Università degli Studi di Ferrara

NOVEL TECHNIQUES FOR IN VIVO CHARACTERIZATION OF SHORT PEPTIDES AND PROTEINS IN MEMBRANE PERMEABILIZATION AND SIGNAL TRANSDUCTION

MARCO AQUILA

PhD thesis in “Biomedical Sciences”

April, 2012

Università degli Studi di Ferrara

DOTTORATO DI RICERCA IN

"SCIENZE BIOMEDICHE"

CICLO XXIV

COORDINATORE Prof. Capitani Silvano

NOVEL TECHNIQUES FOR IN VIVO CHARACTERIZATION OF SHORT PEPTIDES AND PROTEINS IN MEMBRANE PERMEABILIZATION AND SIGNAL TRANSDUCTION

Settore Scientifico Disciplinare BIO/09

Dottorando

Dott. Aquila Marco

Tutore

Prof. Rispoli Giorgio

Anni 2008/2011

ABSTRACT

My scientific interest is focused on the field of cellular electrical activity, ranging from the study of intracellular enzymatic processes to the characterization of new generation of drugs. For this purpose I also used the most powerful techniques of investigation, including patch-clamp technique, fluorescence imaging, and surface plasmon resonance (SPR) spectroscopy. Moreover, to shed light on complex molecular mechanisms, unconventional strategies were employed, requiring sometimes the realization of specific devices not commercially available.

In particular my PhD thesis includes two different scientific projects: the biophysical characterization of antimicrobial peptides and the modulation of visual phototransduction in vertebrate cones.

In the first project, the patch-clamp technique was employed to study the pore forming properties of synthetic cecropin-melittin hybrid peptide (CM15), alamethicin F50/5 and its synthetic analog [L-Glu(OMe)^{7,18,19}] under strict physiological conditions. These short peptides selectively permeabilize the bacteria plasma membrane leading to their lyses and death: they are therefore a source of antibacterial molecules, and inspiration for novel and more selective drugs. I pursued this study by recording the ion current through the channels formed by these peptides, once inserted in the membrane of photoreceptor rod outer segment membrane (OS) isolated from frog retinae. The peptides were applied to (and removed from) the extracellular OS side in ~50 ms with a computer-controlled microperfusion system, so that the ion channel characteristics (as its selectivity, blockade and gating) and the dynamics of pore formation could be precisely assessed. On the basis of the electrophysiological recordings obtained, it was demonstrated that, different than alamethicins, CM15 produced voltage-independent membrane permeabilisation, repetitive peptide application caused a progressive permeabilisation increase, and no single-channel events were detected at low peptide concentrations. Collectively, these results indicate that CM15 form pores according to a toroidal model. Moreover, in order to understand the divalent-cation dependency of [L-Glu(OMe)^{7,18,19}] binding to the lipid bilayer at the molecular level, the electrophysiological experiments were paralleled with experiments employing SPR spectroscopy. Results indicate the presence of Ca^{2+} in the external solution increases the probability of formation of smaller and more stable *[L-Glu(OMe)^{7,18,19}]* pores.

The second project of this thesis concerns the investigation of the physiological role of the neuronal calcium sensor zGCAP3 in the photrasduction cascade. This study was pursued

through the simulation of an over expression and a knock-down of this protein, by delivering it, or its monoclonal antibody, into zebrafish cone cytosol, while recording their photoresponses with the patch-clamp technique. The intracellular protein delivery was attained via the patch pipette, by ejecting the proteins out of a tube inserted into the pipette lumen. A microperfusion system was employed to apply the desired exogenous molecules with a precise timing. However, the long tapered shape of the pipette shank make it very difficult to perfuse efficiently the cell with this strategy. For this reason a pressure polishing setup was assembled to enlarge the patch pipette shank, through the calibrated combination of heat and air pressure. This allowed to insert quartz or plastic tubes in the pipette lumen very close to its tip. In order to obtain a substantial and specific silencing of the zGCAP3s in zebrafish cones, surface plasmon resonance experiments were performed to allow the selection of a monoclonal antibody with strong affinity for zGCAP3 and low cross interaction with other components of the phototransduction cascade. Results showed that the perfusion with GCAP3 did not altered significantly the light response, while he anti-zGCAP3 incorporation in the cytosol caused the progressive photoresponse fall, followed by the progressive fall of saturating flash response amplitude, probably due to the progressive GC inhibition. The unexpected lack of an effect of zGCAP3 incorporation in the cone cytosol, suggests that the endogenous number of zGCAP3 is saturating, i.e. their number is equal or above the number of their target molecules (guanylate cyclase), therefore any further increase of zGAP3 in the cytosol is uneffective.

TABLE OF CONTENTS

ABSTRACT

1. INTRODUCTION

1.1 ANTIMICROBIAL PEPTIDES

1.1.1 Methods to study pore formations dynamics of AMPs

1.1.2 Peptaibol alamethicin F50 and analogues

1.1.3 Cecropin-Melittin Hybrid Peptide CM15

1.2VISUAL PHOTRASDUCTION IN VERTEBRATE

1.2.1 Guanylate cyclase-activating proteins (GCAP)

1.2.2 Guanylate cyclase-activating proteins in the Zebrafish retina

1.2.3 A novel strategy to investigate the physiological role of zGCAP3

2. METHODS

2.1 ANTIMICROBIAL PEPTIDES SEQUENCES AND USAGE

2.2 PROTEINS AND ANTIBODIES

2.2.1 zGCAP3, zGCAP4 and IgG1 monoclonal antibodies

2.2.2 Antibodies purification by anion-exchange-chromatography (AEC)

2.3 CELL PREPARATION

2.3.1 Rod and cone outer segments isolation procedure

2.3.2 Cell viewing

2.4 ELECTROPHYSIOLOGY

2.4.1 Patch-clamp technique

2.4.2 Pressure polish setup

2.4.3 Pressure polishing procedure and pipette usage

2.4.4 Sealing virtually on any membrane with just one glass type

2.4.5 Intrapipette perfusion

2.4.6 Fast external perfusion system

2.4.7 Frog OS recordings, peptides applications and solutions

2.4.8 Zebrafish cones recording, light stimulation, intracellular perfusion and solutions

2.4.9 Fluorescence imaging

2.5 SURFACE PLASMON RESONANCE (SPR) SPECTROSCOPY

2.5.1 SPR theory

2.5.2 SPR analysis of zGCAP3-antibody interactions

2.5.3 Peptide-membrane interactions monitored by surface plasmon resonance

2.5.4 Liposome preparation for surface plasmon resonance experiments

2.5.5 Fitting of data to interaction models

3. RESULTS AND DISCUSSION

3.1 OS endogenous conductances and antimicrobial peptide characterization

3.1.1 Comparison between CM15 and F50/5 permeabilization properties

3.1.2 F50/5 monomer assembling mechanism

3.1.3 Role of divalent cation in [L-Glu(OMe)^{7,18,19}]-membrane interaction and pore formation

3.1.4 Membrane binding of [L-Glu(OMe)^{7,18,19}] monitored by SPR

3.1.5 Ca^{2+}-sensitivity of Trichogin GA IV and [L-Glu(OMe)7,18,19] binding to membrane

3.1.6 Ca^{2+} -dependent modulation of antimicrobial peptide activity

3.2 Modulation of zebrafish cone phototransduction by intracellular delivery of zGCAP3 and of its antibody via patch-clamp pipette

3.2.2 Zebrafish cones dialysis with ZGCAP3

3.2.3 Determination of IgG1 monoclonal antibodies- zGCAP3 affinity by SPR

3.2.4 Binding properties of purified IgG1 7E6

3.2.5 Comparison between global and local fitting to the sensorgrams

3.2.6 zGCAP3 dimerization test

3.2.7 Ca^{2+}-independence of the antibody interaction with zGCAP3

3.2.8 Mass transfer limitation in SPR experiments

3.2.9 Evaluation of zGCAP3 and its antibody on GC activity

1. INTRODUCTION

1.1 ANTIMICROBIAL PEPTIDES

In the last decades, there is a dramatic increase in the number of common and emerging cases of infection due to antibiotic-resistant bacteria, occurring for instance in hospitals and in high frequented spaces. Antibiotic resistance develops when a microorganism mutates or acquires a resistance gene so that standard treatments become ineffective and infection persists. Therefore, discovery and development of new antibiotics is crucial. Part of the work described in this thesis is focused on the study of antimicrobial peptides (AMPs), which represent a potential class of novel antimicrobial agents. These peptides are an evolutionarily conserved component of the innate immune response, which is the main defence system for the majority of living organisms, and are found among all classes of life ranging from prokaryotes to humans (Ganz, 2003). The broad-spectrum activity, the high efficacy and the low level of induced resistance of AMPs (Gordon et al., 2005) have stimulated the research toward the clinical application of these peptides. Besides the development of anti-bacterial drugs, the pore-forming peptides, being the most ancestral form of membrane pores, provide also a simple model system to understand the structure-function relationships of channels and the molecular basis of peptide/protein oligomerization in lipid membranes. Moreover, these peptides are a powerful molecular model on which to build custom molecules with wide-ranging biotechnological applications, as ion channel modulators (Hille, 1992), anti-tumorigenic agents (Papo & Shai, 2005, Hoskin & Ramamoorthy, 2008) biosensors for many different analytes (Aili & Stevens, 2010), and provide a pharmacological approach to cure channelopaties (Wilde, 2008). In the latter case, a synthetic channel could be inserted in cells expressing an aberrant ion channel (Wallace et al., 2000) to restore the physiological ion flow. AMPs may finally provide insights about the evolution of channel selectivity and gating and, more generally, of ion pumps and exchangers: recent data from many laboratories indicate indeed that secondary transporters are basically pores with an highly specialized gate system (Gadsby, 2009). Antimicrobial peptides are classified on the basis of their amino acid composition (generally between 12 and 50 amino acids), spectrum of activity and mode of action. According to a structural scheme of classification (Fig. 1.1), the two largest groups are the α-helical and β-sheet peptides, but other examples of conformations have also been identified: the β-hairpin conformation, for example, is due to the presence of one or more disulfide bonds. Moreover,

many peptides are unstructured in free solution and fold into their final configuration during the interaction with phospholipids of cell membranes.

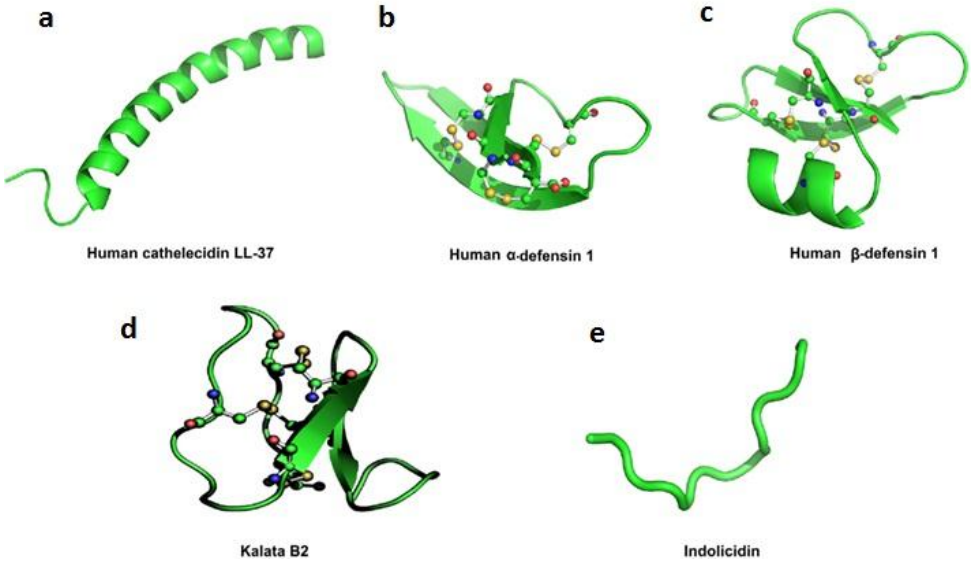

Fig. 1.1. An overview of the major structural classes of host-defense peptides including ***a*** α-helices, ***b*** β-sheets, ***c*** a mixture of α-helices/β-sheets structures, ***d*** cyclic, and ***e*** extended structures. Disulfide bonds are represented in ball and stick.

The AMP mode of action can be broadly divided into intracellular and extracellular mechanisms (Brogden, 2005). The former include the inhibition of DNA or RNA synthesis or blocking of other enzymatic processes involved in bacteria metabolism (Fig. 1.2); the latter consist mainly in a peptide-membrane interaction resulting in the membrane permeabilization and the consequent lysis and death of the pathogen.

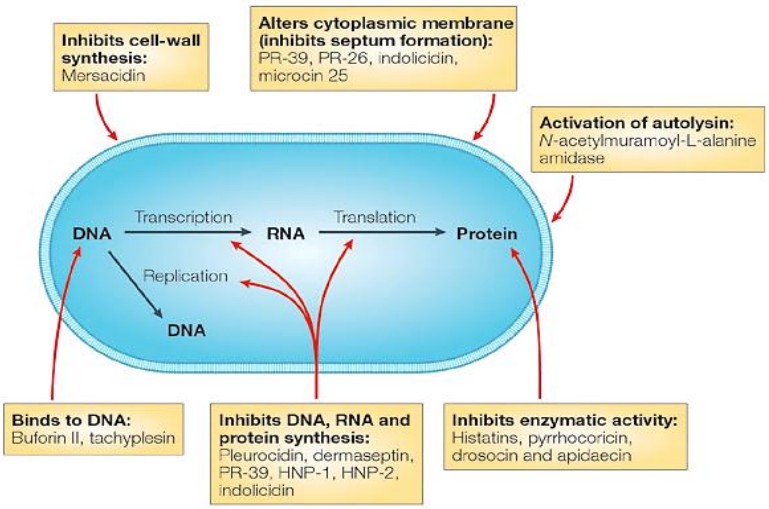

Fig. 1.2. Mode of action AMPs (Brogden, 2005)

This peptide activity and specificity is modulated by several structural and physicochemical parameters of AMPs such as: aminoacid sequence, charge, amphipathicity and secondary structure. Moreover differences in biomembrane composition create an important first discrimination between prokaryotic and eukaryotic cells during the immunity response mediated by AMPs. Indeed, cell membranes of many pathogens are characterized by an high electronegativity due to a predominant concentration of phosphatidylglycerol (PG), cardiolipin (CL) and phosphatidylserine (PS) and this increases the peptide antimicrobial effect. Mammalian cell membranes are instead generally neutral, due to the presence of zwitterionic phospholipids such as: phosphatidylethanolamine (PE), phosphatidylcholine (PC) and phosphatidylserine (PS). Based on these considerations it is clear that peptides with a net positive charge showed a stronger activity against pathogens, with an optimal range between +2 and +9, as demonstrated in the case of the AMP mellitin and magainin analogs (Dathe et al., 2001).

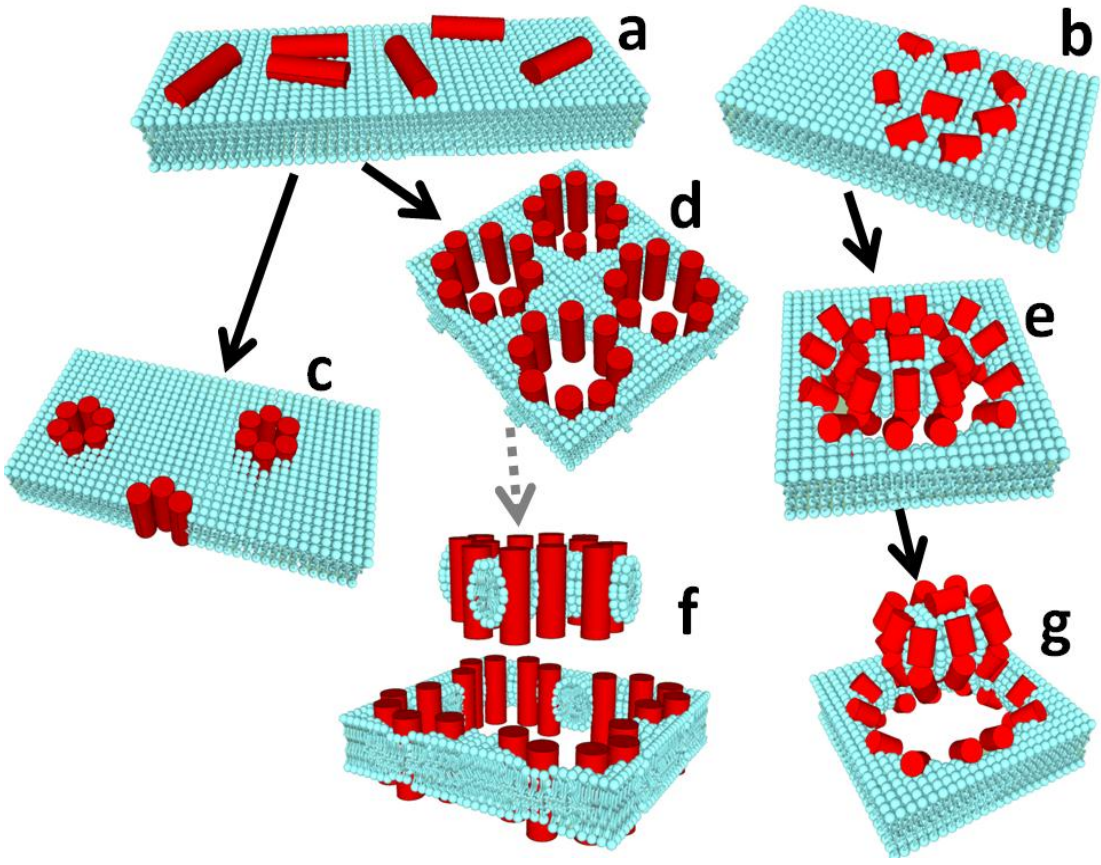

Fig. 1.3. Mechanisms of cell membrane permeabilisation induced by a peptide. After adhering on the external face of the membrane (***a*** and ***b***), the peptide could insert in the membrane according to a barrel stave (***c***), toroidal (***d*** and ***e***), or carpet mechanism (***f*** and ***g***).

Therefore, the right equilibrium between hydrophobic and hydrophilic aminoacids determinates the extent to which AMPs can partition into the lipid bilayer forming transmembrane pores. However, a strong hydrophobicity is related to an high toxicity and loss of antimicrobial specificity (Yeaman & Yount, 2003).

Regardless their origin and purpose, all the membrane permeabilizing peptides adhere first parallel to the lipid bilayer (Fig. 1.3*a* and *b*), they then orient perpendicular to the membrane, and finally they bind together and/or reorganize the lipid bilayer to form transmembrane pores. Because of their amino-acid composition, amphipathicity, and cationic charge, three distinct mechanisms have been proposed to explain membrane permeabilization (Brogden, 2005): "barrel and stave", "toroidal", and "carpet" (Fig. 1.3). The first mechanism requires that the peptide monomers, weekly bound to the membrane surface (Fig. 1.3*a*), orient perpendicularly to the latter and bind together (as staves) around a central pore (the barrel; Fig. 1.3*c*). The peptide hydrophobic segments face the bilayer core, while their hydrophilic segments face the pore lumen. In the toroidal pore, the polar segments of the peptides interact with the polar head groups of the lipids more strongly than in the case of the barrel and stave pore, so that the lipids are forced to tilt from the lamellar normal up to connect the two leaflets of the membrane, forming a continuous bend from one side to the other of the membrane, in the fashion of a toroidal hole (peptides spanning the entire membrane: Fig. 1.3*d*; peptide shorter than the membrane thickness: Fig. 1.3*e*). Differently from the barrel and stave mechanism, the peptides are always associated with the lipid head groups, even when they are perpendicularly inserted in the lipid bilayer. In the carpet mechanism, the strong electrostatic interactions between peptides and the phospholipid head groups result in the peptide carpeting of the membrane (Fig. 1.3*b*). The peptides then assemble with the lipids to form transiently toroidal pores (Fig. 1.3*e*), allowing more and more peptides to cross the bilayer and eventually cover the other membrane leaflet. Finally, the peptides may isolate a micelle that detach from the membrane to head to the water phase (Fig. 1.3*g*), leading to the bilayer disintegration in a detergent-like manner. It is also possible that the contour of a micelle may be delimited by several toroidal pores that happen to group together (Fig. 1.3*d*), and this micelle may eventually separate from the membrane and solubilize (Fig. 1.3*f*). Moreover, it is conceivable that the same peptide may permeabilize the membrane with one mechanism or with another (Brogden, 2005), depending upon the surrounding conditions, as the lipid environment, the temperature, the peptide concentration, the presence of some other endogenous or exogenous molecules (Noshiro et al., 2010)., etc.

1.1.1 Methods to study pore formations dynamics of AMPs

Several approaches are used to assess the mechanisms of AMPs activity. The first one is to observe the microbial cell integrity following the application of AMPs, by using advanced microscopy techniques, as confocal laser-scanning microscopy or scanning and transmission electron microscopy (Kalfa et al., 2001, Yenugu et al., 2004). The peptide-membrane interactions are studied by employing a large variety of biophysical techniques: differential scanning calorimetry (DSC), circular dichroism (CD) spectroscopy, NMR, surface plasmon resonance (SPR), and scattering techniques (X-ray and neutron scattering). Pore formation is one of the most intensively studied AMPs mechanism of action. Most of the research on these AMPs, has the long-term goal to understand at the molecular level how the peptide-lipid interactions produce structural changes in both, and optimal peptide orientation, to eventually produce a raise in membrane conductance (Chen et al., 2001, Saint et al., 2002). This membrane permeabilization can be followed by measuring, for instance, the release of fluorescent-labelled molecules trapped into phospholipid vescicles, or measuring the ionic current flowing through the AMPs-induced pores. With this aim, a widely used technique consists in recording the ion current flowing through the pore formed by these peptides inserted in an artificial lipid bilayer. To have an acceptable signal-to-noise ratio in these experiments, it is necessary to apply non-physiological voltages and ionic gradients, that however could affect the peptides themselves, or even the membrane in which they were inserted (Bockmann et al., 2003). Moreover no studies addressed directly the kinetics with which peptides assemble and disassemble to form a functioning pore in the plasma membrane of a living cell. In this thesis, the biophysical characteristics and the pore formation dynamics of selected antimicrobial peptides and some of their analogues, were studied under strict physiological conditions. This was accomplished by inserting these (or other) peptide monomers in the plasma membrane of a living cell, and recording the current flowing through the peptide channels at a desired voltage by using the whole-cell, patch-clamp technique (see Methods). To make sure that the entire current was flowing through these channels, it was looked for a particular cell system where all the endogenous conductances could be blocked without using any drug, that could affect the peptide pore as well. The outer segment of the photoreceptor rod (OS) mechanically isolated from low vertebrate retinae (Rispoli et al., 1993) is such a cell system, because the only channel type of this cell fragment is fully closed by bright light. The OS of *Rana esculenta* have been found particularly suitable to carry on this study, because of their large size and for the

commercial availability and low cost of this edible frog species. To have a precise control of pore formation (and disaggregation), a custom-made, computer controlled microperfusion system was employed to rapidly apply (and remove) the peptides under study onto a cell. Peptide formation and disaggregation dynamics were therefore gathered, respectively, from the time course of the development and fall of the exogenous current (at a given potential, V_h), following peptide application and removal (Vedovato et al., 2007). This system is also capable to apply and remove ions, drugs and peptides on any isolated cell or tissue fragment in ~50 ms with an accurately controlled timing. This thesis focuses on the biophysical characteristics and the pore formation dynamics of the major component of the neutral fraction (F50/5) of the alamethicin, the L-Glu(OMe)$_{7,18,19}$ alamethicin analog and the Cecropin-Melittin Hybrid Peptide CM15.

1.1.2 Peptaibol alamethicin F50 and analogues

Peptaibiotics are an important group of antibiotic peptides, which are biosynthesized by fungi, mainly of the *Trichoderma* genus. They are linear and amphipathic polypeptides, composed of 5 to 20 amino acids (e.g., peptaibolin, atroviridin, alamethicin, suzukacillin, paracelsin, polysporin), and contain non-proteinogenic amino acid residues such as α-aminoisobutyric acid (Aib).The N-terminal residues of peptaibiotics are usually acetylated, and an amino alcohol (phenylalaninol, valinol, leucinol, isoleucinol, or tryptophanol) is linked by a peptide bond at the C-terminal end. Alamethicins, the longest peptaibiotics, are a group of closely sequence-related peptides composed of 19 amino acid residues and exhibit biological activities including antibacterial and antifungal effects. They form voltage-dependent pores into biological membranes, and are the most extensively investigated among simple model compounds of large pore-forming proteins. The hydrophobic nature of alamethicin allows it to be inserted into biological membrane forming unspecific ion channels (with up to approximately 10 Å pore size) supposedly based on the transmembrane assembly of 6 or 8 helical alamethicin molecules according to the "barrel stave" model (Baumann & Mueller, 1974, Boheim, 1974). This thesis is focused mainly on the biophysical characteristics and the pore formation dynamics on natural membranes of the synthesized F50/5 peptaibol, which is the major component of the neutral fraction of the alamethicin, and its synthetic analog [L-Glu(OMe)^{7,18,19}]. The latter was obtained from F50/5 aminoacid sequence by substitution of glutamine (Gln) residues at positions 7, 18, and 19 with side-chain esterified glutamic acid (Glu) residues, because Gln was believed to be of key relevance for the pore formation (Fox &

Richards, 1982, Molle et al., 1996). The three dimensional structure of [L-Glu(OMe)^{7,18,19}] at a resolution of 0.95 Å, resolved from the electron density maps obtained by using the synchrotron radiation, consisted of two crystallographically independent bent α-helices (showed in Fig. 1.4), just long enough to span the membrane, but that cannot conduct ions through the hole produced by their helical arrangement (Crisma et al., 2007).

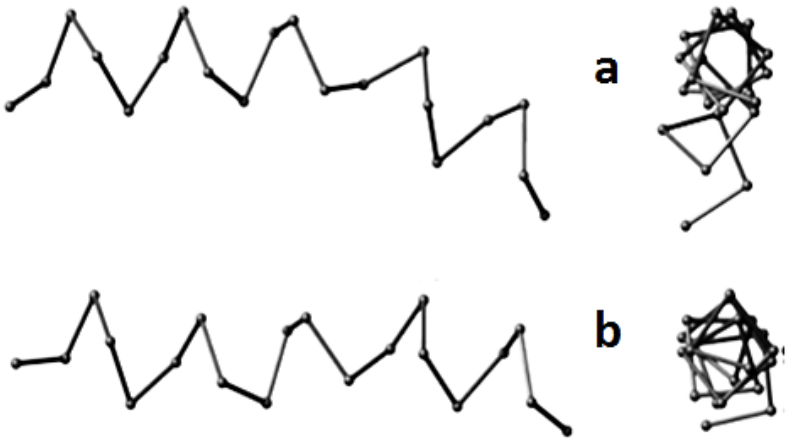

Fig. 1.4. The α-carbon traces of the two crystallographically independent bent [L-Glu(OMe)^{7,18,19}] α-helices ***a*** and ***b*** (Crisma et al., 2007).

In order to shed light on the different aspects and phases of the peptide-membrane binding, in this thesis the electrophysiological experiments with [L-Glu(OMe)^{7,18,19}], were paralleled by SPR investigation. The latter is an optical method to monitor biomolecular interactions (see Methods), and specific SPR-based biosensors have been developed to measure differences in peptides association with different biomimetic membranes (Hall & Aguilar, 2010).

1.1.3 Cecropin-Melittin Hybrid Peptide CM15

The aminoacid sequences of AMPs is strictly correlated to their antibiotic activity: indeed, the creation of antimicrobial peptide chimeras, by the hybridization of specific aminoacid sequences from different AMPS, is one successful approach to improve the antimicrobial effect, reducing toxicity toward eukaryotic cells. In this thesis it was addressed the study of the pore formation properties of CM15, which is an α-helix hybrid, composed of the first seven residues of cecropin A and residues 2–9 of the bee venom peptide mellitin. Cecropin A is a naturally occurring, 37-residue, helical antimicrobial peptide found in the silk moth *Hyalophora cecropia*, and mellitin is a 26-residue peptide found in the venom of the

honey bee *Apis mellifera*. While mellitin has potent, broad-spectrum antimicrobial activity, it is extremely hemolytic, causing damage to host red blood cells. In contrast, cecropin A shows low cytotoxicity but has lower antimicrobial activity. The CM15 hybrid was first synthesized by Andreu (Andreu et al., 1992) who combined the favorable characteristics of each AMP: the resulting peptide displays potent broad-spectrum antimicrobial activity and low cytotoxicity. However, it is not clear whether CM15 forms discrete membrane pores or disrupts membranes via a detergent-like carpet mechanism. In this thesis, it has been studied the biophysical characterization of the pore formation dynamics of CM15 under physiological conditions. This allowed to study, besides the ion channel characteristics (such as the presence of gating, its voltage dependence, the unitary conductance, and the selectivity and blockade), the dynamics of pore formation as well, that are of key importance to assess the channel performance and its potential biotherapeutic activity

1.2 VISUAL PHOTRASDUCTION IN VERTEBRATE

Phototransduction is the process that occurs in vertebrate photoreceptor cells by which the energy of a photon is captured by a visual pigment molecule and is converted into a detectable electrical signal, trough the activation of a cascade of biomolecular events exhibiting an high degree of amplification. There are two classes of photosensitive cells: rods and cones (Fig. 1.5). Cones function in bright light (daylight) and are responsible for colour vision. Rods are sensors of dim light and do not discern colours, but they are able to detect even single photons, due to an extremely high amplification not paralleled by other signal transduction pathways.

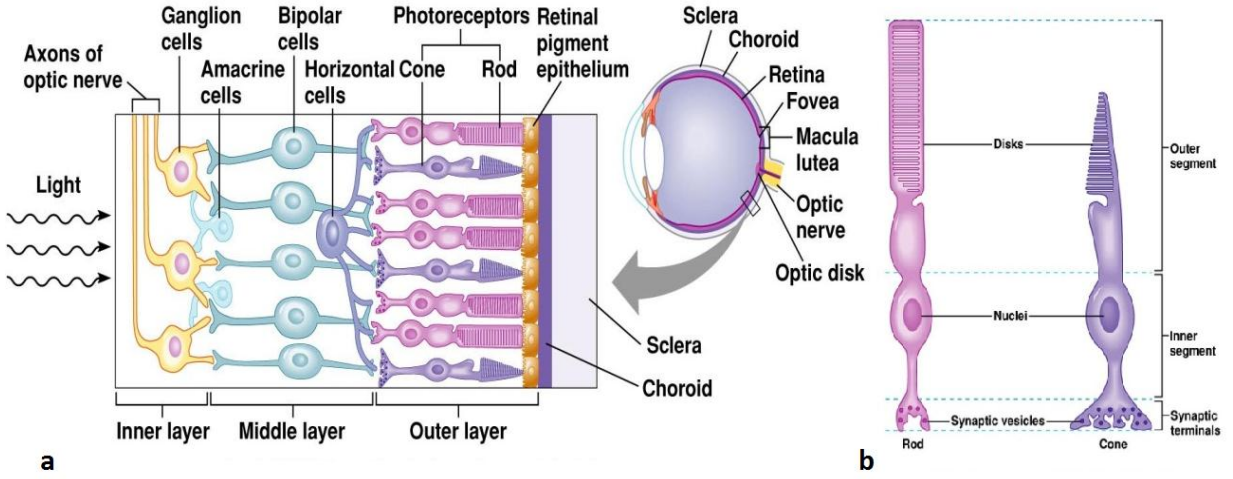

Figure 1.5. Structure of the retina and photoreceptor cell types. ***a*** Simple diagram of the neuronal organization of the retina, where the photoreceptors are connected to the ganglion cells through several interneurons of three types. ***b*** The two types of photoreceptors: rods (*left*) and cones (*right*). The outer segment of each cell contains the lamellar membranes in which are embedded most of the proteins of the phototransduction cascade, and where phototransduction occurs. Photoreceptor inner segments contain the nucleus, organelles (mitochondria, ribosomes, endoplasmic reticulum, synaptic vesicles, etc), and the synaptic terminal (where neurotransmitter is released).

In the dark-adapted state the presence of cGMP in a photoreceptor cell keeps the cGMP-gated channels open, allowing a steady inward current, carried by Na^+ and Ca^{2+} called the dark current (Fig. 1.6). The inward current driven by Na^+ and Ca^{2+} is balanced by an outward K^+ current through K^+ and Ca^{2+} selective channels. The resulting circulating current keeps the cell depolarized at about -40 mV. The depolarization of the cell membrane opens voltage-gated Ca^{2+} channels: the consequent increase of intracellular Ca^{2+} concentration causes the release of glutamate at the synaptic terminal toward the bipolar and the horizontal cells. Light activates an enzymatic cascade which ends with the hydrolysis of cGMP causing the closure of the cGMP gated channels reducing the influx of Na^+ and Ca^{2+}. The consequent reduction of cationic influx

causes photoreceptor hyperpolarization, the closure of the voltage-gated Ca^{2+} channels and the reduction of the rate of neurotransmitter release at the synapse (Fig. 1.6, *right*).

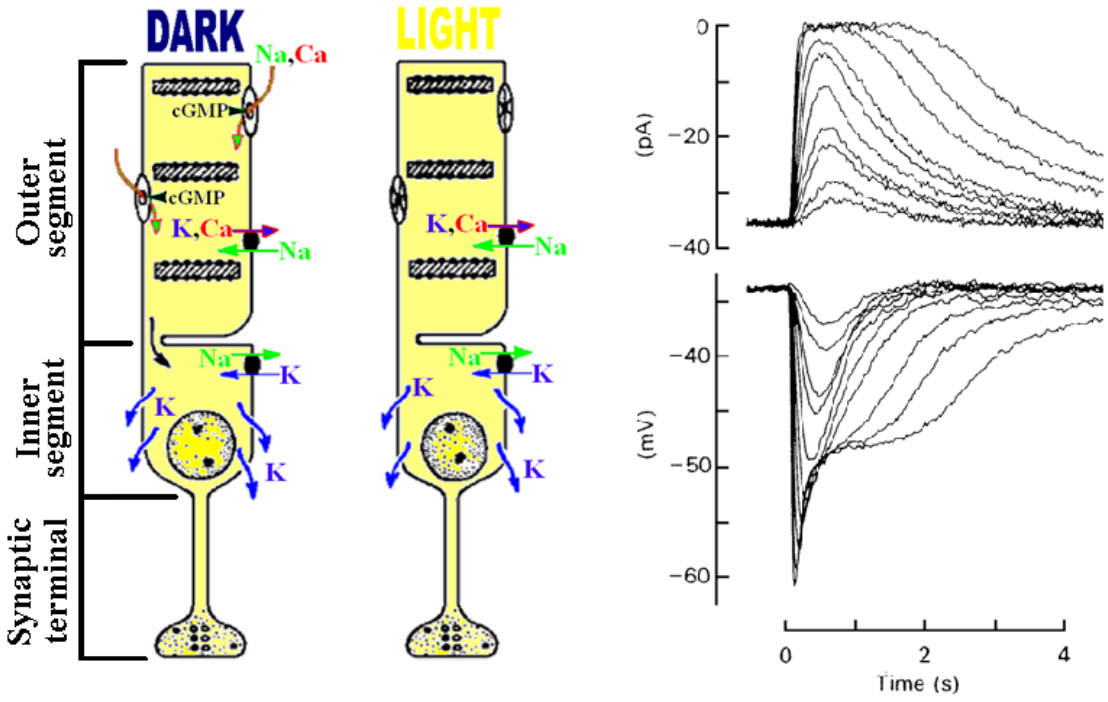

Figure 1.6. *Left* Ion fluxes across the membrane of a photoreceptor cell (in this case, a rod). *Right* Electrical response of an isolated rod photoreceptor. *Upper right panel* the transient suppression of the current entering the outer segment in response to 20 ms flashes of light of progressively increasing intensity, is recorded with a suction pipette; *lower right panel* simultaneous voltage recording with an intracellular microelectrode impaling the inner segment.

The complex molecular mechanisms underlying the visual cascade allow the effective transduction of light into a photocurrent change, which can be detected by electrophysiological recordings performed either on single isolated cells or, in vivo, on the animal itself. Such mechanisms have been deeply studied in the last four decades, and many of the elements and physiological properties of the signalling cascade are now well established (Rispoli, 1998, Lamb & Pugh, 2006, Dell'Orco et al., 2009). The elements of the phototransduction enzymatic cascade are packed into a stack of flattened, membranous vesicles, called disks, that in rods are enclosed by the membrane of the outer segment, while in cones the disk membranes are invaginations of the plasma membrane (Fig. 1.5*b*).

The phototransduction cascade is initiated by the absorption of light by 11-cis-retinal, a chromophore bound to rhodopsin (R), a member of seven-transmembrane helix receptor coupled to G-protein (GPCRs). After the photon absorption, 11-cis retinal undergoes photoisomerization to all-trans retinal, a form that causes a conformational change of the visual pigment (R) in its activated form, known as metarhodopsin II (MII or R*).

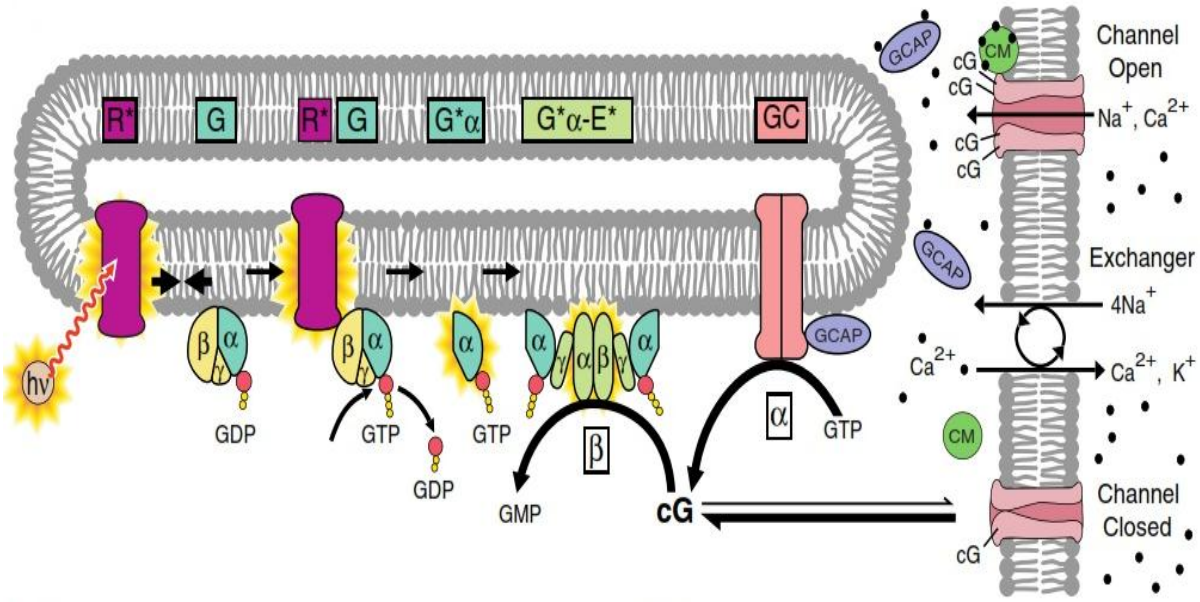

Fig. 1.7. Phototransduction cascade activation by light.

Within a millisecond of photon capture, R* activates heterotrimeric GDP-bound transducin (G) by catalyzing the GDP/GTP exchange on its α subunit (G*α), which is followed by the dissociation of the GαGTP complex from the βγ dimer. GαGTP activates phosphodiesterase (PDE), which is an holo-enzyme composed by two catalytic (α and β) and two regulatory (γ) subunits. The GαGTP removes the γ subunit from the catalytic sites of PDE, which in this active form (E*) hydrolyzes guanosine 3-cyclic monophosphate (cGMP). The consequent reduction of the cGMP concentration leads to the closure of cyclic nucleotide gated channels, which in turn determines a decrease in the circulating ion current due to the reduction of the inward Na^+ and Ca^{2+} current. Consequently, the intracellular Ca^{2+} concentration drops, due to continuous Ca^{2+} extrusion from the cell via the Ca^{2+}/K^+–Na^+ exchanger.

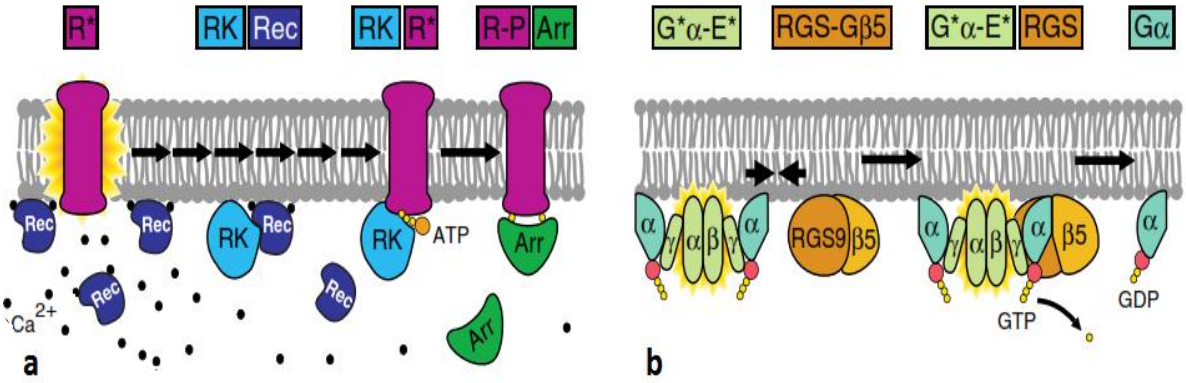

Figure 1.8. ***a*** Inactivation of R*. ***b*** Inactivation of G*–E*.

The decline of Ca^{2+} concentration with light, causes the release of Ca^{2+} from at least three Ca^{2+} sensor proteins which act through a negative feedback mechanisms on the cGMP channels: calmodulin, GC-activating proteins (GCAPs), and recoverin (Rec). These mechanisms mediate response shut-off and adaptation of the signalling cascade (Fain et al., 2001, Nakatani et al., 2002). In detail, release of Ca^{2+} from calmodulin causes its dissociation from the cGMP gated channels, thus increasing their affinity for cGMP; GCAPs activate instead guanylate cyclase (GC) following Ca^{2+} release, thus promoting the cGMP recovery at the shut-off of the light stimulation. (Fig. 1.7). Indeed, the Ca^{2+}/GCAP-dependent regulation of GC activity forms a powerful negative feedback mechanism, in which the rate of cGMP synthesis increases as Ca^{2+} falls during the photoresponse, thereby setting the photoresponse amplitude, accelerating the recovery phase of the photoresponse, and improving the signal-to-noise characteristics of the rod. Finally, release of Ca^{2+} from Rec makes the latter to dissociate from Rhodopsin kinase (RK), which becomes free to phosphorylate the C-terminus of R*. This allows the association of R* with Arrestin (Arr), resulting in R* inactivation (Fig. 1.8*a*). Signalling shut-off also includes the simultaneous deactivation of GαGTP and PDE, which occurs because G*α possesses an intrinsic catalytic activity, which hydrolyses bound GTP in GDP. This hydrolysis is significantly accelerated by a multiprotein complex, called RGS-Gβ5, which is formed by the ninth member of the regulators of G-protein signalling (RGS) family, bound to its obligatory Gβ5 subunit (Fig. 1.8*b*). As a result of the GAP (GTPase activating protein) action of RGS-Gβ5, the GTP is hydrolyzed in GDP: the GDP bound to the Gα promotes the re-association of GαGDP to the βγ dimer, restoring the GαGDP-βγ heterotrimer (i.e. G). All these negative feedbacks collectively accelerate the recovery of the dark state once the light stimulation has turned off. They also generate the well-known phenomenon of photoreceptor light adaptation in the presence of continuous illumination: indeed, the reduction of intracellular Ca^{2+} accelerates the re-synthesis of cGMP and increases the sensitivity to cGMP of the cGMP-gated channel. This promotes a partial recovery of the light-suppressible current despite the continuous illumination (see Fig. 3.23*a*).Moreover, the higher cGMP flux and the higher rate of R phosphorylation, produces responses to light stimuli superimposed on a background of light faster and smaller in respect to the response to the same light stimuli in the dark (see Fig. 3.23*b*,*c*).

1.2.1 Guanylate cyclase-activating proteins (GCAP)

The neuronal calcium sensor (NCS) protein family consists of a group of Ca^{2+}-binding proteins whose expression is restricted to neuronal systems including retinal photoreceptor cells (Palczewski et al., 2000, Polans et al., 1996). These proteins bind Ca^{2+} through EF-hand motifs and many of them are fatty acylated at the amino terminus, most frequently with myristic acid (Ames & Ikura, 2002). NCS proteins serve as switches for Ca^{2+} signalling by assuming different Ca^{2+}-dependent conformational changes. Two members of this family, Rec and GCAP, are expressed only in the retina, where they play an important role in light adaptation and in recovery of the dark current level once the light stimulation is ceased. The intracellular stimulation of GC mediated by GCAP at low Ca^{2+} concentration, was showed for the first time by Koch and Stryer (Koch & Stryer, 1988). The general structure of GCAP reveals a compact protein made of two domains separated by a flexible linker and each domain contains a pair of EF-hands (Fig. 1.9). A post-translational myristoylation at the N-terminal Gly residue is predicted to be common to all GCAPs (Palczewski et al., 2004). GCAPs regulate their target enzyme, GCs, as a function of Ca^{2+} which binds to their EF-hands. The conformational change induced by Ca^{2+} dissociation activates GCAPs, which in turn increase the activity of GCs, and dimerization of GCAP monomers has been proposed as a mechanism of GC regulation (Olshevskaya et al., 1999).

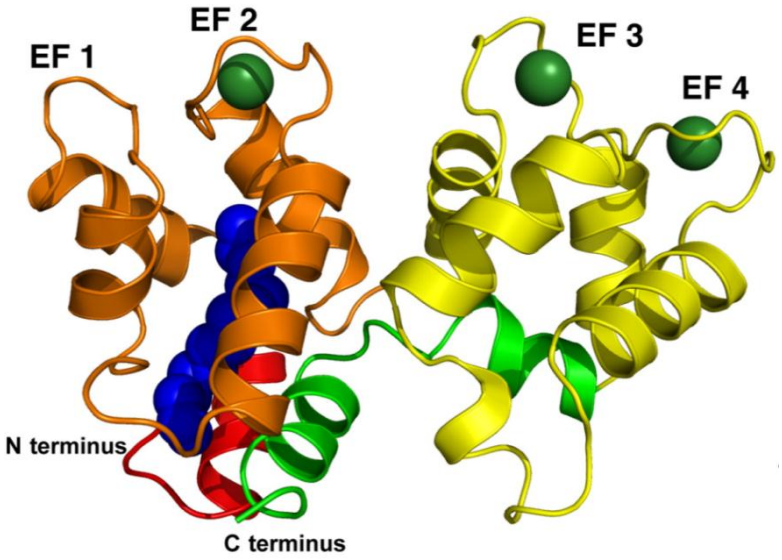

Figure 1.9. Representation of Structure of GCAP1 with three Ca^{2+} bound. The N-terminal helix is red, N-terminal domain (EF-1 and EF-2) is orange, C-terminal domain (EF-3 and EF-4) is yellow, kinked C-terminal helix is green, and the Ca^{2+} ions and myristoyl group are shown as dark green and dark blue space-filling spheres, respectively.

Two GCAPs (GCAP1 and GCAP2) first isolated from bovine retina (Dizhoor et al., 1995, Gorczyca et al., 1995, Palczewski et al., 1994) are present in all mammals. A third isoform, GCAP3, is expressed in human and zebrafish (*Danio rerio*) retinas (Haeseleer et al., 1999, Imanishi et al., 2004) and it has not been found in mouse retina. At least five additional GCAPs (GCAP4–8) are predicted to be present in pufferfish (*Fugu rubripes*) and zebrafish genomes (Imanishi et al., 2004). The physiological contribution of GCAPs in the photocurrent modulation has been investigated by Mendez (Mendez & Chen, 2002), through the comparison of the flash response of wild-type rods and rods where GCAP1 and GCAP2 were silenced by knocking out the relative genes in a transgenic mouse ($GCAPs^{-/-}$). These authors found that flash responses recorded from dark-adapted $GCAPs^{-/-}$ rods were larger (i.e. were more sensitive) and slower than the responses to the same flashes recorded from wild-type rods. This indicates that GCAP1 and GCAP2 play a major role in response recovery (Fig. 1.10).

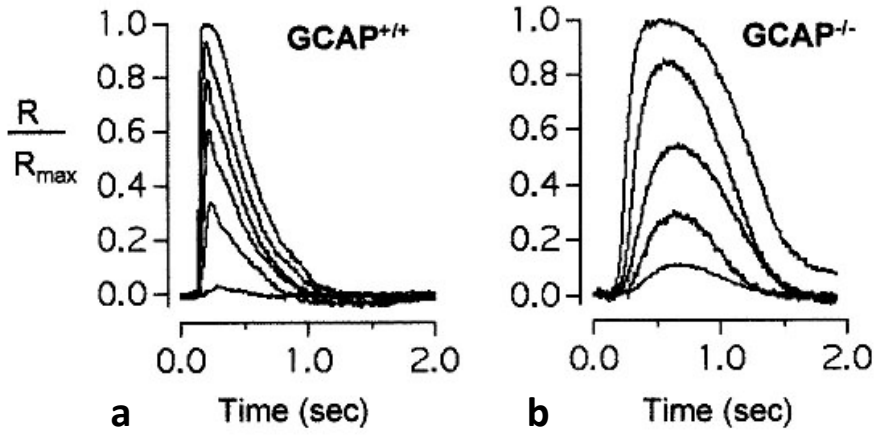

Figure 1.10. Effect of GCAP knock out on the flash response. Representative families of responses from wild-type ***a***, GCAPs−/− ***b*** rods to 10 ms flashes that increase in intensity in ~2-fold steps from starting values (equivalent 500 nm photons/μm2/flash) of: 0.6, 2.0, 8.4, 2.0, 8.4 and 8.4, respectively. Responses were normalized to the rod's resting dark current (R/Rmax). (Mendez & Chen, 2002)

1.2.2 Guanylate cyclase-activating proteins in the Zebrafish retina

Zebrafish (*Danio rerio*) is a common and useful animal model for studies of vertebrate development, gene function and biomolecular processes. The similarities of the zebrafish visual system to that of other vertebrates make this animal a valuable model for visual neuroscience (Bilotta & Saszik, 2001). An interesting feature of the zebrafish retina is the presence of six GCAP isoforms (zGCAPs) which show distinct and partial overlapping expression profiles in rods and cones (Fig. 1.11). This determines a more complex Ca^{2+}-sensor system, if compared

with mammalians, supporting a Ca^{2+}-relay model of differential zGCAP operation in Zebrafish rods and cones (Scholten & Koch, 2011).

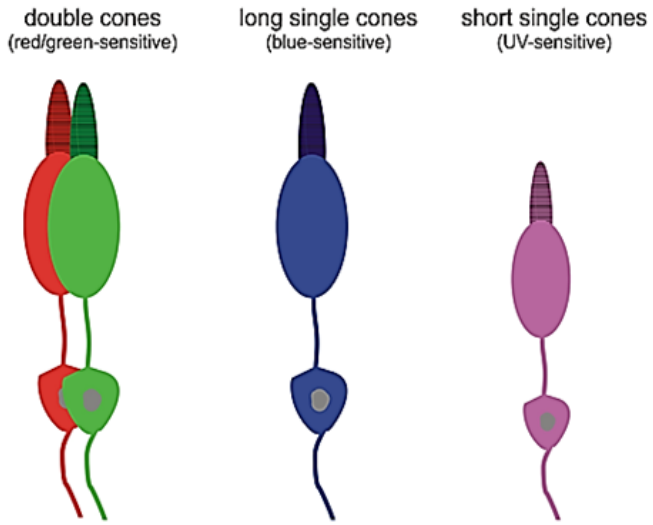

LEVEL OF EXPRESSION	zGCAP ISOFORMS		
HIGH	zGCAP3 zGCAP4 zGCAP5	zGCAP3 zGCAP4 zGCAP5	zGCAP1 zGCAP2 zGCAP3 zGCAP5
LOW	---	---	zGCAP4
FAINT	zGCAP7	zGCAP7	zGCAP7

Figure 1.11. Schematic summary of zGCAP expression in different type of cones. Double cones (long-wavelength sensitive), long single cones (short-wavelength sensitive) and short single cones (UV-sensitive) are drawn schematically in the upper part. The lower part compares the expression profiles of zGCAPs among these cones (Modified form: Scholten and Koch, 2011)

1.2.3 A novel strategy to investigate the physiological role of zGCAP3

The expression pattern zGCAP3 and the role of myristoylation in the Ca^{2+}-sensitivity and in the GC regulation, have been well characterized by biochemical approaches (Fries et al., 2011). These authors found out that the protein expression of zGCAP3 was present in the inner plexiform and ganglion cell layer as well as in that of the photoreceptors, suggesting other zGCAP3 regulatory targets. Moreover it has been demonstrated that the myristoyl group is not necessary for the zGCAP3 functionality: however, myristoylated zGCAP3 shows a higher Ca^{2+}-sensitivity and conformational stability compared to the not myristoylated one.

In this thesis it is also investigated the physiological role of zGCAP3 through the simulation of an over expression and a knock-down of this protein, by delivering it, and its monoclonal antibody, into zebrafish cones, while recording their photoresponses with the patch-clamp technique. The intracellular protein delivery was attained via the patch pipette, by ejecting the proteins out of a tube inserted in the pipette lumen. A microperfusion system (see Methods) was employed to apply the desired exogenous molecules with a precise timing. However, the long tapered shape of the pipette shank make it very difficult to perfuse efficiently the cell with this strategy. For this reason a pressure polishing setup has been assembled to enlarge the patch pipette shank, through the calibrated combination of heat and air pressure, that allowed to insert quartz or plastic tubes in the pipette lumen very close to its tip. In order to obtain a substantial and specific silencing of the zGCAP3s in zebrafish cones, surface plasmon resonance experiments were performed to allow the selection of a monoclonal antibody with strong affinity for zGCAP3 and low cross interaction with other components of the phototransduction cascade.

2. METHODS

2.1 ANTIMICROBIAL PEPTIDES SEQUENCES AND USAGE

The primary structure of all peptides studied in this thesis is reported in Table 2.1. CM15 and its scrambled version were dissolved in bi-distilled water, F50/5 and its analogs in methanol, to get a 50, 100, 500, and 1000 μM stock solutions; an aliquot of one of these peptide stocks was dissolved in the perfusion solution to get a final peptide concentration of 0.25, 0.33, 0.1, 1, 2.5, 5 and 10 μM, and used within 30 min. Control experiments proved that the methanol and DMSO contamination of the perfusion solution (no larger than 10 nl/ ml and 1 μl/ml, respectively) did not cause any non-specific membrane permeabilization.

Peptide	Sequence
F50/5	Ac-UPUAUAQUVUGLUPVUUQQ-Phol
[L-Glu(OMe) ^{7,18,19}]	Ac-UPUAUAEUVUGLUPVUUEE-Phol
CM15	Ac-KWKLFKKIGAVLKVL-NH_2
Scrambled CM15	Ac-KWKLKFKIGLVKLVAV-NH_2
Trichogin GA IV	Oc-UGLUGGLUGI-Lol

Table 2.1. Residue sequences of the peptides studied here. Ac, acetyl; Phol, phenylalaninol; Oc, *n*-octanoyl; Lol, leucinol.

CM15 and its scrambled version were a generous gift of Dr. Feix of Department of Biophysics, Medical College of Wisconsin, Milwaukee, WI, USA; Trichogin GA IV, F50/5 and its analogs were synthesized in the lab of Dr. Toniolo of Department of Chemistry of the University of Padoa, Italy (Peggion et al., 2004).

2.2 PROTEINS AND ANTIBODIES

2.2.1 zGCAP3, zGCAP4 and IgG1 monoclonal antibodies

Recombinant zGCAP3 (and its dansylated version), zGCAP4 and all the IgG1 monoclonal antibodies were a kind gift of prof. Karl-Wilhelm Koch (Biochemistry Faculty V, IBU, Carl von Ossietzky University Oldenburg, D-26111, Oldenburg, Germany). ZGCAPs

were purified from BL21 *E.coli* cells overexpressing the protein, following known protocols (Behnen et al., 2009, Fries et al., 2011, Scholten & Koch, 2011). IgG1 monoclonal antibodies (zG3 7E6-1-1; zG3 6G9-14; zG3 4C12-1-1; zG3 6B9-11) directed against purified recombinant zGCAP3, were produced in the laboratory of Dr. Elisabeth Kremmer (Institute of Molecular Immunology, Helmholtz Zentrum München, Munich,Germany) using rabbits for immunization. IgG1 antibodies were raised against a synthetic peptide corresponding to the last 20 aminoacids (168-188) of the C-terminus of zGCAP3.

2.2.2 Antibodies purification by anion-exchange-chromatography (AEC)

In order to avoid to detect unspecific events during surface plasmon resonance experiments, IgG1 monoclonal antibodies (clones: 7E6,6G9,6B9 and C12) were purified from rabbit serum using the non-denaturing protocol of ion-exchange chromatography. For this purification phase, an anion-exchange-chromatography (AEC) was performed using an ÄKTAprimeTM-FPLC apparatus (GE Healthcare) and a MonoQ 5/50 GL column (GE Healthcare). The column, containing a polystyrene/divinyl benzene matrix, was cleaned before each use as described in the manual and equilibrated with degassed buffers. A solution containing 10 ml of serum antibodies was mixed with 90 ml AEC-buffer A (20 mM $NaPO_4$, pH = 6,5) and loaded onto the column via an injection loop at a flow rate of 1 ml/min. During this procedure monoclonal antibodies remain attached to the column matrix, while unbound proteins were washed out. After it the antibodies were eluted by a linear NaCl-gradient from 0% to 30% AEC-buffer B (20 mM $NaPO_4$,1 M NaCl, pH = 6,5) in 25 min at a flow rate of 1 ml/min. The fractions were collected in 1 ml per tube using an auto sampler. The purity of various IgG samples was checked using sodium dodecyl sulfate polyacrylamide gel electrophoresis (SDS-PAGE). The final concentration of polyacrylamide solution was 10%. Aliquots of each samples were boiled for 10 min and were loaded on the electrophoresis gel. After separation, the gel was stained with Coomassie Brilliant Blue G 250. The most pure samples were collected together and dialyzed (Spectrapor semi-permeable membranes 6,000 to 8,000 molecular weight cutoff; Spectrum Laboratories, TX) against 50 mM NH_4HCO_3-buffer (decalcified by Chelex 100®). After determining the concentration of each sample by UV-absorption spectroscopy, the samples were aliquoted and lyophilized using Vacufuge®-concentrator (Eppendorf, Hamburg, Germany) and stored at 80 °C.

2.3 CELL PREPARATION

2.3.1 Rod and cone outer segments isolation procedure

Rod outer segments (OS) were mechanically isolated from the retina of *Rana esculenta*. The same procedure was adopted to isolate cones from the retina of zebrafish (*Danio rerio*). Frogs were kept in filtered, running tap water in small tanks at room temperature (20–23 °C).

Adults zebrafish were kept in groups of 8-10 individuals in 50 l aquaria with dechlorinated, continuously filtered fresh water at constant temperature (28 ˚C) and with a photoperiod of 10h:14h L:D. Animal experiments and care were performed in compliance with the Declaration of Helsinki guidelines and approved by a local ethical committee. Before dissection, the animals were dark adapted (~4 hr), anaesthetised by immersion in a tricaine methane sulphonate solution (1 g/l in water) and then decapitated. Both eyes were removed from the head and hemisected. The back half of the eyeball was cut into four pieces that were stored in oxygenated Ringer solution on ice and used when needed. The retina was "peeled" from an eyecup piece and was gently triturated in ~200 µl of Ringer, using a fire-polished Pasteur pipette or fine forceps to obtain the rod outer segment (OS). All these manipulations were made in the dark using infrared illumination and an infrared viewer (Find-R-Scope, FJW Optical Systems, Palatine, IL, USA).

2.3.2 Cell viewing

An aliquot (~2 ml) of the appropriate Ringer solution containing the isolated cells (rods or cones) was transferred to the recording chamber placed on the microscope (TE 300, Nikon,Tokyo, Japan) stage. The preparation was illuminated with an ultra-bright infrared LED (900 nm) and focused on a fast digital camera (C6790-81, Hamamatsu Photonics, Tokyo, Japan) coupled to the microscope. The preparation was then viewed in the frame grabber window generated by the AquaCosmos software package (version 2.5.3.0; Hamamatsu Photonics), which controlled all the camera parameters (as gain, frame rate, binning, etc.) as well, via a PCI board (PCDIG, Dalsa, Waterloo, ON, Canada).

2.4 ELECTROPHYSIOLOGY

2.4.1 Patch-clamp technique

The patch-clamp, voltage-clamp technique consists in the control of the membrane potential across a small area of membrane, or across the entire cell membrane, by measuring the current necessary to maintain the membrane potential equal to that of the command circuit. The main part of the patch clamp amplifier is constituted by a current-voltage converter that makes the membrane potential to follow rapidly the variations of the command potential. The injected current is proportional to the potential drop at the edges of the resistance inserted in the feedback loop of an operational amplifier (Fig. 2.1).

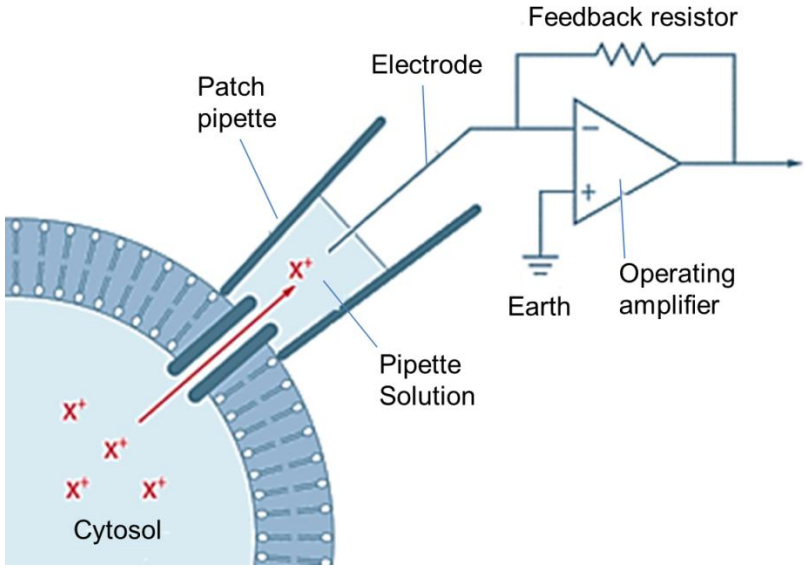

Fig. 2.1. Schematic drawing of the classical cell attached configuration.

The membrane patch is isolated by pressing the clean and smooth tip of a glass pipette on the surface of the cell membrane to obtain a seal between the pipette and the membrane (the adhesion can be so tight that the seal resistance, i.e. the electrical resistance between the pipette lumen and the external solution, can exceed 10 GΩ). Under these conditions (*cell-attached* configuration), the current flowing through the ion channels enclosed by the pipette tip is almost entirely collected by the patch-clamp amplifier, since the tightness of the gigaseal prevents that a significant portion of this current leaks out the pipette toward the earth electrode (Fig. 2.1). When the *cell-attached* configuration is obtained (Fig. 2.2*A*), the pipette can be pulled-away and a patch of membrane can be excised from the cell, forming the *inside-out* patch-clamp configuration (Fig. 2.2*D*). In this configuration the internal membrane surface is exposed to the bath solution. Once the *cell-attached* configuration is obtained, the membrane patch can be perforated through the application of negative pressure to obtain the *whole-cell*

configuration (Fig. 2.2*B*). Under this condition, the current flowing through the entire cell surface can be recorded, and the intracellular solution is rapidly dialysed by the pipette solution, giving a control of the internal composition of the cell. From the latter configuration, by slowly withdrawing the pipette from the cell, the patch of membrane at the tip reseals with the outer surface exposed to the bath solution, and the internal surface exposed to the pipette solution (*outside-out* configuration; Fig. 2.2*C*) (Hamill et al., 1981).

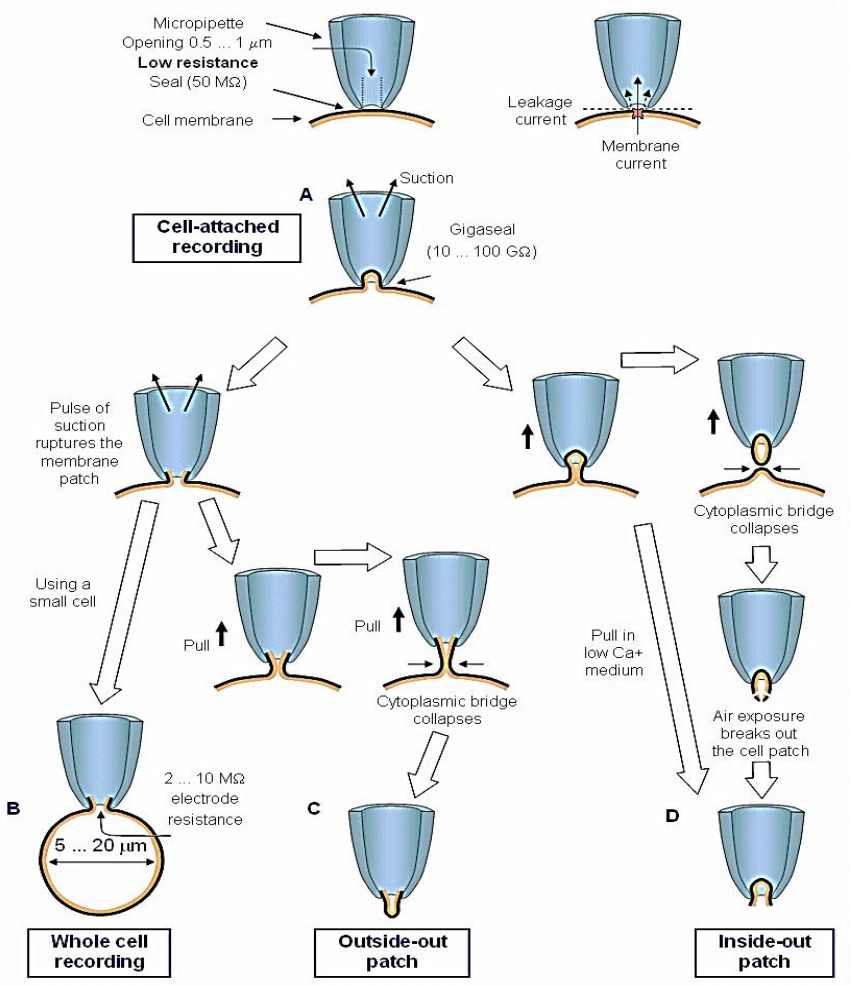

Fig. 2.2. Schematic illustration of the four different methods of patch clamp: ***A*** cell-attached recording, ***B*** whole cell configuration, ***C*** outside-out configuration, and ***D*** inside-out configuration. (Hamill et al., 1981)

2.4.2 Pressure polish setup

Patch pipettes were pulled in the conventional manner from 50 or 100 µl borosilicate glass microcaps (Drummond, Broomall, PA, USA), with a vertical puller (model PP-830, Narishige, Tokyo, Japan), and tightened into a pipette holder. The latter was clamped to the microscope stage, and a three-way valve allowed to connect the pipette to a pressurized air line (set to ~4 atm and filtered to 0.2 µm to avoid pipette clogging), or to vent it to air (Fig. 2.3).

The pipette holder was moved by means of the XY manipulator of the microscope stage, to center the pipette tip into the central bend of an "omega" shaped, glass-coated platinum filament (50 µm of diameter; Fig. 2.4). This shape ensured the homogeneous softening of the pipette shank, when the filament was heated by passing a constant current through it. To avoid metal evaporation onto the pipette, the filament was uniformly glass-coated by dipping it in borosilicate glass powder when heated to yellow color. The filament was tin soldered to a copper holder (that functioned also as a heat sink, Fig. 2.4) mechanically coupled to a micromanipulator, and electrically connected to a variable current generator via a "push-to-make" switch.

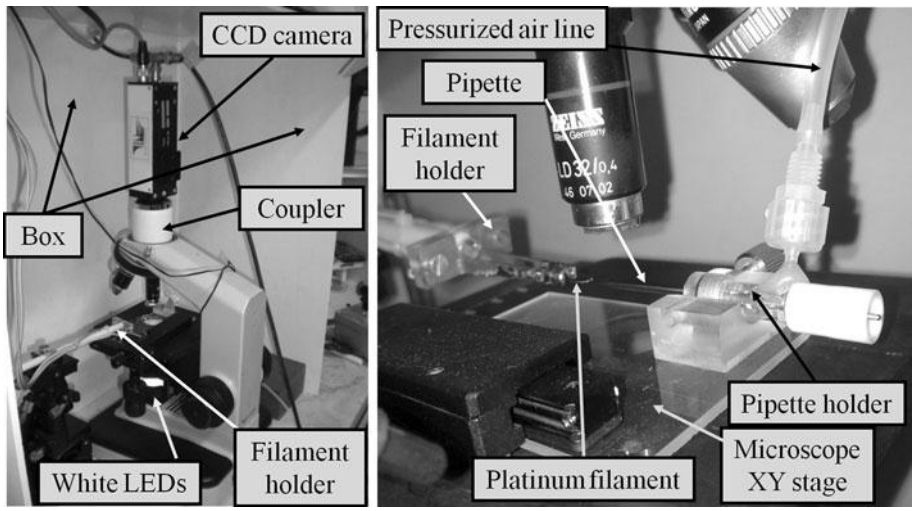

Fig. 2.3. Set-up to fabricate the pressure-polished pipettes. *Left* View of the microscope, the camera coupled to the objective nosepiece, the microscope stage, the filament holder, the LED illuminator, and the box; *right* closer view of the microscope stage, the pressurized pipette holder, and the platinum filament.

To produce the adequate heat to soften the pipette tip (i.e. the filament was brought to reddish color), the current was typically set to ~1.2 A for filaments shaped as shown in Fig. 2.4. The pressure polishing set-up was enclosed in a box, to protect the filament from air currents, that could strongly affect the filament temperature as well, and the entire set-up from dust. The optical field containing the filament and the pipette was viewed on an LCD monitor connected to a contrast-intensified CCD camera (VX 44, Till Photonics, Gräfelfing, Germany), that replaced the objective turret of a bright-field stereomicroscope (YS2-T, Nikon). The video signal was also digitized on-line (by Pinnacle Studio MovieBox DV, Avid, Burlington, MA, USA) and stored on a computer, to have a record of the time course of the pipette shaping process.

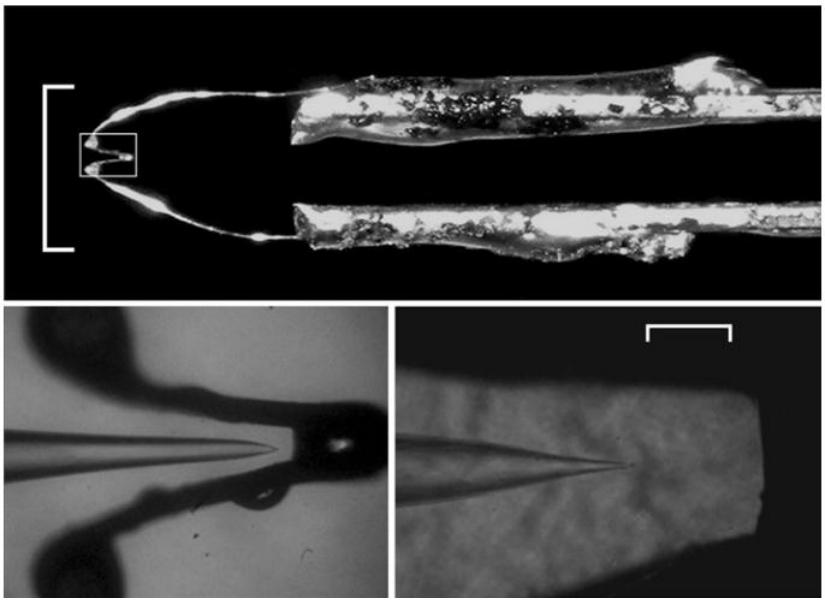

Fig. 2.4. Filament shape and pipette alignment. *Top* Shape of the glass-coated platinum filament tin-soldered to the holder; *scale bar* 5 mm. The region within the *white box* is enlarged at *bottom left*, where a pipette is shown properly aligned with the filament to ensure uniform pipette heating, at the end of a mild pressure polishing. The ‘‘omega’’-shaped region of the filament is enlarged at *bottom right*, where a pipette is shown before pressure polishing, correctly aligned with the filament; scale bar 100 μm.

2.4.3 Pressure polishing procedure and pipette usage

Once the pipette was properly aligned with the filament (Fig 2.4), the box was closed and the air pressure and the filament heating were turned on and off for an appropriate time (to attain the desired pipette shape), with the three-way valve and the push-to-make switch, respectively. The shaping process of the pipette shank and the tip was precisely followed using the calibration grating superimposed on the LCD monitor.

The pipette shank geometry and its tip opening diameter could be finely controlled by adjusting: 1) the relative position of the pipette in respect to the filament, 2) the current intensity passing through the filament, 3) the duration of this current flow, 4) the pressure intensity, and 5) the duration of the pressure application while the current was flowing in the filament. In order to standardize the technique, the most efficient strategy found was to optimize the parameters 1), 2), and 4) and to keep them fixed throughout the pressure polishing process, while the third and the fifth parameters were left to be adjusted each time in order to obtain the desired shank profile and tip opening diameter (Fig. 2.5). Long pressure applications (while the current was flowing in the filament), were used to obtain very enlarged shanks (Fig 2.5*e*). If the pipette opening resulted too large for a given pressure duration, then its tip was heated again in the absence of pressure until the desired size was achieved; if it was instead too

small, then that pressure duration was applied to pipettes pulled with larger tips. Therefore, by carefully regulating the duration of pressure and heating application, the pipette shank was widened as desired, while the tip opening diameter could be increased, decreased or left unchanged.

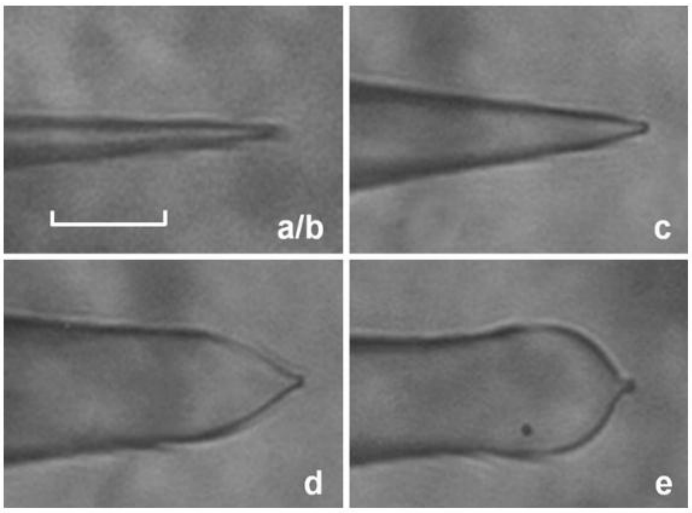

Fig. 2.5. Different pipette shanks obtained with the pressure fire polishing. ***a*** Pulled pipette; ***b*** the same pipette fire polished without pressure (indistinguishable from the pulled one at this magnification); ***c–e*** pulled pipettes similar to ***a***, fire polished with progressively longer pressure durations. Scale bar 20 µm

In order to have a very high rate of sealing on virtually any membrane surface, the pipette must be kept clean: therefore, the microscope stage, the puller and the pipette storage jar were carefully kept dirt free, the pipette holder was often ultrasonicated in distilled water and ethanol (50:50 v/v), and the platinum filament was routinely cleaned with ethanol. Moreover, the microcaps were thoroughly cleaned with ethanol, avoiding to touch them with bare hand especially in their center, i.e. where there will be thinned to form the pipette tips. To keep the pipette in the bath as little as possible, the microscope objective was focused first on the bottom of the chamber while the pipette was in air, i.e. at the "home position" of the step motor micromanipulator (model 5171, Eppendorf, Hamburg, Germany) employed to move the head stage of the patch clamp amplifier (Axopatch 200B, Molecular Devices, Sunnyvale, CA, USA). The chamber was then moved away, the pipette was brought (while still in air) a little above the focus of the chamber bottom, and these coordinates were stored in the micromanipulator memory. The pipette was then returned to the home position, and the chamber was brought back on the objective to search the suitable membrane target. Finally, the pipette was returned to the previously memorized position, that was now just above the membrane target, while holding a strong positive pressure. Once the pipette was close to the target, the strong pressure

was released but a positive pressure was kept by mouth to clean from cellular debris the membrane area where it was intended to seal the pipette, but to avoid at the same time to blow away the target, especially if it was a small isolated cell. This "pressure cleaning" was not however sufficient to remove connective tissue or other organic material strongly sticking on the membrane target: if this was the case, it was necessary to use specific proteolytic enzymes, following known protocols described in detail in the literature.

To provide a quantitative measure of the performances of the pressure polished pipettes, it was measured the bubble number of pulled pipettes (Fig. 2.5*a*) and the bubble number, the ohmic resistance, and the access resistance (measured on frog OS recorded in whole-cell, Fig. 3.12*a-d*; Fig. 3.1) of the pulled pipettes after polishing them with (Fig. 2.5*c*, *d* and *e*) or without (Fig. 2.5*b*) the pressure, for four different representative geometries (Fig. 2.5*b-e*; Table 2.2).

Geometry	BN_i	BN_f	R_p (MΩ)	R_a (MΩ)
a	5.3±0.1	-	5.6±0.7	-
b	5.5±0.2	4.8±0.2	7.0±0.7	26.4±0.8
c	5.8±0.2	5.1±0.1	3.2±0.5	22.7±2.6
d	5.8±0.2	5.0±0.2	2.3±0.2	10±2
e	5.6±0.3	5.1±0.1	2.4±0.2	6.5±1.3

Table 2.2 Quantitative parameters of the patch pipettes. BN_i = initial bubble number after pulling the pipette; BN_f = final bubble number of the polished pipette (with or without pressure application); R_p = pipette resistance in the bath; R_a = access resistance; n=15.

The pipettes of Fig. 2.5 were thoughtfully tested on frog OS, because this was the most critical cell system among the ones tested. Indeed, to have reliably recordings from frog OS, it was necessary to use pipettes with a very small tip diameter (yielding therefore high access resistances if fabricated with conventional methods) to avoid to break the OS, because they were very fragile, had a small diameter (Fig. 3.1; Fig 3.12*a* and *c*) and they were often soiled with retina debris and vitreous humor. The conventional fire polishing reduced the tip opening diameter of the pulled pipette (see column "BN_f" of Table 2.2; n=15 for all pipette geometries),

without affecting the shank profile (Fig. 2.5*b*), resulting therefore in an increased pipette resistance once filled with saline solution (and placed in the bath; see column "R_p" of Table 2.2). The fire polishing increased significantly the probability to gain the seal on all the cells tested, although the access resistance resulted high, especially for the pipette employed for frog OS recordings (Table 2.2). The conventional fire polishing did not improve the sealing capacity of the pipette because it removed any contaminants left on tip, after coating with insulating agent (to reduce the capacitance between the pipette interior and the bath), as proposed by many authors, because no coating was used in these experiments and because the pipette was already perfectly cleaned. The fire polishing rather thickened the wall, and smoothed the surface, of the pipette tip, that is expected to be quite rough (at the molecular level) after it was abruptly separated from its companion following the pulling procedure. It is conceivable that a larger membrane surface sealed on the smoother and thicker glass surface in respect to the rough and thin one of the pipette just pulled, resulting in an increase of the seal resistance. This view is also supported by the following observation: occasionally, when a large bleb was formed once gaining the seal (that was about in the GΩ range) with pipettes or cells not perfectly clean, or with pipettes not fire polished, most of this bleb could be expelled out of the pipette, by applying a positive pressure, without any change in the seal resistance. This indicates that the portion of the glass tip that sealed on the membrane and this membrane itself formed very stable assemblages, around which the lipids that did not sealed on the glass could flow quite freely. If the seal was instead very good (seal resistance >20 GΩ), by using fire polished pipettes unsoiled by bath debris and on clean cell surfaces, i.e. a much larger glass surface have sealed on the membrane, usually it was not possible to eject the bleb, unless the applied pressure inside the pipette was so large to lose the seal.

By carefully regulating the duration of pressure and heating application, the pipette shank was widened as desired, while the tip opening diameter could be increased, decreased or left unchanged, resulting for pipettes as shown in Fig. 2.5*e* in a 4-fold reduction of access resistance in respect to the conventional ones (Fig. 2.5*b* and Table 2.2). As expected, for a fixed shank geometry, as the pipette tip opening was made larger, the bubble number increased, while the pipette and access resistance decreased. However, pressure polished pipettes with similar bubble number and resistance (Table 2.2), but with very different shanks and tip openings, gave quite different access resistances. Therefore, to reproduce a desired pipette geometry, it was necessary to rely on the bubble number of the pulled pipette (that was fabricated always with the same shank) and on the pressure polishing parameters (i.e. heating and pressure durations), rather than on the bubble number of the polished pipette only.

2.4.4 Sealing virtually on any membrane with just one glass type

Surprisingly, the chosen borosilicate glass was extremely good at attaining tight seals on an extremely wide variety of cells, being isolated or inserted in small tissue fragment or slice, or on giant unilamellar vesicles (GUVs) of many different lipid composition (Benedusi et al., 2011). Therefore, it was not true, as commonly believed, that different type of glass work better on different cell types (Penner, 1995). Moreover, at difference with that reported in the literature (Coronado, 1985), it was possible to routinely gain seals exceeding 10 GΩ with GUVs made up to 90% of phosphatidylcholine. Therefore, when there was a failure at attaining a seal, it was because the patch pipette tip was soiled, and/or because the membrane target was contaminated with cell debris, connective tissue or other organic material, not because the glass type was inappropriate. The day-to-day variability in attaining the seal was therefore entirely due to the cell quality (soiled or too fragile to sustain the sealing process), not to some uncontrollable parameter in the pipette fabrication. Indeed, if the protocol described in paragraph 2.3 was strictly followed, the pressure polishing set-up was maintained dirt-free, the pipette was kept in the bath as little as possible (to avoid that cell debris soiled the tip while approaching the cell), and the membrane target was "pressure cleaned", the seal was guaranteed. Moreover, it was sometimes possible to gain a seal with the same pipette more than once, especially when the cell extracellular matrix was broken down with enzymatic treatment providing to move as quickly as possible while going from one cell to the other, to avoid to soil the pipette. Although the seal resistance was constantly decreasing from one trial to the other, it was possible to have seal resistances above 1 GΩ up to the fourth consecutive seal with the same pipette. To refrain that the lack of seal was not due to the pipette (if properly fabricated) but to the cell quality, it was observed many times on enzyme-treated or cultured cells that, if the first seal attempt was unsuccessful, it was still possible to attain the seal with the *same* pipette on another cell. Finally, at difference with what reported by many authors, but in agreement with Priel (Priel et al., 2007), it was found that at physiological pH, the presence or the lack of Ca^{2+} in the patch pipette was not necessary to promote the seal. Indeed, it was possible to routinely gain the seal with patch pipette filled with solutions containing up to 30 mM BAPTA or 30 mM Ca^{2+} (Rispoli, 1998) in the latter case, it was obviously not possible to attain the whole-cell recording, because cells underwent immediately in apoptosis but the OS, since they are not endowed with Ca^{2+}-dependent proteases.Given the "sealing power" of the

glass pipette mentioned above, the pressure polishing technique was optimized just for this glass type.

2.4.5 Intrapipette perfusion

The enhanced cell dialysis obtained with the pressure polished pipettes allows to control the delivery of exogenous molecules in the cytosol with the following intracellular perfusion system. The test solution is applied in the lumen of a pressure polished pipette by ejecting it out of a pulled quartz (or plastic) tube, which can be positioned very closed to the pipette tip, respect to conventional pipette (Fig. 2.6)

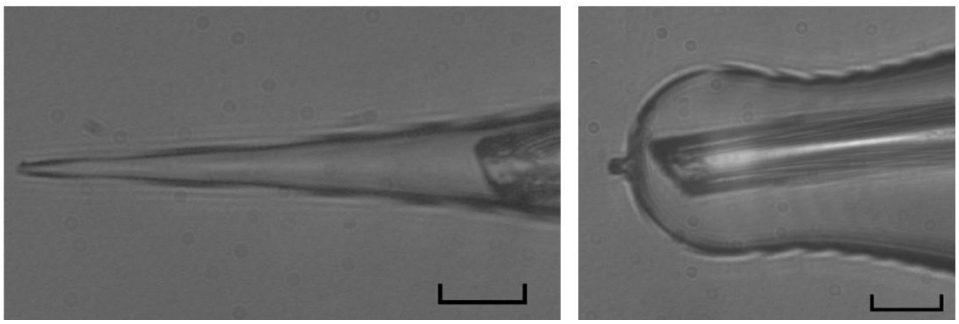

Fig. 2.6. A pulled quartz tube is positioned inside the lumen of a conventional pipette as close as possible to its tip (*left*); the same tube is inserted in a pressure polished pipette (*right*). Scale bar is 20 μm

The other end of the quartz tube is tightly inserted into a Teflon tube that comes out of the pipette, and then out of the holder, through a side-port (Fig. 2.7). This Teflon tube is connected to one of the port of a couple of "three-way" valves with low dead volume. These valves are also connected to: a syringe (containing the test solution, in red; Fig. 2.7), a tube ending in a waste container (wash line), and a precision pressure generator. The solution change protocol is as follows: the patch pipette (not yet in the bath) is filled first with the control solution (shown in green, Fig. 2.7), applied manually with a syringe, by using the valve configuration illustrated in Fig. 2.7. The pipette is then moved into the bath to attain the gigaseal on the membrane target and the desired patch clamp configuration (cell attached, whole-cell or excised patch).

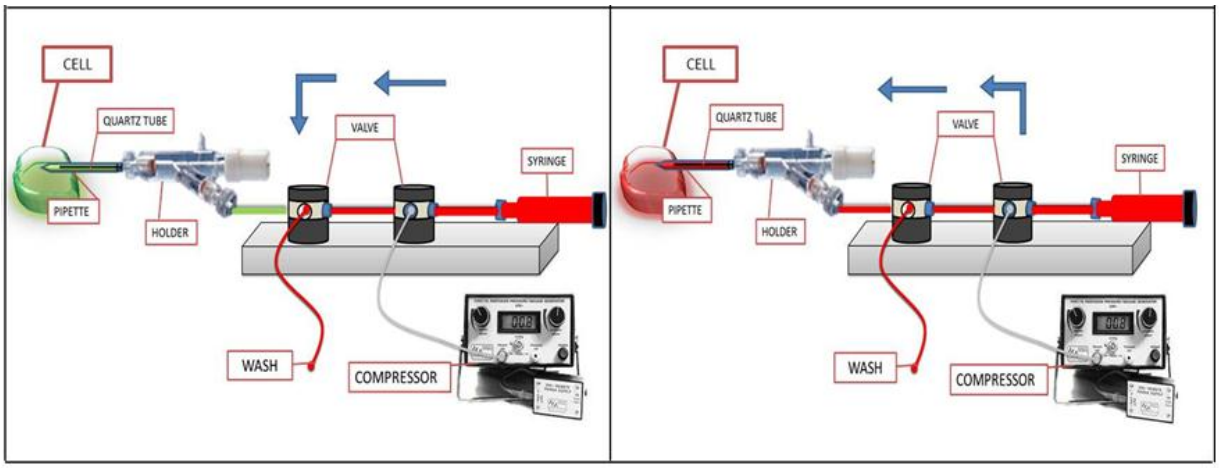

Fig. 2.7. Intracellular perfusion system. Valve configuration schemes: to wash the perfusion lines with test solution (in red; *left*) and to substitute the control solution (in green) filling the patch pipette with the test solution (*right*).

The perfusion lines are then filled with a test solution by injecting it with a syringe toward the waste container by using the valve configuration illustrated in Fig 2.7, left. In this way the perfusion tubes can be flushed several times with the new solution, in order to remove air bubbles or residues left from the previous solution. The test solution is then applied to the membrane surface or to the cytoplasm (depending upon the patch clamp recording configuration) at a desired time, by switching the valve in the configuration shown in Fig 2.7, right. In this configuration, the test solution is expelled out from the quartz capillary by using a precise pressure generator, so to minimize any mechanical stress on the membrane, resulting in a stable seal during the pipette perfusion.

2.4.6 Fast external perfusion system

After obtaining the whole-cell recording, the OS was aligned in front of a multibarreled perfusion pipette of a fast microperfusion system (Fig. 2.8*a*). The perfusion pipette was moved on a horizontal plane with a precision step motor, controlled by a user-friendly interface (Fig. 2.8*c*) running in a host computer, connected to the microperfusion system via the serial port. The perfusion pipette was constituted of up to six barrels (500 µm of side; two barrels of a four barrelled pipette are visible in Fig. 2.8*a*) made with precision, square glass capillaries glued together. Peptides were applied and removed in ~50 ms (see below) by moving the perfusion pipette so that to switch the whole-cell recorded OS back and forth from a stream of control perfusion solution (usually containing 130 mM of a monovalent cation and 1 mM Ca^{2+}; see Results) to a stream containing the peptide (dissolved in the same perfusion solution). This

strategy allowed to assess the dynamics of the pore formation and the possible reversibility of the process. The temporal lag between the time in which the command (internal or triggered by an external device) moving the perfusion pipette was imparted, and the time in which the solution change effectively occurred, as well as the speed of the solution change, were occasionally measured (since they were very reproducible) as illustrated in Fig. 2.8*b*. At the end of experiment, the cell was blown off the patch pipette with a positive pressure pulse, and the odd perfusion lines were filled with a solution having 50% choline chloride and 50% KCl, while the even perfusion lines were filled with the patch pipette solution. The choline chloride had a different refraction index in respect to all the patch pipette solutions used, therefore the boundary separating two adjacent streams was clearly visible (see the three still frames of Fig. 2.8*b*).

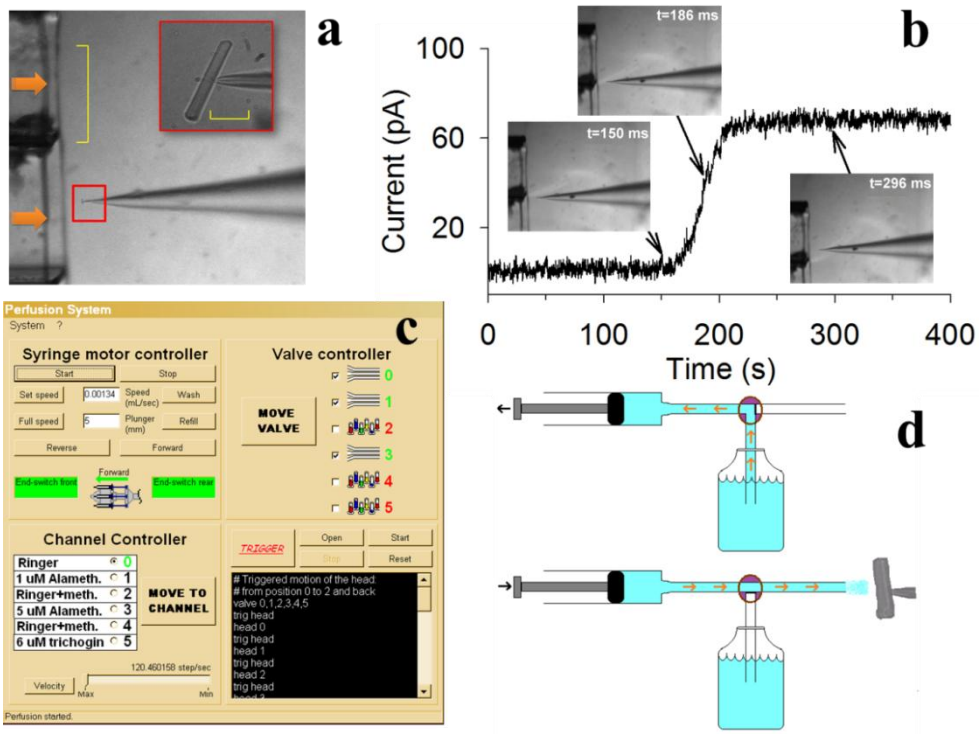

Fig. 2.8. The technique employed to investigate the permeabilization properties of the peptides inserted in a natural membrane. ***a***, isolated rod outer segment (OS) recorded in whole-cell mode (shown enlarged in the *inset*; scale bar is 20 µm) aligned in front of the multibarreled perfusion pipette (scale bar is 500 µm; horizontal orange arrows denote perfusion flows). ***b***, trace shows the current jump upon switching an open patch pipette filled with 130 mM K^++1 mM Ca^{2+} (9 MΩ, V_h=0 mV) from 65 mM choline+65 mM K^++1 mM Ca^{2+} to 130 mM K^++1 mM Ca^{2+}. The two latter solutions had a 0.6 mV junction potential, producing a current jump of 70 pA, lasting ~50 ms, that had the same kinetics of the solution change. This kinetics is also shown by the three still frames (650x494 pixels at 12 bits grey-scale resolution), extracted from a 30 frame/s movie synchronized with the voltage-clamp recording. The boundary separating the two solution streams was clearly visible, allowing a precise electrical and visual correlation of the solution change dynamics. ***c***, user interface of the perfusion apparatus described in Methods. ***d***, scheme of one perfusion line (composed by a syringe, a three-way valve, a cylinder and one perfusion pipette barrel) and perfusion flow (in orange) during syringe refilling (*upper panel*) and during perfusion of an OS recorded in whole-cell (*lower panel*); drawing not in scale.

Since a junction potential was also developed between the two solutions, upon repeating the solution changes previously performed with the OS, a current jump was recorded by the open pipette (voltage-clamped at 0 mV) that had the same kinetics of the solution change (Fig. 2.8*b*). By comparing the electrical and the imaging recordings, it results that the solution change was completed within the 50 ms necessary to the OS to cross the boundary separating two adjacent streams. The perfusion system could be also used to apply to the cell solutions of different ionic composition or containing a specific drug, so that to study, besides the current-to-voltage characteristics, the ion selectivity and blockade of the pore as well. To this aim, all perfusion solutions contained the peptide under study at the same concentration, so that to compare the effects of the test solutions at a constant membrane permeabilization. The solutions flowing in the perfusion pipette were fed by means of precision syringes (Hamilton, Reno, NV, USA), whose piston was moved by a DC motor controlled via the computer interface (*Syringe motor controller* panel, Fig. 2.8*b*). The typical perfusion speed was 15 µl/min, therefore minimal amounts of peptide solution (<500 µl) were required to perform peptide applications lasting more than half an hour. The fine regulation of the perfusion flow speed and of the velocity of perfusion pipette horizontal movements (controlled by the *Velocity* button in the *Perfusion pipette controller* panel) allowed to perform fast solution changes on practically any isolated cell type, or even on small cell aggregates, without any significant change of the seal resistance. This system has been successfully tested on cells mechanically or enzymatically isolated from different amphibian, reptilian, fish, and mammalian tissues, on cultured cells and on giant unilamellar vesicles made with many different lipid mixtures. Depending upon the position of the six three-way solenoid valves (Fig. 2.8*d*; all tubing and valve components in contact with the solutions were made in teflon), each one independently controlled by the *Valve controller* panel (Fig. 2.8*c*), the solution contained in each syringe could be sent to the perfusion pipette (symbolized by the perfusion pipette in the *Valve controller* panel; Fig. 2.8*c*) or redirected to one of the six reservoirs (in which each solution was made, symbolized by a group of cylinders in the *Valve controller* panel). This allowed to save the solutions that were not used, or to avoid that, upon switching between two non-adjacent barrels, the OS was transiently exposed to a third undesired solution. Once emptied, the syringes could be refilled from the cylinders by clicking on the *Refill* button (in the *Syringe motor controller* panel, Fig. 2.8*c*). This command moved the six three-way valves in the cylinder position and backed up the DC motor at full speed until the syringes were filled: the motor was then stopped by an end-position switch; a second end-position switch stopped the motor when syringes were emptied (the status of the

switches was signaled by the *End switch rear* and the *End switch front* indicators in the *Syringe motor controller* panel that turned from green to red). When particularly precious solutions were used, all the perfusion lines were filled with control solution and the connectors to the perfusion pipette were detached and immersed in the vials containing the peptide solutions. The syringe motor was then backed up and the solutions filled just the terminal portion of the tube between the valve and the perfusion pipette. The connectors were replaced and the motor was set to normal operation to apply the solution to the cell. At the end of the experiment, all the perfusion lines could be washed by dipping all the tubes previously dipped in the cylinders, into a container filled with distilled water (or other washing solution, as methanol, ethanol, DMSO, etc.), and clicking the *Wash* button. This command activated the valves and moved the motor back and forth at full speed, so that the syringes were emptied through the perfusion pipette and refilled with the wash solution, a number of times set by the user in a sub-window opened by the *Wash* button (not shown). The timing and sequence of the solution changes (i.e. the direction, speed and travel of the perfusion pipette step motor), the syringe motor speed, start, stop and direction, and each valve position could be also automatically controlled by simple instructions, entered as a text code (visible in white characters in the black window of Fig. 2.8*c*). A set of instructions of arbitrary length could be manually executed in sequence by clicking on the *Trigger* button; each instruction could be executed after an arbitrary delay set by a particular instruction, that would therefore set the sequence timing. Every instruction could be also executed after receiving a trigger pulse from an external device, allowing, for example, the synchronization of the solution changes with the pClamp voltage protocols or with an imaging system (as in the experiments of Fig. 2.8*b*). It was also possible to send out a trigger pulse, after executing a set of instruction of arbitrary length, to synchronize other external devices.

2.4.7 Frog OS recordings, peptides applications and solutions

Frog OS were recorded using the whole-cell configuration of the patch-clamp technique under visual control at room temperature (20-22 °C). The Ringer solution had the following composition (in mM): 115 NaCl, 3 KCl, 10 HEPES free acid [*N*-(2-hydroxyethyl)piperazine-*N'*-(2-ethanesulfonic acid)], 0.6 $MgCl_2$, 0.6 $MgSO_4$, 1.5 $CaCl_2$, 10 glucose (osmolality 260 mOsm/Kg, buffered to pH = 7.6 with NaOH). All chemicals were purchased from Sigma (St. Louis, MO, USA). The current amplitude (recorded employing an Axopatch 200B; Molecular Devices, Sunnyvale, CA, USA) elicited by repetitive -10 mV pulses was used to measure the

seal resistance during cell-attached recording. Once the whole-cell recording configuration was obtained, the current transients produced by these repetitive pulses were used to measure the OS membrane resistance (R_m), the access resistance (R_a), and the membrane capacitance (C_m). Peptides (whose primary sequence are reported in Table 1) were applied and removed in ~50 ms by switching forth and back the OS from a stream of control perfusion solution [composition (in mM): 130 KCl, 1 $CaCl_2$ and 10 HEPES; osmolality 260 mOsm/Kg, buffered to pH=7.6 with KOH] to a stream of containing the peptide (dissolved in the same perfusion solution; see paragraph 2.5). Patch pipettes were filled with the same perfusion solution in order to drive the current just with the holding potential (V_h, that was typically –20 mV). The solution used in the experiments of ion selectivity (reported in the caption of Fig. 3.6, 3.7 and 3.8) were designed to have the same driving force DF for Na^+ and Ca^{2+}, calculated as:

$$DF = \frac{RT}{zF} ln \frac{C_o}{C_i} - V_h$$

Where C_o and C_i are the extracellular and intracellular ion concentration of valence z; R, T and F have the usual meanings and V_h is the holding potential. DF for and Ca^{2+} and Na^+ was -34 mV in the experiment of Fig. 3.7 and -55 mV in the one of Fig. 3.6 (in both experiments V_h=-20 mV and the intracellular solution was: 32.8 mM, 5 mM Ca^{2+} and 90 mM choline). The osmolarity of extracellular and intracellular solutions were adjusted, when needed, with choline (as in the experiment of Fig. 3.7).

The stability of the recording was checked by routinely measuring R_m, R_a, and C_m in control perfusion solution, i.e. before and after each peptide application. Recordings were filtered at 2 kHz via an eight-pole Butterworth filter (VBF/8 Kemo, Beckenham, UK), sampled on-line at 5 kHz by a Digidata 1322A (Molecular Devices) connected to the SCSI port of a Pentium computer running the pClamp 9.0 software package (Molecular Devices), and stored on disk. Data were further low-pass filtered off-line at 200 or 500 Hz using a Gaussian filter, or by using the "running average" routine of SigmaPlot (version 8.0; Jandel Scientific, San Rafael, CA, USA), and analyzed using Clampfit (version 9.0; Molecular Devices). Figures and statistics were performed using SigmaPlot; results are given as means±SEM.

2.4.8 Zebrafish cones recording, light stimulation, intracellular perfusion and solutions

Zebrafish cones were recorded using the whole-cell configuration of the patch-clamp technique under dark-adapted condition at room temperature (20-22 °C). The Ringer solution had the same composition of the frog OS one. The current amplitude (recorded employing an

Axopatch 200B; Molecular Devices, Sunnyvale, CA, USA) elicited by repetitive -10 mV pulses was used to measure the seal resistance, R_m, R_a, and C_m. Patch pipettes were filled with an intracellular solution containing (in mM): 40 KCl, 70 K-Asp, 5 $MgCl_2$, 1 GTP, 5 ATP, 5 HEPES, pH=7.6. The imposed membrane voltage V_h was held constant at –40 mV. The intracellular dialysis of zebrafish cones with solution containing proteins or antibodies, was performed by using pressure polished pipette (illustrated in Fig 2.5c-e) and the intrapipette perfusion system (Fig. 2.7). zGCAP3 and its specific antibodies were dissolved in the intracellular solution at a concentration of 40 µM and 6 µM, respectively. Light stimuli (flashes in the dark and flashes on a background of light) were delivered using pClamp voltage protocols: one of the two analogical outputs of the Digidata 1322A was connected to a calibrated voltage-to-current converter driving an ultra-bright LED (550 nm). The latter was mounted on a miniaturized xyz micromanipulator, that allowed to align and focus the light on the cell through a 60x objective via the binocular port of the microscope (Nikon TE-300). The LED was positioned so that the spot of light was focused and centered on the OS when the OS was viewed in sharp focus by the TV camera. Enough space was left between the LED and the binocular port to host neutral density filters, when required. The voltages generated by the pClamp protocols and the neutral density filters were matched so to have the appropriate light stimulus intensity with currents always falling in the LED linear range (1-10 mA). Recordings were acquired and analysed as described above.

2.4.9 Fluorescence imaging

Besides bright-field viewing of the cells, the camera and the AquaCosmos software were employed for fluorescence imaging experiments as well; the excitation light was generated by a monochromator (Polychrome II, Till Photonics) coupled to the epifluorescence port of the microscope via an optical fibre. The concentration of lucifer yellow (CH, dilithium salt) in the imaging experiments was 350 µM (excitation: 425 nm, emission: 528 nm). The concentration of zGCAP3 labeled with dansyl chloride was ~30 µM (excitation: 280 nm, emission: 400 to 600 nm). The protocol to measure the intracellular spatial and temporal changes of the fluorescence dye are described in the Results.

2.5 SURFACE PLASMON RESONANCE (SPR) SPECTROSCOPY

2.5.1 SPR theory

Surface plasmon resonance (SPR) is described as the resonant, collective oscillation of valence electrons in a thin gold layer, excited by an incident light. The resonance condition is established when the frequency of light photons matches the natural frequency of surface electrons. In the SPR biosensors this thin gold layer is positioned at the interface between two transparent media of different refractive index (glass and water), where a monochromatic and polarized ray of light coming from the side of higher refractive index is partly reflected and partly refracted (Fig. 2.9).

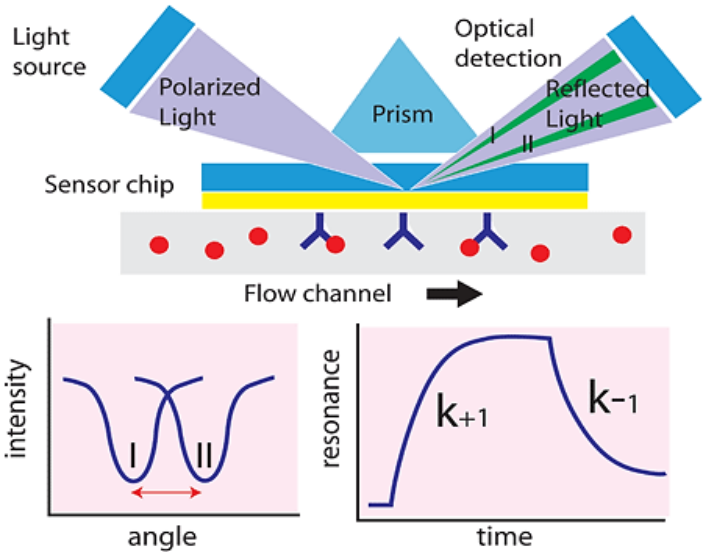

Fig. 2.9. Surface plasmon resonance (SPR) detects changes in the refractive index in the immediate vicinity of the surface layer of a sensor chip. SPR is observed as a sharp shadow in the reflected light from the surface at an angle that is dependent on the mass of material at the surface. The SPR angle shifts (from I to II in the lower left-hand diagram) when biomolecules bind to the surface and change the mass of the surface layer. This change in resonant angle can be monitored non-invasively in real time as a plot of resonance signal (proportional to mass change) versus time. (modified from Cooper, 2002)

Above a certain critical angle of incidence (called "SPR-angle") light surface, plasmons can be excited at the surface of the gold layer thus causing a drop in the reflected light. The angle at which SPR occurs (the SPR-angle) is dependent on the refractive index within a few hundred nanometers of the gold layer surface. The binding of biomolecules to the sensor surface causes a change in the refractive index of the surface and consequentially a shift in the SPR-angle, which is directly proportional to the mass increase. The angular shifts of the SPR-angle are expressed in resonance units (RU) where 1 RU corresponds to a shift of 0.0001°. SPR apparatus is able to measure kinetic rates of molecular interactions between a *ligand*, which is immobilized on the surface of a sensor chip and an *analyte*, which is flowed across the surface

via a microfluidic perfusion system. If interaction between the *ligand* and analyte occurs, the change in refractive index is measured in real time, and the result plotted as resonance units (RUs) versus time (Fig. 2.10). The period during which analyte is being injected to the immobilized *ligand*s on the chip surface, is termed the 'association phase', which is characterized by the association rate constant k_{on}. The equilibrium may be reached when the rate of analyte molecules association with the *ligand* is equal to the rate of their dissociation off the *ligand* (Malmqvist, 1993). When the analyte injection is ceased, begins the 'dissociation phase', which is quantitatively described by the dissociation rate constant k_{off}.

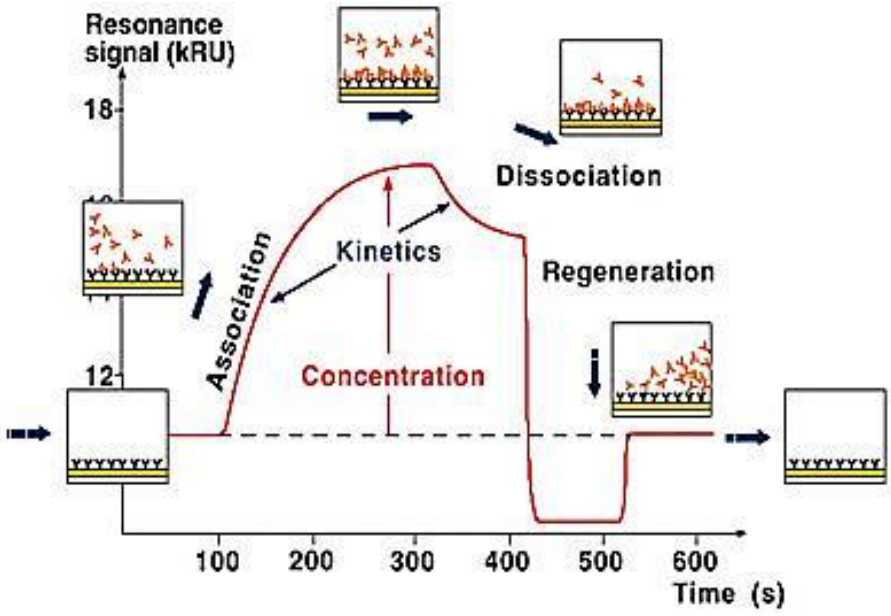

Fig. 2.10. SPR sensorgram of an antibody/antigen interaction showing the establishment of an initial baseline, an increase in response during association, a constant response after equilibrium is reached, and a decrease in response during dissociation. The sensor is then regenerated by a pulse of 0.05 % (v/v) sodium dodecyl sulphate (SDS).

2.5.2 SPR analysis of zGCAP3-antibody interactions

Binding of a selection of monoclonal antibodies to zGCAP3 (immobilized on the sensor chip surface) was investigated by surface plasmon resonance, by using CM-series sensor chips developed by BIAcore AB (GE Healthcare, Uppsala, Sweden), which are characterized by a 100-200 nm thick carboxymethylated dextran matrix attached to the gold surface (Fig. 2.11).

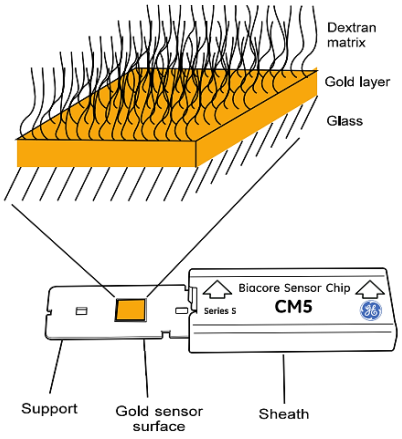

Fig. 2.11. Schematic illustration of the structure of the sensor chip surface on CM-series chips. The chip surface is covered with a matrix of carboxymethylated dextran, a flexible unbranched carbohydrate polymer forming a thin surface layer of approximately 100 nm.

*Ligand*s can be immobilized to the dextran matrix with a variety of covalent bonds via *ligand* functional groups (amino, thiol, aldehyde or carboxyl group): the most common immobilization is by means of ammine coupling. The latter can be realized by activating first the carboxyl groups of the dextran matrix with a mixture of 1-ethyl-3-(3-dimethylaminopropyl) carbodiimide (EDC) and N-hydroxysuc-cinimide (NHS), in order to obtain a reactive surface of succinimide esters (Fig. 2.12).

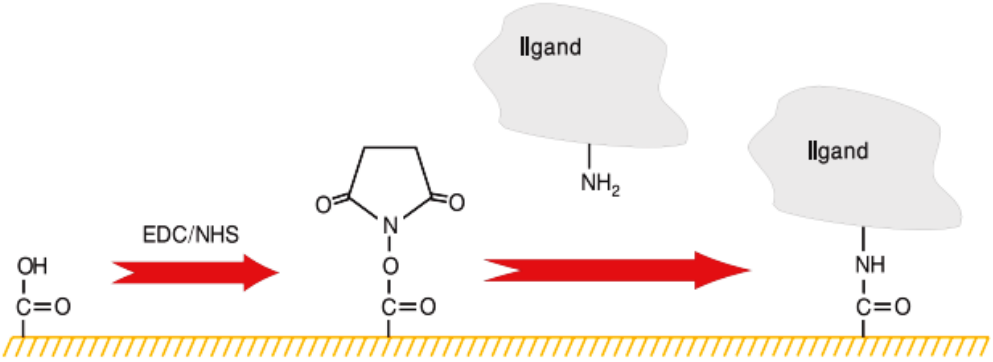

Fig. 2.12. Amine coupling. *Ligand* is linked to the surface through a covalent chemical bond to reactive surface of succinimide esters, which was obtained by reacting EDC/NHS to a carboxyl group.

Ligand is then injected over the dextran matrix surface where succinimide esters are exposed, and becomes immobilized on the surface because its amine group reacts spontaneously with succinimide esters, forming covalent bonds. It is then necessary to inject ethanolamine-HCl to deactivate remaining active groups on the surface, in order to remove non-covalently bounded *ligand*.

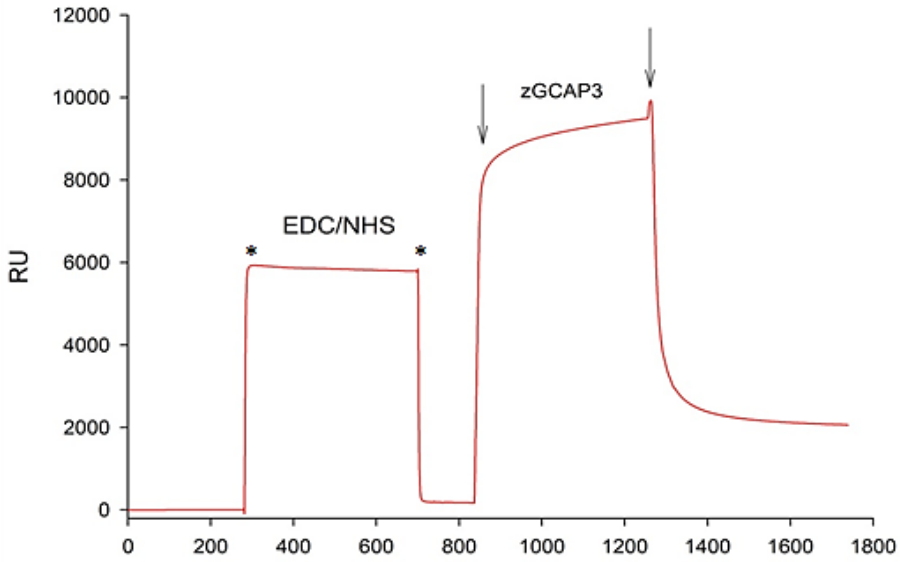

Fig. 2.13. Sensorgram of the activation of the carboxyl groups of the dextran matrix (CM5 sensor chip) with a EDC/NHS mixture (occurring in between the arrows), followed by zGCAP3 immobilization (timing of protein injection is in between red arrows).

The zGCPA3 was immobilized with the above described heterogeneous amine coupling method (Fig 2.13). First, the lyophilized protein was dissolved in bidistilled water (1 mg/ ml) and then it was further diluted in a 10 mM sodium-acetate buffer (pH = 3.0) to a concentration of 25 µg/µl. The surface of the sensor chip was activated by injecting a 7 min pulse of a mixture (1:2) of 50 mM NHS and 200 mM EDC at a flow rate of 5 µl/min. zGCAP3 was then injected for 7 minutes at a flow rate of 5 µl/min to immobilize approximately 2000 RU of covalently bound protein, where 1000 RU correspond to 1 ng protein/mm^2. The affinity of four different IgG1s (i.e. 7E6, 6G9, 6B9, and 4C12) for zGCAP3 was measured. Different concentrations of antibody (0,05 µM to 1 µM in HBS buffer: 10 mM Hepes, 150 mM NaCl,3 mM EDTA and 0.005% Tween20) were injected for 4 min and the dissociation process was monitored for 15 min. The chip surface was regenerated with a pulse of 5ul of 0.05% (v/v) sodium dodecyl sulfate (SDS) at a flow rate of 10 µl/min.

2.5.3 Peptide-membrane interactions monitored by surface plasmon resonance

The interaction between [L-Glu(OMe)^{7,18,19}] and the membrane was investigated through SPR experiments performed with a Biacore 2000 analytical system, using the commercially available L1 sensor chip (GE Healthcare, Uppsala, Sweden).

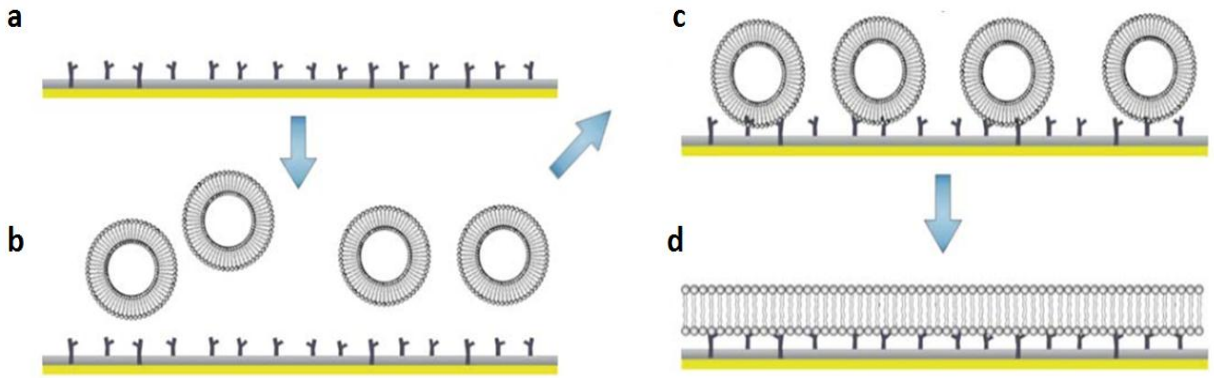

Fig. 2.14. Formation of a lipid bilayer on the hydrophobic anchors of the dextran matrix bound to the sensor chip L1. ***a*** L1 sensor chip surface; ***b*** liposome injection; ***c*** liposome captured on the surface; ***d*** formation of the lipid bilayer. (Hall & Aguilar, 2010)

The latter is characterized by a dextran surface, on which lipophilic residues are covalently attached (Fig. 2.14). These lipophilic anchors are able to capture lipid vesicles and free lipids that can be rearranged to form a lipid bilayer. One of the best advantages of sensor chip L1 technology is the possibility to select the exact lipid bilayer composition and to simulate different biological environments. In this thesis, small unilamellar vesicles (SUV), with the same lipids composition of vertebrate rod outer segment membranes, were immobilized to L1 sensor chip as shown in Fig. 2.15. Before SUV immobilization, the L1 sensor chip was deterged by 10 µl injection of 20 mM CHAPS at a flow rate of 5 µl/min. SUVs were dissolved in 130 mM NaCl, 10 mM Hepes, pH= 7.6 (running buffer) at a concentration of 2 mg/ ml, and 35 µl of this solution was injected on the chip surface at a 5 µl/min flow rate. After SUVs immobilization, 5 µl of 100 mM NaOH was injected at a flow rate of 5 µl/min to remove multilamellar layers. After checking the bilayer stability for 10 minutes, the [L-Glu(OMe)^{7,18,19}] was then injected and, after the association and dissociation constants were measured, the sensor chip was regenerated by removing the lipid bilayer with several injections of CHAPS (40 mM) The peptides were solubilized in the running buffer at concentrations ranging from 200 nM to 2 µM and injected on the immobilized membrane at a flow rate of 5 µl/min for 4 minutes. At the end of each injection the peptide solution was replaced with running buffer for 10 minutes to monitor the dissociation.

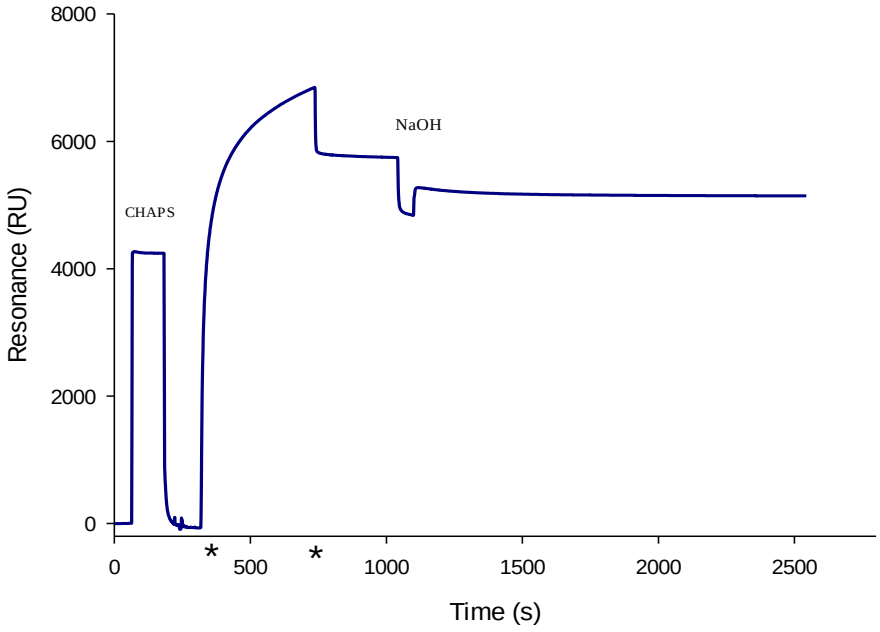

Fig. 2.15. SUV immobilization on L1 sensor chip. The chip surface was first deterged by 10 µl injection of 20 mM CHAPS at a flow rate of 5 µl/min. SUVs were dissolved in running buffer (130 mM NaCl, 10 mM Hepes, pH= 7.6) at a concentration of 2 mg/ ml; 35 µl of this solution was injected at a 5 µl/min flow rate to the chip surface. In the figure the time of SUV injection occurs between the two asterisks. After SUVs immobilization, 5 µl of 100 mM NaOH was injected at a flow rate of 5 µl/min to remove multilamellar layers.

2.5.4 Liposome preparation for surface plasmon resonance experiments

A Lipid composition corresponding to the vertebrate ROS membrane was obtained by mixing: 40% w/w phosphatidylethanolamine (PE), 40% w/w phosphatidylcholine PC, 15% w/w phosphatidylserine (PS) and 5% w/w cholesterol CH (Avanti Polar Lipids). Lipids were dissolved in chloroform and the solvent was evaporated by using a speed vacuum concentrator. The dehydrated lipid samples were stored at -20°C. Before use, the lipid mixture was hydrated in the running buffer (130 mM NaCl, 10 mM Hepes, pH=7.6) at a concentration of 2mg/ ml and sonicated in a water bath sonicator until the solution became clear. SUV were generated using a LiposoFast-Basic system (Avestin, Ottawa, ON; Fig. 2.16) in which the lipid emulsion is extruded repeatedly thorough a polycarbonate filter membrane with a 100 nm pore size, using gas-tight, glass syringes. The sample was passed through the membrane by pushing the sample back and forth between two syringes (MacDonald et al., 1991).

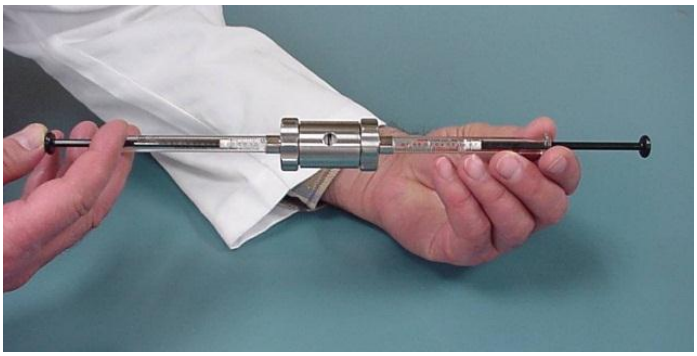

Fig. 2.16. The LiposoFast-Basic produces unilamellar liposomes by the manual extrusion of a multilamellar liposome suspension through a polycarbonate membrane of defined pore size, using gas-tight, glass syringes. The sample is passed through the membrane by pushing the sample back and forth between two syringes.

2.5.5 Fitting of data to interaction models

The sensorgrams of protein-antibody interactions were analyzed by BiaEvaluation software (GE Healthcare) using a 1:1 Langmuir binding model. As a control, the protein was not amine-coupled on a section of the sensor chip, in order to collect the response to analyte injection, that must be subtracted from the sensorgram recorded in the presence of the protein, to obtain the real binding response. The sensorgrams recorded in the dilution series of an analyte where overlapped, and all the baselines were adjusted to zero. To compensate for any bulk effects, the curves obtained in response to the buffer injections only, was subtracted from all the above sensorgrams.

3. RESULTS AND DISCUSSION

3.1 OS endogenous conductances and antimicrobial peptide characterization

The biophysical properties of pore-forming antimicrobial peptides inserted in a natural phospholipid bilayer, were studied by perfusing the peptides on the photoreceptor rod outer segments (OS) mechanically isolated from *Rana esculenta* frogs (see Methods and Fig. 3.1). This particular cell have been found suitable to carry on this study, because of their large size and for the commercial availability and low cost of this edible frog species. Moreover, the vertebrate OS possesses just two endogenous conductances: the main one is the light sensitive (or cGMP) channel, the other one is the Na^+:Ca^{2+},K^+ exchanger (reviewed in Rispoli, 1998). If the OS is illuminated, the light sensitive channels close, while the exchanger can be blocked if just one of the ion species transported by it (i.e. Na^+, Ca^{2+} or K^+) is removed from both sides of the membrane. In this way all the OS endogenous sources of membrane current could be readily blocked, therefore the entire current is entirely flowing through the pore-forming peptides. The ionic currents flowing through the peptide channels, were recorded at a desired voltage by using the whole-cell, patch-clamp technique (see Methods).

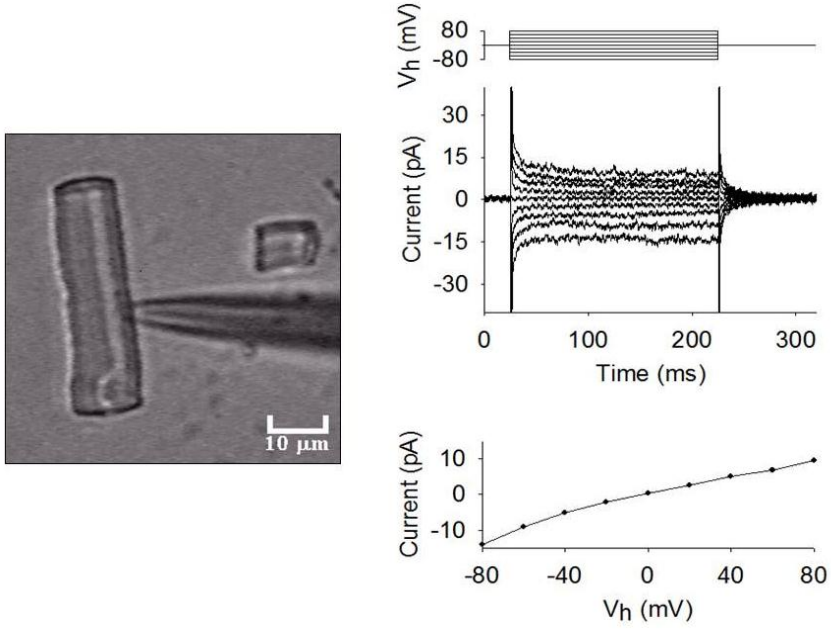

Fig. 3.1. Electrical properties of OS. Frog OS recorded in whole-cell configuration (*left*). *Central right panel*: average whole-cell current recorded from a representative OS under room lights (pipette and external solution: 130 mM K^++1 mM Ca^{2+}), subjected to 5 s voltage steps from –80 mV to +80 mV in 10 mV increments (*top right panel*) starting from V_h=0 mV and repeated 10 times; *lower right panel*, the average current recorded for each voltage step shown in the *central left panel* is plotted against the voltage step (the resulting current-to-voltage characteristics is linear, giving R_m~8 GΩ).

To simplify the interpretation of the experiments, patch pipettes were filled with the same perfusion solution (that typically contained 130 mM of KCl or 130 mM of NaCl) to ensure the current through the exogenous peptide pore was only driven by the holding potential (V_h, usually set to -20 mV). To preserve the membrane integrity during long recordings, it was necessary to include a physiological concentration of Ca^{2+} (1 mM) to the external solution. Therefore, 1 mM Ca^{2+} was added to the intracellular solution as well, to ensure that the current was still entirely driven by V_h. Under these ionic conditions and under room lights (that will close all the light-regulated channels), the OS membrane resistance (R_m) was usually larger than 1 GΩ in the absence of the peptide, exhibiting a linear (ohmic) current-to-voltage characteristics (Fig. 3.1). The high signal to noise ratio, given by the large value of R_m, allowed the detection of current signals down to the single channel level. The dynamics of the pore formation was tested by means of the following protocol (shown in Fig. 3.2*a*; 3.3a,*b*; 3.4*a*,b; 3.6; 3.7; 3.8). With the isolated OS continuously held to V_h, R_m was measured before peptide perfusion by means of a brief -10 mV step (indicated with an asterisk in all figures); the peptide was then quickly applied (in about ~50 ms) using the fast perfusion system. Once the current had stabilized, the OS was finally returned to the control solution (without the peptide) to assess the possible recovery of the current, and R_m was again measured. In control solution, repetitive 10 mV pulses were routinely applied to check that R_a was unchanged, otherwise the cell was discarded. In general, the waveform of the current induced by a peptide application and withdrawal can be described quantitatively by the following five kinetics parameters:

1) The activation delay (D_a), defined as the time lag between peptide application and the time in which the current deviates from its baseline (following peptide application), more than three times the noise average fluctuation (indicated by the arrows in Fig. 3.4 *c* and *e*, 3.5*b*, and 3.6*b*);
2) The activation time constant (τ_a), defined as the time constant of the single exponential fit to current activation (Fig. 3.4*a* and *b*, *black* traces);
3) The current amplitude at steady-state (I_{max});
4) The deactivation delay (D_d), defined as the time lag between peptide removal and the time in which the current deviates from I_{max} more than three times the noise average fluctuation;
5) The deactivation time constant (τ_d) defined as the time constant of the single exponential fit to current deactivation (Fig. 3.4*a* and *b*, *black* traces).
6) To avoid errors produced by the noise, the above parameters were measured on the low-pass filtered or on the smoothed traces (see Methods).

3.1.1 Comparison between CM15 and F50/5 permeabilization properties

Application of CM15 at concentrations ≤1 μM gave no detectable macroscopic currents nor single channel events, but currents were routinely obtained at concentrations ≥2.5 μM (Fig. 3.2, 3.3*a*, 3.4*a*, *c*, and *d*). Occasionally, at early times of peptide application at low concentration, current waveform resembled (barely) single channel events (the clearest recording ever obtained is shown in Fig. 3.2.

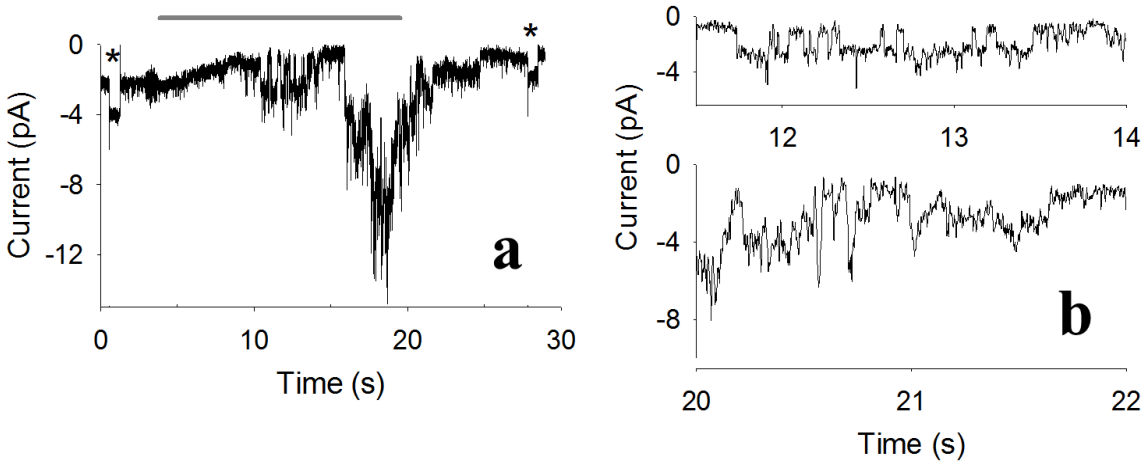

Fig. 3.2. Membrane permeabilization induced by CM15 at early times of recording at low concentrations. ***a***, application for 16 s (*grey thick* line) and withdrawal of CM15 at concentration of 2.5 μM on an OS recorded in whole-cell configuration. The membrane resistance was checked before and after peptide application by means of -10 mV pulses, indicated by the asterisks; V_h was -20 mV throughout the recording. ***b***, enlargements of the recording of *a* 6.6 s after the perfusion onset (*upper panel*) and just after peptide removal from external solution (*lower panel*). To identify the temporal location of the two enlargements, timing of panels in ***b*** follows the one of panel ***a***.

These events were followed by a noisy macroscopic current, that was expected to flow through several pores, which number was progressively increasing up to a steady-state number, as the peptide was continuously applied. It can be argued that the mechanism of pore formation by CM15 occurs according to a barrel and stave model: this requires that a certain number of monomers binds together once in the plasma membrane to form an ion conductive pore (Fig. 1.1.3). If the number of peptide monomers inserted in the membrane is small, as it occurs at early times of peptide application at low concentration, the pores are formed and disaggregated frequently, producing single channel events. However, besides the rarity of the occurrence of these events at early time of the recordings, they were never detected just after peptide removal, as instead expected, since the number of peptide monomers inserted in the membrane should return to be small again. At difference with CM15, low concentrations of F50/5 (and of their

analogs reported in Table 2.1) gave clear and sustained single channel events (Fig. 3.5*c*). Incidentally, these channel events were produced by F50/5 at concentrations as low as 250 nM, showing a much larger efficiency in pore formation in eukaryotic cell membrane in respect to CM15.

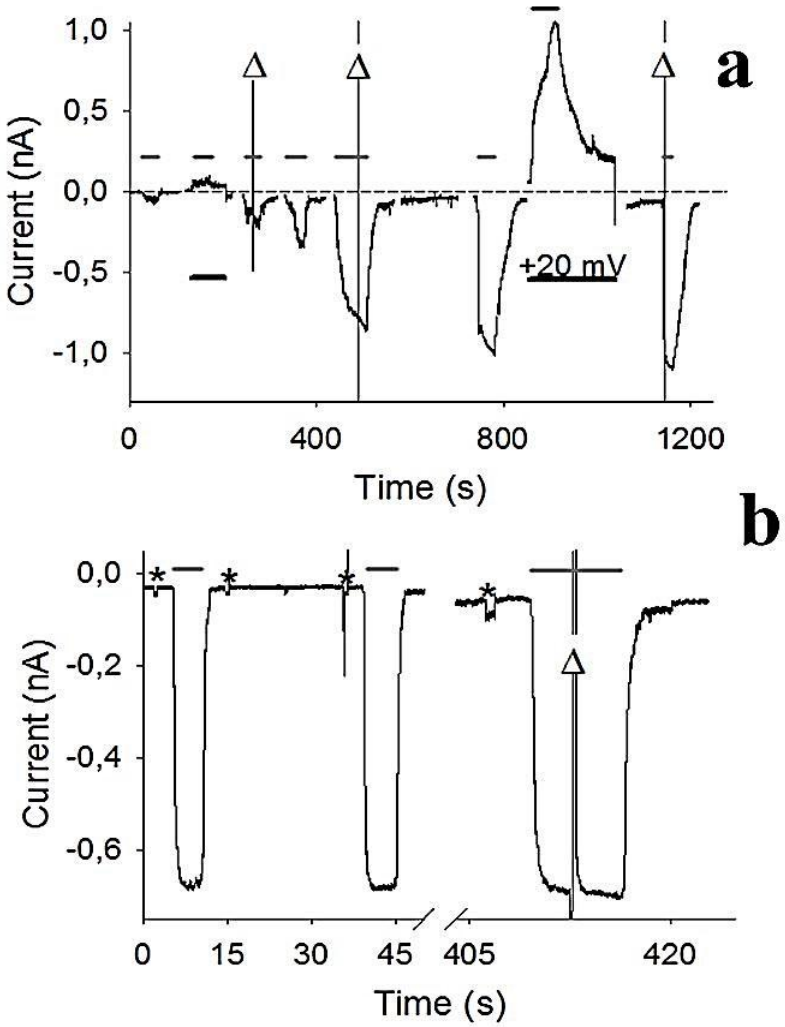

Fig. 3.3. Comparison between the currents elicited by repetitive applications of CM15 and F50/5. ***a***, repetitive applications of CM15 at concentration of 5 µM (*thick grey* lines); V_h was -20 mV but at the *thick black* lines, where it was +20 mV; *dotted* line indicates the zero current at the beginning of recording (i.e. before any peptide application). ***b,*** repetitive applications of F50/5 at concentration of 1 µM at -20 mV. In both panels, the clipped vertical lines, indicated by the symbol Δ, are actually the response to quick voltage ramps (see text) used to construct the current-to-voltage relationships (shown in Fig. 3.4*d*); The membrane resistance was checked before and after peptide application by means of -10 mV pulses, indicated by the asterisks; V_h was -20 mV throughout the recording. The blanks in the recordings in control solution in ***a*** and ***b*** omit the repetitive voltage pulses used to measure R_m, C_m and R_a and/or the response to voltage ramps (a representative one is shown in Fig. 3.4*d*, *thick black* trace).

The CM15 application at concentration of 5 µM gave consistently macroscopic currents (Fig. 3.3*a*) that developed exponentially to a relatively stable level (Fig. 3.4*a*). This level was

not however maintained if the peptide application was lengthen, but current kept slowly increasing throughout the peptide application (Fig. 3.4*a*), at difference with sustained F50/5 perfusion (Fig. 3.4*b*), that produced very stable current. Moreover, repetitive CM15 applications produced currents of increasingly amplitude (Fig. 3.3*a*), but no such increase was ever observed with F50/5 (Fig. 3.3*b*). This again excludes that CM15 permeabilizes the plasma membrane according to a barrel and stave mechanism, since during continuous peptide application at high concentration, membrane peptides are expected to equilibrate with the ones externally perfused, giving a stable macroscopic current, as in the case of F50/5. Moreover, the current did not return to the zero level following peptide removal (Fig. 3.3*a* and 3.4*a*), but it recovered to a plateau level, where R_m was consequently smaller in respect to the one measured before the peptide application. The CM15 concentration was larger, and/or more and more applications were performed (i.e. the larger was the current induced by CM15), the larger was the plateau amplitude and the smaller was the R_m (measured during the plateau phase). This is again in contrast to F50/5, where current and R_m fully recovered (Fig. 3.3*b* and 3.4*b*) following peptide removal. In these experiments, the F50/5 and CM15 concentrations were selected to give currents smaller than 1 nA, since there is a voltage error induced by R_a (that was typically ~10 MΩ in the recordings considered in this chapter) that can be as high as 10 mV at 1 nA of current. The kinetics parameters of current activation and deactivation defined in paragraph 3.1 can be measured from the fittings and the interpolations to the recordings as illustrated in Fig. 3.4*a*, *b*, *c* and *e*. However, these parameters cannot be unambiguously estimated in the case of CM15, since they depend by the current amplitude. For instance, from the first exposure to the last one of Fig. 3.3*a*, D_a progressively decreased from 2.6 s to 0.5 s and τ_d increased from 3.4 to 26.1 s, as the current increased from 50 pA to about 1 nA. To obtain a reproducible value of the kinetics parameters of the CM15-induced current, in order to compare them with the ones obtained with F50/5, CM15 recordings were selected to approximately give current amplitudes comparable to the ones induced by 1 µM F50/5, irrespective of the CM15 concentration and/or the recording time. A representative example of one of these recordings is shown in Fig. 3.4*a* (*thick grey* trace), that is compared to the much faster kinetics of F50/5 recordings (one example is in Fig. 3.4*b*, *thick grey* trace). This strong difference of permeabilization kinetics is better evidenced numerically by the 32-fold larger value of τ_a and τ_d of the CM15 recordings in respect to the F50/5 ones (Table 3.1), obtained by the monoexponential fittings to the activation and deactivation phases of both recordings (shown in Fig. 3.4*a* and *b*, *black* traces). As expected, the average value of D_a (Table 3.1) measured from the CM15 recordings on a fast time scale (indicated by the arrow in Fig. 3.4*c*) was larger than D_a of F50/5 (Table 3.1; Fig.

3.4*e*). Moreover, D_d was not measurable in the case of F50/5 (since the current started to decrease as soon as the solution change was completed), while it was significant in the case of CM15 (Table 3.1). The dramatically slower kinetics parameters of CM15 in respect to F50/5 ones, indicate that it takes a longer time to form pores with CM15 monomers than with F50/5 (i.e. D_a and τ_a of the CM15 are larger than the ones of F50/5). Moreover, once formed, the CM15 pores are more difficult to be disaggregated upon ceasing the peptide supply at the external solution (D_d and τ_d of CM15 are again larger than the corresponding values measured for F50/5).

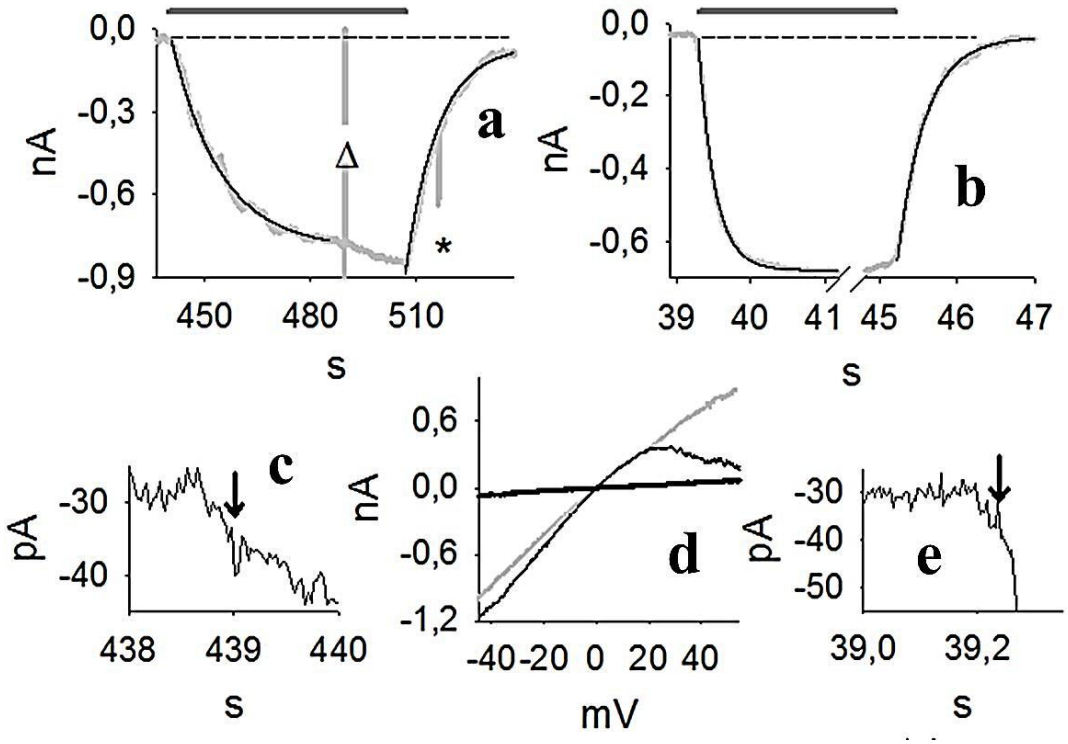

Fig. 3.4. Comparison of the kinetics parameters and the voltage dependence of the currents elicited by CM15 and F50/5. ***a***, the fifth CM15 exposure of Fig. 3.3***a*** (the time scale follows the one of Fig. 3.3***a***) is enlarged and the activation and deactivation of the current are fitted with monoexponential curves, which time constants are τ_a~14 s and τ_d ~9.1 s, respectively. The first two seconds of this trace is further enlarged in ***c***, starting with the time in which the peptide was applied (at ~438 s from the beginning of recording of Fig. 3.3***a***), to show how D_a was measured (indicated by the arrow, D_a~1 s). ***b***, the second F50/5 exposure of Fig. 3.3*b* (the time scale follows the one of Fig. 3.3*b*) is enlarged and the activation and deactivation of the current are fitted with monoexponential curves which time constants are τ_a~0.22 s and τ_d ~0.36 s, respectively. The first 350 ms of this trace is enlarged in ***e***, starting with the time in which the peptide was applied (at ~39 s from the beginning of recording of Fig. 3.3*b*); D_a~0.21 s (indicated by the arrow). ***d***, voltage dependence of the current elicited by CM15 (*thick grey* trace) and by F50/5 (*thin black* trace) subtracted from the leakage, that was measured by applying the same voltage ramp in the absence of peptide (*thick black* trace). D_d was measured for both CM15 and F50/5 with the same procedure shown in ***c*** and ***e***. *Dotted* lines in ***a*** and ***b*** indicate the zero current before peptide application.

In general, as I_{max} and the plateau amplitude following peptide removal progressively increased with repetitive CM15 applications, D_a and τ_a progressively decreased while D_d and τ_d

progressively increased. It is conceivable that the CM15 monomers build up in several regions of the OS membrane to a concentration not enough large to give rise to conductive pores: these peptides may then contribute in forming new pores once the CM15 is applied again extracellularly, giving rise to the observed acceleration of activation kinetics of the current (i.e. decreasing D_a and τ_a). As expected, the resulting progressive build up of the number of conductive channels upon repeating the CM15 applications (that produced the progressive increase of I_{max}), would slow down more and more the deactivation kinetics (i.e. increasing D_d and τ_d), since larger the number of channels (that are also more stable than the ones produced by F50/5), longer it takes to disaggregate them when ceasing the CM15 supply from the external solution. Collectively, all data presented so far exclude a barrel and stave model of pore formation of CM15, while they strongly support this model of permeation in the case of the F50/5. Moreover, the cell integrity and the substantial recovery of current, observed for CM15 applications and withdrawal at concentrations as high as 10 µM (data not shown), exclude the carpet mechanism of membrane permeabilization at concentrations smaller than 10 µM, because micellation would produce the irreversible disruption of the membrane and cell lyses.

Parameter	**CM15 (n=6)**	**F50/5 (n=10)**	**[L-Glu(OMe)^{7,18,19}] (n=9)**
D_a **(s)**	0.8±0.2	0.21±0.03	1.7±0.4
τ_a **(s)**	8.4±1.4	0.26±0.02	4.1±0.8
I_{max} **(nA)**	0.51±0.05	0.70±0.03	0.74±0.20
D_d **(s)**	0.6±0.2	0	0
τ_d **(s)**	10±2	0.31±0.02	1.9±0.6

Table 3.1 Kinetics parameters of current elicited by CM15, F50/5, and [L-Glu(OMe)^{7,18,19}].

It is however conceivable that, at high concentrations, CM15 could irreversibly permeabilize the membrane, by producing micellation according to the mechanism described in Fig. 1*f*. It therefore can be concluded that CM15 permeabilizes the membrane according to a toroidal model of pore formation. This view is also supported by the voltage-independency of CM15 membrane permeabilization, in contrast to F50/5, that instead inserts in the OS membrane at

negative voltages (Fig. 3.4*d*). Indeed, CM15 application at +20 mV or -20 mV produced currents with similar I_{max} (and D_a, D_d, τ_a, τ_d as well; Fig. 3.3*a*). However, the latter protocol is not suitable to assess the precise voltage dependency of the current, since the current progressively increases with repetitive applications of CM15 (note that the maximal current amplitude at +20 mV in Fig. 3.3*a* is larger in respect to the one recorded at -20 mV). To circumvent this problem, rapid voltage ramps (slope: 0.25 mV/ms) were applied during CM15 perfusion at V_h=-20 mV, once the current stabilized for a period at least as long as the ramp (400 ms). To avoid the loss of voltage control due to R_a at extreme voltages (-60 and +40 mV, where current may became very large), cells were selected to have currents of about 100-200 pA at V_h=-20 mV. The response to the voltage ramp during CM15 perfusion was subtracted to the response to the same voltage ramp recorded in control conditions (i.e. in the absence of peptide; Fig. 3.4*d, thick black* trace) to obtain the current-to-voltage relationship corrected for the leakage (Fig. 3.4*d, thick grey* trace). Relationship was almost perfectly ohmic for physiological voltages, in all cells examined (n=6), in contrast with the strong inward rectification of the current-to-voltage relationship (corrected for the leakage) produced by F50/5 (Fig. 3.4*d, thin black* trace, n=16), obtained with the same voltage protocol used for CM15. Therefore, it is required a particular orientation of the F50/5 monomers (attained with the voltage) to form a conductive channel, while the CM15 monomers permeabilize the membrane regardless their orientation. This again supports the barrel and stave model for F50/5 and the toroidal model for CM15.It can be argued that the pore formation according to the toroidal model could be ascribed to the relative abundance of lysine and/or leucine in respect to other aminoacids present in the CM15 sequence. Alternatively, the CM15-induced permeabilization might be due to some aspecific effect produced by the interaction of one or more of its aminoacids with some membrane protein/s. These possibilities were however ruled out because a random sequence of the CM15 aminoacids, (as the "scrambled" CM15; Table 2.1 in Methods), was not able to produce any permeabilization, even for repetitive applications at 10 µM concentration (lasting up to 3 min; n=3 OS; data not shown). Therefore, it is concluded that CM15 must be lined up in a precise sequence to produce efficient membrane permeabilization.

3.1.2 F50/5 monomer assembling mechanism

The barrel and stave model of pore formation requires that a certain number of peptide monomers binds together to form a functioning pore. The hydrophilic glutammine residues at

positions 7, 18 and 19 of F50/5 are supposed to face the pore lumen and form hydrogen-bonded rings, therefore they are expected to play a key role in channel formation. To examine the role of these residues in the pore formation, the three glutammine residues, were substituted with a glutamic acid, in which a methyl ester group was linked to the carboxyl function in the γ position. The synthetic analog [L-Glu(OMe)^{7,18,19}] was applied to the OS with the same protocol used to study the F50/5. Surprisingly, 1 μM concentration of [L-Glu(OMe)^{7,18,19}] produced a current as large that induced by F50/5, showing that these residue substitutions do not prevent pore formation. However, D_a and τ_a of current elicited by [L-Glu(OMe)^{7,18,19}] were ~8-fold and ~16-fold, respectively, larger than those of F50/5 (Table 3.1). Moreover, as the current developed, there was a much larger noise increase in respect to F50/5, indicating that [L-Glu(OMe)^{7,18,19}] may form fewer channels, but with a larger single channel conductance, than those generated by F50/5. The latter peptide applied at 250 nM concentration on the OS produced single channel events of several amplitudes, being not a simple multiple of a fixed size. Analysis of traces displaying very few channels (as the one shown in Fig. 3.5*c*, *upper panel*) allowed to estimate the smallest average single channel size, that resulted of ~50±8 pS at -20 mV (3500 events averaged in 3 cells). As expected, the single channel events produced by [L-Glu(OMe)^{7,18,19}] at concentration of ~250 nM, were much larger than the F50/5 ones. Many different event amplitudes were produced by [L-Glu(OMe)^{7,18,19}], and some were so fast that they were cut by the patch-clamp amplifier, even when filtering as high as 2 KHz (Fig. 3.5*c*, *bottom panel*, *grey* trace). Since the majority of the events were anyway much slower, in order to compare the single channel amplitude of [L-Glu(OMe)^{7,18,19}] with the one of F50/5, these very fast events were usually cancelled out upon low pass filtering the traces at 100 Hz (Fig. 3.5*c*, *bottom panel*, *black* trace). The distribution of current amplitudes (Fig. 3.5*c*, *bottom panel*, *right*) showed that the most probable amplitude was 310±30 pS (820 events, n=3), but events of smaller sizes (as 260 pS) were recorded as well. For both peptides, current bursts occurred at very irregular intervals, making it impossible to systematically investigate interval duration, and measure key parameters as the open probability and the average open and closed time of the channel levels. The range of single channel amplitudes indicates that a channel is probably formed by several peptides assembled together, and various configurations of the peptide assembly are possible, depending upon the voltage, the peptide concentration and the duration of peptide application. The slower kinetics of current activation formed by [L-Glu(OMe)^{7,18,19}] may simply reflect the smaller probability to assemble such large conductance channels. Consistently with this view, single channel events were recorded after ~20 s of [L-Glu(OMe)^{7,18,19}] application to the OS (V_h=-20 mV), instead of ~5 s as in the case of F50/5.

Similarly to F50/5, the current fell to zero without any delay in respect to [L-Glu(OMe)^{7,18,19}] removal time, therefore this analog also does not stably integrate into the plasma membrane. Moreover, the current-to-voltage relationship of [L-Glu(OMe)^{7,18,19}] was almost identical to the F50/5 one (shown in Fig. 3.4*d*, *thin black* trace).Incidentally, the fact that the current elicited by F50/5 and by its analogs fell from several hundreds of pA to the single channel level following a 4-fold reduction of peptide concentration, and that the peptide-elicited current fell to 0 within a few hundred of ms following peptide removal from the external solution (see, for example, Fig. 3.5*a* and *c*), indicate that the pore formation and disaggregation are very fast and cooperative events.

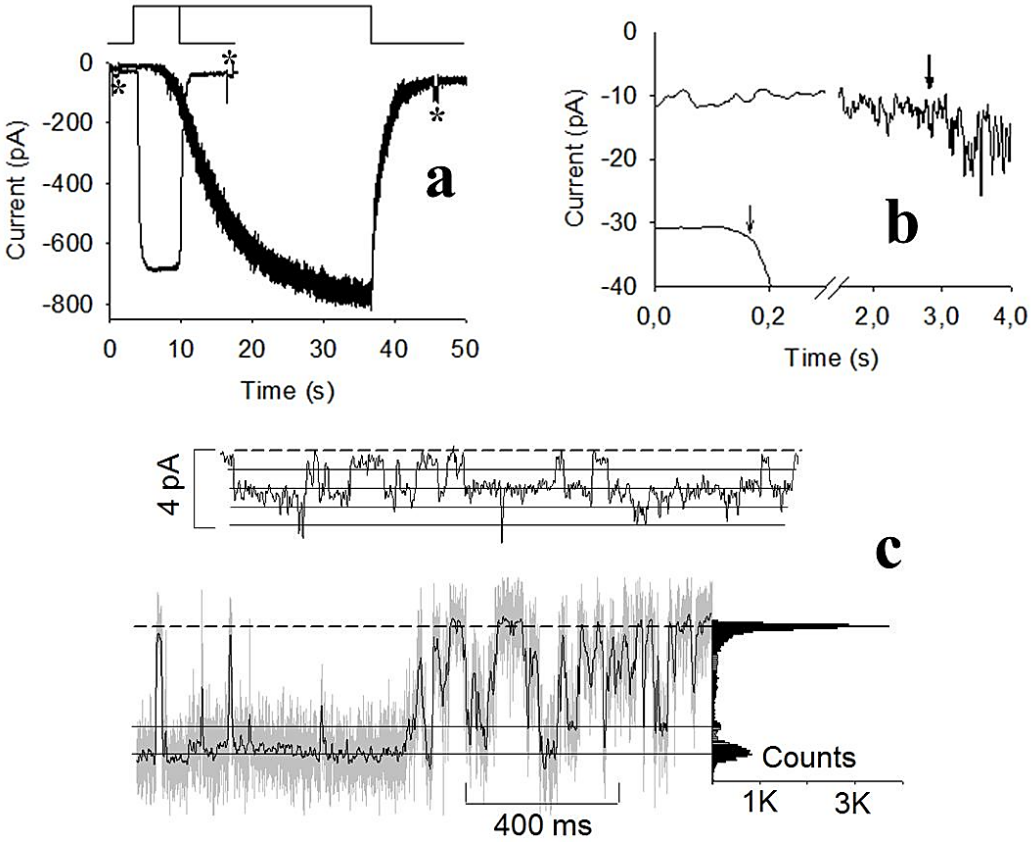

Fig. 3.5. Kinetics of OS membrane permeabilization induced by synthetic F50/5 and its [L-Glu(OMe)^{7,18,19}] analog. ***a***, *upper* traces, timing of application and withdrawal of peptides at 1 μM concentration; *lower* trace, the voltage-clamp, whole-cell current recordings from one OS perfused with F50/5 (*thin* trace) and with [L-Glu(OMe)^{7,18,19}] (*thicker* trace). Asteriscs indicate the occurrence of the two –10 mV voltage pulses (superimposed to V_h=-20 mV), used to measure R_m, that was about 1 GΩ before, and 20 s after, peptide application in both OS. ***b***, the whole-cell current recordings of ***a*** are smoothed to accurately measure the activation delay, indicated by the arrows, that is 0.17 s for F50/5 and 2.8 s for [L-Glu(OMe)^{7,18,19}], computed from the solution change (that occurs at time 0 in this plot); the other kinetics parameters were, respectively: τ_a (0.21 s and 7.4 s), τ_d (0.29 s and 1.6 s), and I_{max} (700 pA and 760 pA at V_h=-20 mV; see Table 3.1). ***c***, *upper panel*, single channel events produced by F50/5; *lower panel*, *left*, channel activity produced by [L-Glu(OMe)^{7,18,19}] low-pass filtered at 2 KHz (*grey* trace) and at 100 Hz (superimposed *black* trace). *Right*, cumulative current amplitude distribution. Both recordings of ***c*** have the same scales and V_h=-20 mV; *continuous* and *dotted* lines indicate the most probable single channel amplitudes and 0 pA, respectively.

For all peptide tested, the D_a, I_{max}, τ_a, and τ_d recorded in symmetric Na^+ were very similar to those reported in Table 3.1 (i.e., recorded in symmetric K^+; data not shown).All the above findings show that F50/5 and its analog [L-Glu(OMe)^{7,18,19}], although exhibiting a very different kinetics of pore formation, retain the poor cation selectivity and the voltage dependency, that are typical features of peptaibiotics. The peptaibiotics constitute therefore the most ancestral form of ion channel, since all the voltage gated channels, the *ligand* gated channels and the gap junction found in all eukaryotic cells, are formed by several α-helices that pack together around a central ion conducting pore.

3.1.3 Role of divalent cation in [L-Glu(OMe)^{7,18,19}]-membrane interaction and pore formation

The relative selectivity for monovalent and divalent ions of [L-Glu(OMe)^{7,18,19}] pores inserted in vertebrate OS, was studied by comparing the current elicited by this peptide in the presence of Na^+ and in the presence of an equiosmolar concentration of Ca^{2+}. [L-Glu(OMe)^{7,18,19}] pores resulted permeable to both divalent and monovalent cations, but there was a strong and unexpected difference in the kinetics with which the current increased, attained a steady state level, and returned to zero in response to the peptide application and withdrawal from the external solution (Fig 3.6).

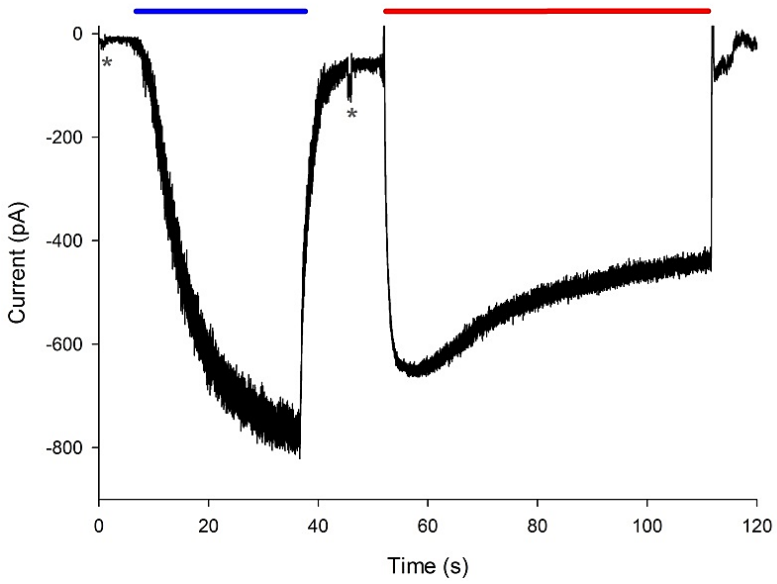

Fig. 3.6. Kinetics of OS membrane permeabilization induced by 1 µM [L-Glu(OMe)^{7,18,19}] in the presence of Na^+ and Ca^{2+}. Bars indicate timing of peptide application and withdrawal. Peptides were dissolved in two different solution (see Methods): (blue bar) 128 mM NaCl, 1.1 mM $CaCl_2$, 10 mM Hepes, pH 7.6; (red bar) 76.6 mM $CaCl_2$, 15 mM NaCl, 10 mM Hepes, pH 7.6. The asterisks indicate the -10 mV steps to measure R_m , R_a, and C_m at the steady state, before and after peptide removal. Kinetic parameters for the two transmembrane inward currents were reported in table 3.2.

1 µM [L-Glu(OMe)^{7,18,19}]	D_a (s)	τ_a (s)	I_{max} (pA)	D_d (s)	τ_d (s)
High external [Ca^{2+}]	1,00 ± 0,03	0,4 ± 0,02	450 ± 30	1,7± 0,2	1,00 ± 0,02
Low external [Ca^{2+}]	1,60 ± 0,02	3,80 ± 0,04	750 ± 15	2,5± 0,2	1,90 ± 0,01

Table 3.2. Kinetics parameters of current elicited by 1 µM [L-Glu(OMe)^{7,18,19}]. High external [Ca^{2+}] is referred to the solution (see Methods): 76.6 mM $CaCl_2$, 15 mM NaCl, 10 mM Hepes, pH 7.6; low external [Ca^{2+}] is referred to: 128 mM NaCl, 1.1 mM $CaCl_2$, 10 mM Hepes, pH 7.6. I_{max} was measured at the steady state i.e. ~35 sec following the peptide application n=3

The activation time constant (τ_a) of the current recorded through [L-Glu(OMe)^{7,18,19}] pores, was accelerated of ~10-fold if external Na^+ or K^+ was substituted with an equiosmolar concentration of Ca^{2+} (Table 3.2). Moreover, in the presence of high external Ca^{2+} concentration, current rapidly reached a peak amplitude and then decayed, at difference with Na^+, to a steady state level during continuous peptide application, possibly due to a progressive reduction of the number of peptidic pores, after an initial larger number. This hypothesized lower stability of the pores in high Ca^{2+} is also suggested by the faster decay to 0 of the current, upon peptide removal from the external solution, in respect to high Na^+: D_d and τ_d were indeed ~2-fold smaller than in high Na^+ (Table 3.2).

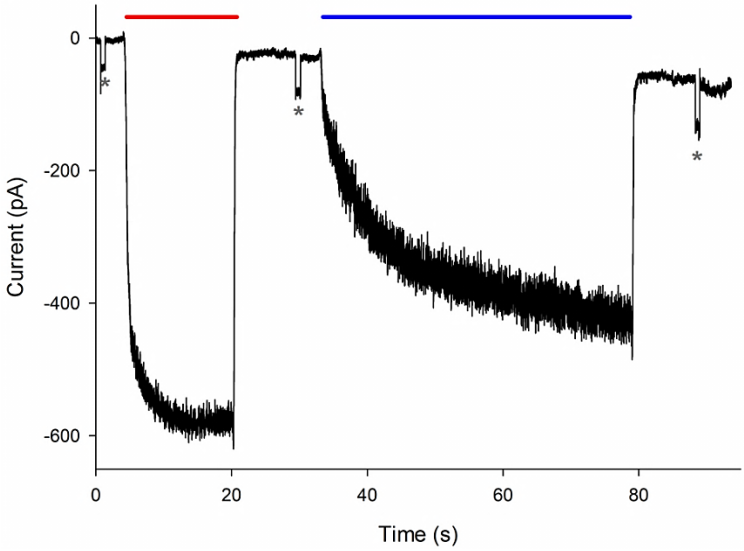

Fig. 3.7. Ca^{2+}-dependence kinetics of OS membrane permeabilization induced by 1 µM [L-Glu(OMe)^{7,18,19}]. Bars indicate timing of peptide application and withdrawal. Peptides were dissolved in two different solution: 57 mM NaCl, 1.1 mM $CaCl_2$, 50 mM choline chloride,10 mM Hepes, pH 7.6 (blue bar); 15 mM $CaCl_2$, 57 mM NaCl, 50 mM choline chloride, 10 mM Hepes, pH 7.6 (red bar). The asterisks indicate the -10 mV steps to measure R_m , R_a, and C_m at the steady state, before and after peptide removal. Kinetics parameters of the two current waveforms were reported in table 3.2.

1 µM [L-Glu(OMe)^{7,18,19}]	D_a (s)	τ_a (s)	I_{max} (pA)	D_d (s)	τ_d (s)
High external [Ca^{2+}]	**1,80 ± 0,02**	**1,00 ± 0,02**	**-584 ± 20**	**1,7± 0,3**	**1,00 ± 0,02**
Low external [Ca^{2+}]	**2,00 ± 0,01**	**9,10 ± 0,02**	**-400 ± 16**	**2,2± 0,2**	**1,90 ± 0,01**

Table 3.2. Ca^{2+}-dependence of the kinetics parameters of current elicited by 1 µM [L-Glu(OMe)^{7,18,19}].High external [Ca^{2+}] is referred to 15 mM $CaCl_2$, 57 mM NaCl, 50 mM choline chloride, 10 mM Hepes, pH 7.6; low external [Ca^{2+}] is referred to 57 mM NaCl, 1.1 mM $CaCl_2$, 50 mM choline chloride,10 mM Hepes, pH 7.6. n=3

Moreover, the smaller noise of the steady-state current in high external Ca^{2+} concentration in respect to high external Na^+ concentration, suggests that in high Ca^{2+} the average ratio of the single channel conductance and the number of channel open is larger than in high Na^+ (Fig. 3.6 and Fig. 3.7).

In order to evaluate the sensitivity to Ca^{2+} the phenomenology so far observed, different "high Ca^{2+} solutions" were used: at Ca^{2+}concentrations as low as 15 mM, τ_a and τ_d of the current waveform elicited by 1 µM of [L-Glu(OMe)^{7,18,19}], were already ~10-fold and ~2-fold, respectively, larger than those observed at low Ca^{2+} concentration (Fig. 3.7 and Table 3.2). However, at difference with 76 mM Ca^{2+}, the decay to a steady state level during continuous peptide application in 15 mM Ca^{2+} was not observed; moreover, the average value of I_{max} in 15 mM Ca^{2+} was larger than I_{max} in "low Ca^{2+}" concentration.

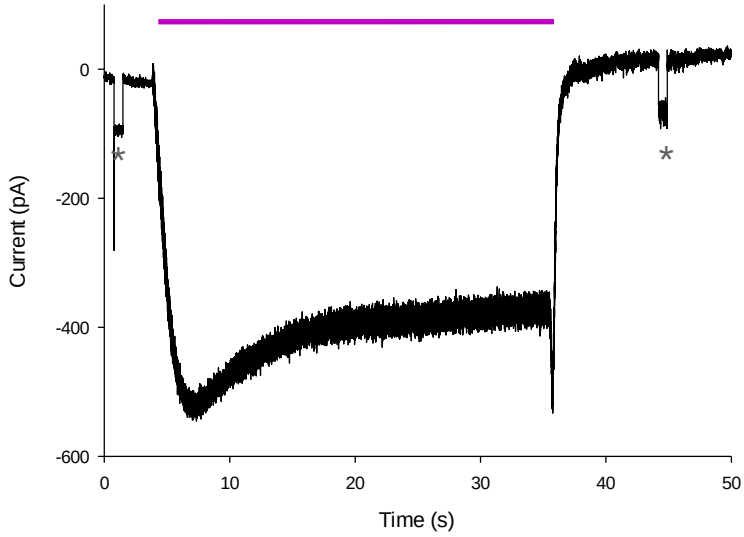

Fig. 3.8. Kinetics of OS membrane permeabilization induced by 1 µM [L-Glu(OMe)^{7,18,19}] dissolved in 76.6 mM $MgCl_2$, 15 mM NaCl, 10 mM Hepes, pH 7.6. Purple bar indicates timing of peptide application and withdrawal. The asterisks indicate the -10 mV steps to measure R_m , R_a, and C_m at the steady state, before and after peptide removal.

The waveform of current elicited by peptide application in "high Mg^{2+}" solution were similar to the one recorded in "high Ca^{2+}": however in 76.6 mM Mg^{2+}, τ_a (1.0 ± 0.2; n=3) resulted slower in respect to Ca^{2+}.

3.1.4 Membrane binding of [L-Glu(OMe)^{7,18,19}]-monitored by SPR

In order to understand the divalent-cation dependency of [L-Glu(OMe)^{7,18,19}] binding to the lipid bilayer at the molecular level, the electrophysiological experiments were paralleled with experiments employing the surface plasmon resonance (SPR) spectroscopy. For this purpose, lipid vesicles with a lipid composition corresponding to the vertebrate ROS membrane were immobilized on the surface of the L1 sensor chip (see Methods), and the dynamics of [L-Glu(OMe)^{7,18,19}] binding to this phospholipid surface was monitored, by using the same Ca^{2+} and Mg^{2+} concentrations of the electrophysiological experiments.

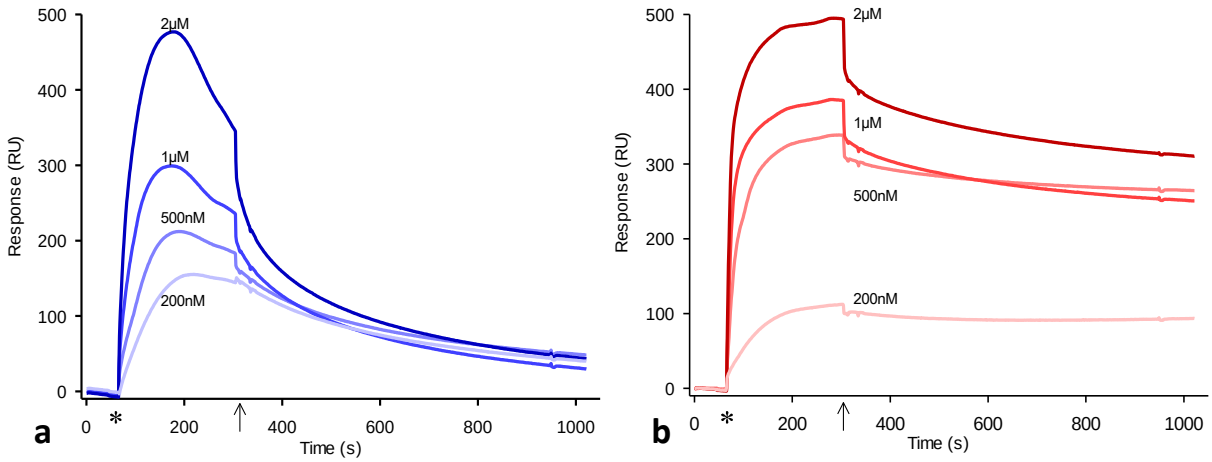

Fig. 3.9. SPR sensorgrams of [L-Glu(OMe)^{7,18,19}] binding to a lipid mixture (mimicking the OS membrane composition) immobilized on the sensor chip surface. ***a***, in the absence of $CaCl_2$; ***b*** in the presence of 76 mM $CaCl_2$. Four different peptide concentrations between 200 nM and 2 μM are shown. The asterisks indicate the start of antibody injection, followed by the association phase; the arrows indicate the injection end, followed by the dissociation phase. The running buffers were: ***a*** 130 mM NaCl, 10 mM Hepes, pH 7.6; ***b*** 76 mM $CaCl_2$, 10 mM NaCl, 10 mM Hepes, pH 7.6.

Different concentrations of [L-Glu(OMe)^{7,18,19}] (0.2, 0.5, 1, and 2 μM, dissolved in the running buffer), were injected on the immobilized phospholipid, at a flow rate of 5 μl/min for 4 minutes (Fig. 3.9). The binding kinetics measured in the absence of Ca^{2+} (Fig. 3.9*a*) was clearly different than the one measured in high Ca^{2+} (Fig. 3.9*b*). The sensorgram waveform in the former case increased up to a maximal amplitude, but after ~200 s (after injection started) it decreased in a concentration-dependent manner, indicating that at this point the dissociation

rate prevailed on the association rate, even if peptide is still injected. This instability of peptide binding is reinforced by the easiness with which the peptide was washed away the phospholipid surface (by applying solely the buffer at a flow rate of 5 µl/min) during the dissociation phase, that was monitored for 10 minutes following the end of peptide injection. If [L-Glu(OMe)^{7,18,19}], dissolved in high Ca^{2+} running buffer, was applied to the membrane surface, the binding kinetics was faster than the one recorded in low Ca^{2+} at all the peptide concentration tested. Moreover, the sensorgram waveform during the peptide injection increased up to a plateau, that was not followed by any decay, suggesting an higher stability of the peptide binding to the lipids in respect to low Ca^{2+} (Fig. 3.9*b*). This stability of peptide binding is reinforced by the extremely slow and incomplete dissociation phase during the peptide wash-out. However, the difficulty to estimate the precise amount of lipids absorbed on the chip surface do not allow quantitative analyses of these kinetics, but it can be anyway concluded from the qualitative analysis of this data, that Ca^{2+} increases the peptide affinity to the phospholipids surface.

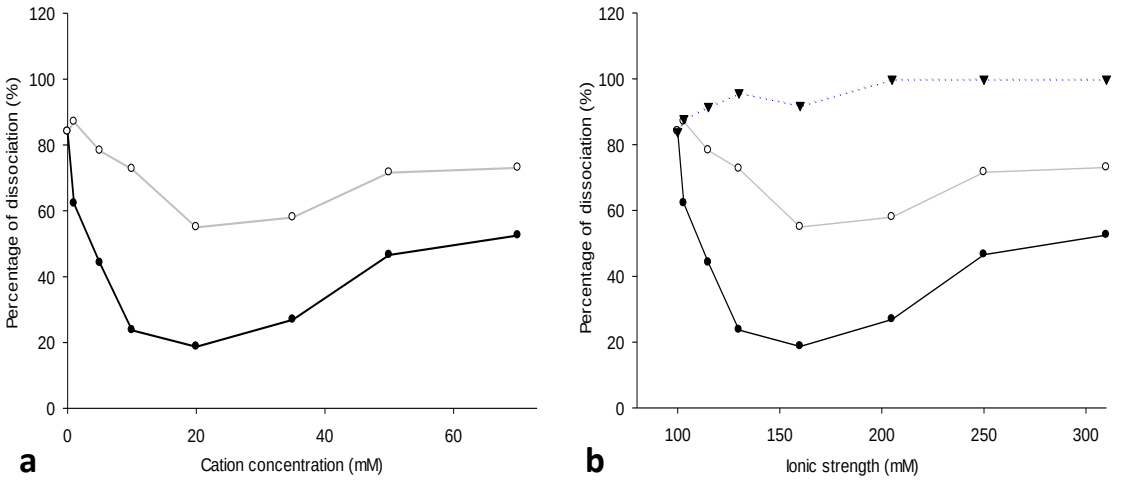

Fig. 3.10. Binding strength between [L-Glu(OMe)^{7,18,19}] and lipids in various ionic conditions. Percentage of dissociation of [L-Glu(OMe)^{7,18,19}] from the lipids ten minutes after ceasing the peptide injection (flow rate of 5 µl/min for 4 minutes; peptide concentration: 1µM) in function of divalent cation concentration ***a*** and ionic strength ***b***; black line, $CaCl_2$; gray line, $MgCl_2$; dotted gray line, NaCl. 100 mM NaCl were always present in all the experiments reported in ***a*** and ***b***.

To further investigate the Ca^{2+}-dependent increase of the binding strength between the peptide and the lipid phase, titrations with increasing Ca^{2+} concentrations (1 mM - 60 mM) were performed (Fig. 3.10*a*). The percentage of dissociation ten minutes after ceasing the 1 µM [L-Glu(OMe)^{7,18,19}] injection were plotted against the $CaCl_2$ concentrations (added to 100 mM NaCl, 10 mM Hepes, pH 7.6 running buffer) The results in Figure 3.10*a* show that 1 mM Ca^{2+} in the running buffer sufficed to increase significantly the number of peptide molecules

bounded to the phospholipid surface: this number kept increasing upon increasing Ca^{2+} concentration, peaked at about 20 mM (i.e. the percentage of dissociation had its smallest value), and declined at higher Ca^{2+} concentration. A similar trend was also observed when the titrations were performed with the same concentrations of Mg^{2+} in the running buffer, but the amount of peptide bound after the dissociation phase was significantly lower than that observed in the presence of Ca^{2+} at the same concentrations (Fig. 3.10*a*, 3.11*a*). Interestingly, 20 mM of Mg^{2+} appeared again to be an optimal concentration for divalent cations in order to maximize the peptide binding to the membrane (Fig. 3.10*a*). Many studies suggest that the increase in ionic strength reduces the activity of antimicrobial peptides, weakening the electrostatic interactions needed for the initial interaction with the membrane phospholipids (Wu et al., 2008; Zasloff et al., 2002). To discriminate between the effect of the ionic strength of the solutions used in Fig. 3.10*a*, and a direct effect of the divalent ions on the peptide-lipid binding, the latter was studied by using solutions with no divalent ions, but of increasing ionic strength that was achieved by using only Na^{+}. However, the increase of ionic strength obtained by changing Na^{+} concentration (Fig. 3.10*b*, dotted gray line) resulted in the complete dissociation of [L-Glu(OMe)^{7,18,19}] ten minutes after the end of injection. In contrast, the higher affinity of the peptide to the phospholipids in the presence of Ca^{2+} or Mg^{2+} in the high ionic strength solutions, indicates that ionic strength per se is not a modulator of the peptide-membrane affinity, but Ca^{2+} and Mg^{2+} promote specifically the [L-Glu(OMe)^{7,18,19}] binding to phospholipids surface.

3.1.5 Ca^{2+}-sensitivity of Trichogin GA IV and [L-Glu(OMe)^{7,18,19}] binding to membrane

As a further control, it was studied the divalent ion dependency of the binding of another antimicrobial peptaibiotic, trichogin GA IV, on the immobilized lipid surface (Fig. 3.11*b*) under the same experimental conditions used above for [L-Glu(OMe)^{7,18,19}]. In the absence of divalent cations, *trichogin* GA IV (1 µM) application to the membrane elicited a sensorgram (Fig. 3.11*b*, blue line) similar to the one elicited by [L-Glu(OMe)^{7,18,19}] (Fig. 3.11*a*, blue lines). However, no significant differences in the binding responses of 1µM trichogin GA IV were observed in the absence of Ca^{2+} or in the presence of 20 mM Ca^{2+} or Mg^{2+} (Fig 3.11*b*): this demonstrates that divalent cations specifically increase the membrane-peptide affinity of [L-Glu(OMe)^{7,18,19}].

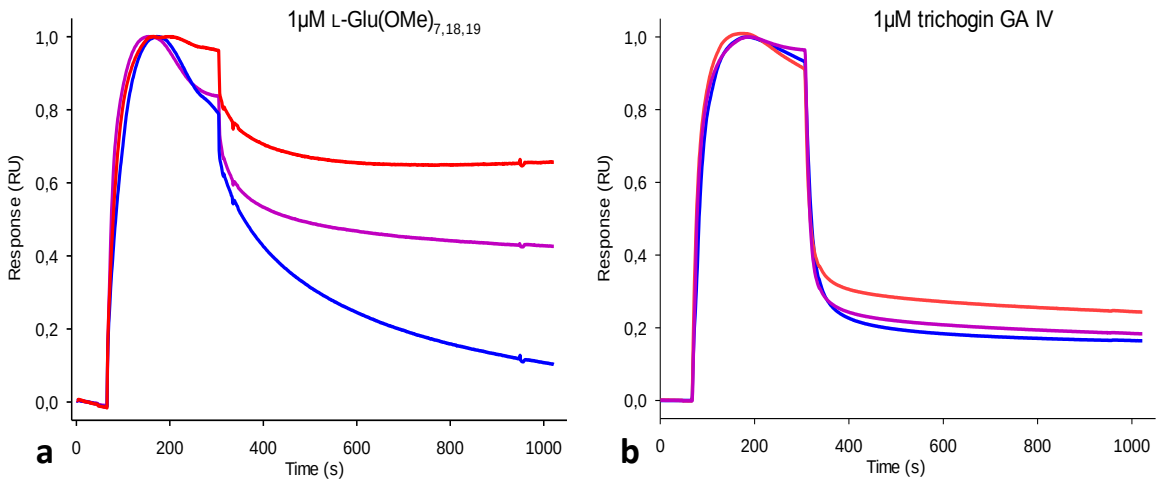

Fig. 3.11. Comparison between the divalent cation sensitivity of the binding properties of [L-Glu(OMe)^{7,18,19}] and *trichogin* GA IV applied at 1 µM concentration. ***a*** Normalized sensorgrams of [L-Glu(OMe)^{7,18,19}] binding to immobilized liposomes mixture on the surface of the sensor chip, in the absence of divalent cations (blue line; running buffer composition: 100 mM NaCl, 10 mM Hepes, pH 7.6), in the presence of 20 mM $MgCl_2$ (added to the above buffer; purple line) and in the presence of 20 mM $CaCl_2$ (red line). ***b*** Normalized sensorgrams of 1µM *trichogin* GA IV binding to the same immobilized liposomes mixture on the surface of the sensor chip. Same sensorgram color code and solutions as in ***a***.

3.1.6 Ca^{2+} -dependent modulation of antimicrobial peptide activity

The interaction of pore-forming peptides to biological membranes is a multi-step process in which a first initial electrostatic peptide-membrane interaction is followed by the peptide insertion into the phospholipid bilayer, and finally pore formation occurs. The rapidity (milliseconds) with which these processes succeed one another, makes it difficult to study each step separately. In this work, the merge between the analysis of the peptide-induced current and the relative peptide-membrane interaction measured by SPR, has proved very innovative method to discriminate these events. Surface plasmon resonance-based results showed that high Ca^{2+} or Mg^{2+}concentration promotes a larger number of [L-Glu(OMe)^{7,18,19}] monomers to bind to the lipid surface, resulting in the increase of the pore formation probability, as it was shown by the small τ_a value of the current activated by [L-Glu(OMe)^{7,18,19}] application. Moreover, the increase in the peptide-membrane affinity in the presence of Ca^{2+} and Mg^{2+} (Fig. 3.11) is a peculiarity of [L-Glu(OMe)^{7,18,19}], in fact these divalent ions did not significantly affect the trichogin GA IV bind to the membrane. This also excludes that the observed Ca^{2+} (or Mg^{2}) modulatory effect of peptide binding to the lipids can be entirely due to an interaction between divalent cations and phospholipids, i.e. independently by the presence of the peptide. It is indeed well known that the cell membrane spontaneously reseal a damage, because a closed bilayer is the most stable form of lipids in water. This self-sealing property is enhanced by

divalent cations such as Mg^{2+} and Ca^{2+}, which form ionic bonds with phospholipid phosphate groups, leading to lipid binding and decreased fluidity, playing an important role in stabilizing biological membranes (Carratu et al., 1996). Moreover Zhau (Zhou et al., 2008) showed that membrane pores induced by cell membrane sonication, were resealed in a Ca^{2+} concentration-dependent manner. On the basis of these papers, it is possible to simply explain all the results presented above by hypothesizing that Ca^{2+} plays a dual role in the pore-formation dynamics, as follows. Once the peptide is applied to the membrane, the presence of even small amount of Ca^{2+} rapidly increases the rate of peptide-membrane binding, but this is in competition with the capability of Ca^{2+} to form ionic bonds with phospholipid phosphate groups, which progressively increases membrane rigidity, and therefore slowly hinders the pore formation. The former mechanism reduces therefore τ_a when the peptide is applied in the presence of Ca^{2+}, while the latter produces the progressive decay of the current amplitude to a steady state level during continuous peptide application. It is conceivable that, to hinder the continuous pore formation (promoted by Ca^{2+} itself) through the Ca^{2+} dependent increase of the membrane rigidity, high Ca^{2+} concentrations may be required: indeed, no current decay was observed during peptide application in 15 mM Ca^{2+} (but the τ_a decrease was still well evident: Fig. 3.7 and Table 3.2). This is in full agreement with the SPR data, that indicate a range of Ca^{2+} concentration between 10 and 20 mM for optimal membrane-[L-Glu(OMe)^{7,18,19}] binding (Fig. 3.10a). Moreover, the smaller current fluctuation amplitude observed in high Ca^{2+} in respect to low Ca^{2+}, agrees again with the action of Ca^{2+} in promoting pore formation: since a conductive channel must be formed by several peptide monomers (Crisma et al., 2007) the presence of Ca^{2+} increases the probability of formation of smaller and more stable pores, rather than larger and more unstable ones. Finally, both SPR and electrophysiology experiments showed that Mg^{2+}promotes [L-Glu(OMe)^{7,18,19}]-membrane interaction and pore formation, but the effect was less stronger if compared with Ca^{2+}.

3.2 Modulation of zebrafish cone phototransduction by intracellular delivery of zGCAP3 and of its antibody via patch-clamp pipette

The physiological role of zGCAP3 in phototransduction was investigated in zebrafish cones by time-controlled delivery of either exogenous GCAP3 or its specific monoclonal antibody in the cytosol. The delivery was performed via the patch pipette by a quartz capillary (or a Teflon tube) inserted in its lumen. The perfusion solution containing the macromolecules under study was drained out of the quartz capillary, positioned as close as possible to the pipette tip, by the controlled application of pressure, thus leading to the delivery of macromolecules into the cytosol. However, the long tapered shape of conventional pipette shanks, makes it very difficult to perfuse efficiently the cell with this strategy. A significant improvement of an existing method to wide the patch pipette shank illustrated in the Methods section, based on the calibrated combination of heat and air pressure (pressure polishing, see Methods), allowed to insert quartz or plastic tubes in the pipette lumen very close to its tip.

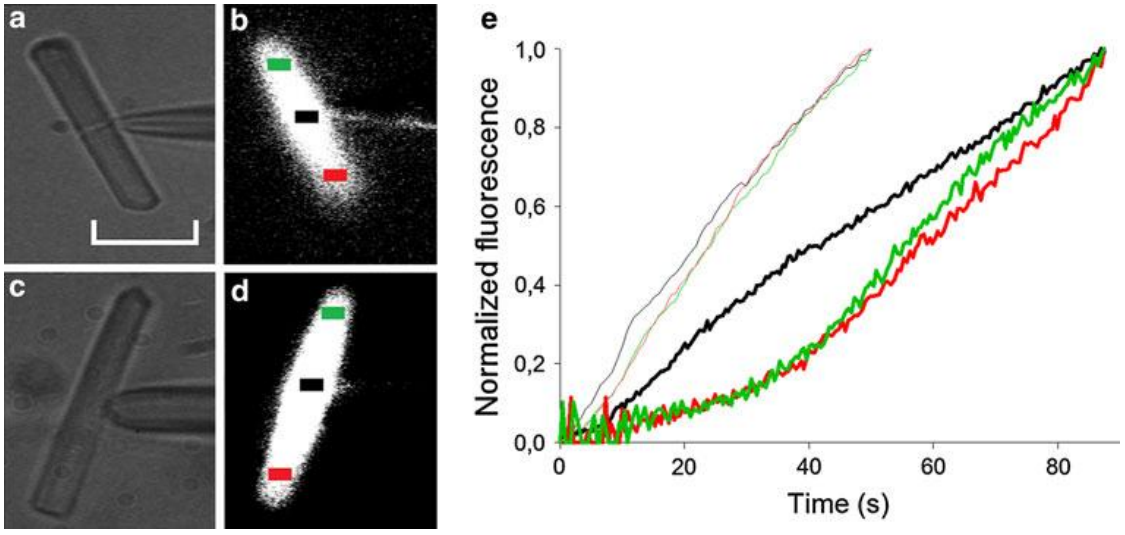

Fig.3.12. Kinetics of *lucifer yellow* diffusion into a frog OS recorded in whole-cell for two different pipette geometries. ***a*** and ***c***, bright-field images of a whole-cell configuration recording with a conventional fire polished pipette (shown in ***b*** in fluorescence; access resistance ~24 MΩ) and a pressure polished pipette (shown in ***d*** in fluorescence; access resistance ~7 MΩ), respectively; scale bar = 20 μm. ***e***, normalized fluorescence intensity integrated in the *black*, *green*, and *red* regions vs time for the fluorescence imaging recording in ***b*** (*thick* traces) and ***d*** (*thin* traces). In numbers: the normalized fluorescence, integrated in the *black* region, reached about 50% of the maximal one at 40.9 s in ***b*** (data from *e*, *black thick* trace) and at 21.8 s in *d* (***e***, *black thin trace*); the integrated fluorescence in *green* and *red* regions was 0.24 and 0.23, respectively, at 40.9 s in ***b*** (*e*, *green* and *red thick* traces) and 0.45 in both regions at 21.8 s in ***d*** (*e*, *green* and *red thin* traces).

Pressure polished pipettes increased the rate of molecular diffusion between the pipette and the cell interior, as shown by the time course of fluorescence dye loading of the frog rod outer segment (OS) cytosol via the patch pipette. In such experiment (Fig. 3.12), the rate of the

fluorescence increase with time (Fig. 3.12*e*) detected in three OS cytoplasmic rectangular regions of the same area at the level of the patch pipette and at the two OS ends (Fig. 3.12*b* and *d*), was plotted against time and shown for two typical experiments. One experiment (Fig. 3.12*a*, *b*, and *e*, *thick traces*) was carried out with a conventional patch pipette (Fig. 3.12*a*), the other one (Fig. 3.12*c*, *d* and *e*, *thin traces*) with a pressure polished pipette with a geometry in between the ones illustrated in Fig. 2.5*c* and *e*. The rate of *lucifer yellow* (see Methods) concentration increase in the cytosol obtained with the pressure polished pipettes (Fig. 3.12*e*, *thin traces*) was about 2-fold (1.8 ± 0.4, n=4) faster with respect to conventional pipettes (Fig. 3.12*e*, *thick traces*). This larger concentration rise at the level of the patch pipette (*black traces*), produced also a faster longitudinal diffusion toward the two OS ends (although the presence of the disk stack should hinder this diffusion) with respect to conventional pipettes, as indicated by the shorter delay between the rate of fluorescence increase at these two OS ends (*red and green traces*) compared to the one at the level of the patch pipette (*black trace*).

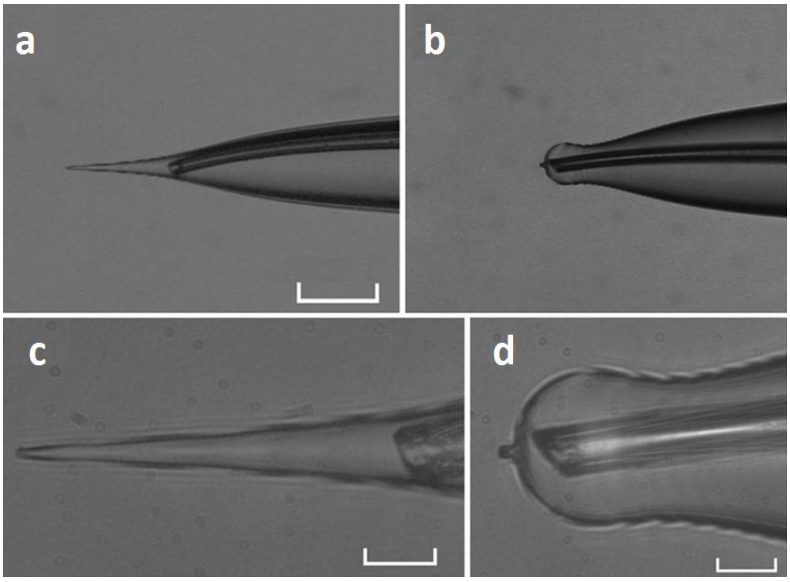

Fig. 3.13. Controlled intracellular perfusion. ***a*** A pulled quartz tube is positioned inside the lumen of a conventional pipette as close as possible to its tip, magnified in ***c***; ***b*** the same tube is inserted in a pressure-polished pipette, magnified in ***d***. Scale bar 100 µm in ***a*** and ***b***, and 20 µm in ***c*** and ***d***.

The substantial improvement in the cell dialysis given by the pressure-polished pipettes, allows to perfuse small proteins and peptides in the cytosol, making it possible to perform a "real time modulation" of a multitude of cellular processes, like signal transduction cascades. Indeed, the enlarged pipette shank (Fig. 3.13*b* and *d*), allowed a significantly small quartz perfusion tube (~10 µm of internal diameter and ~18 µm of external one) to be placed approximately 95 µm closer to the pipette tip with respect to a conventional pipette shank (Fig. 3.13*a* and *c*), hence reducing the perfusion delay for a small protein (having a diffusion

coefficient $D=10^{-6}$ cm^2 sec^{-1}) of about 15 s, according to the three-dimensional diffusion equation in the absence of pressure:

$$t = \frac{x^2}{6 \cdot D}$$

However, pulled quartz tubes with such a small diameter were extremely fragile and difficult to handle. More robust tubes, having an external diameter up to ~45 µm, were positioned inside an enlarged shank pipette as close to the pipette tip as the above one (Fig. 3.13*d*), but they had to be positioned at least as far as 200 µm from the pipette tip in the case of conventional pipettes, resulting in a perfusion delay of more than 70 s.

3.2.2 Zebrafish cones dialysis with ZGCAP3

The incorporation of zGCAP3 into the zebrafish cone cytosol was verified by the intracellular fluorescence, following the application of an intracellular solution containing 10 µM of dansyl chloride-labeled zGCAP3 (with low degree of dansylation: 16-22%), once the *whole-cell* recording was gained. This fluorescence build-up was observed about ~10 s after the application of the pressure into the perfusion tube placed inside the pipette.

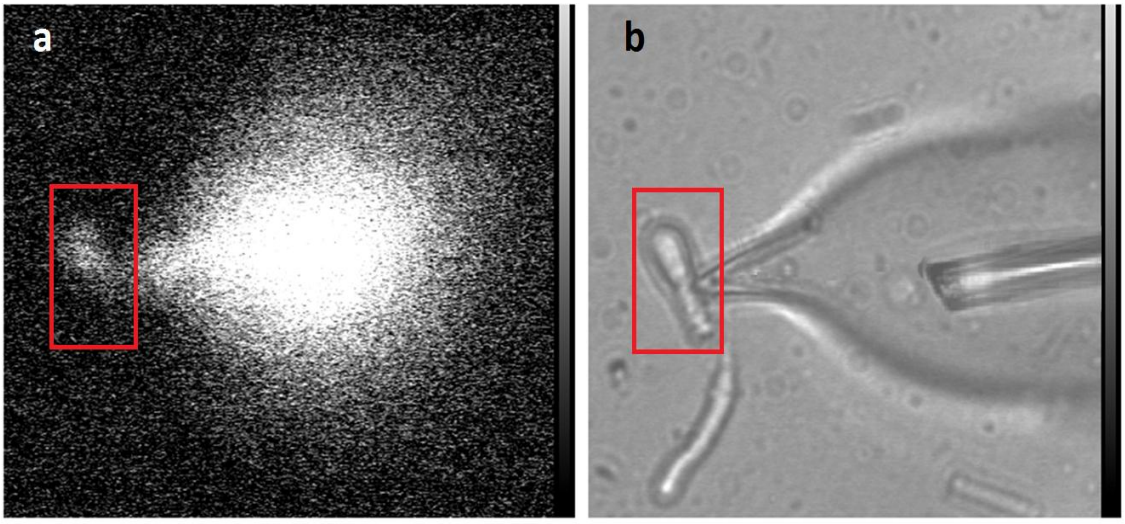

Fig. 3.14. Fluorescence diffusion of dansyl chloride-labeled zGCAP3 in a zebrafish cone (shown by the red square). ***b*** bright field image of ***a*** where it is visible the perfusion Teflon tube inserted in the pipette lumen.

3.2.3 Determination of IgG1 monoclonal antibodies- zGCAP3 affinity by SPR

In order to obtain specific silencing of the zGCAP3s with the intracellular delivery of antibodies in zebrafish cones, surface plasmon resonance (SPR) (see Methods) experiments were performed to allow the selection of a monoclonal antibody with strong affinity for zGCAP3 and low cross activity with other components of the phototransduction cascade. Several methods, employing surface plasmon resonance, were devised for screening antibodies from their crude hybridoma samples (Canziani et al., 2004, Safsten et al., 2006). Therefore, using similar capture technique, four different IgG1 monoclonal antibodies (clones: 7E6, 6G9, 6B9 and 4C12; see Methods) were screened against zGCAP3 and zGCAP4 in order to select the antibody with highest affinity for zGCAP3 and less cross activity for zGCAP4. The specific concentration for each antibody present in the hybridoma fluid was not exactly quantified and this represents a limitation in the association rate constant determination of each antibody-antigen interactions. zGCAP3 was covalently attached to the dextran matrix of the sensor chip (CM5, see Methods) surface by amine-coupling (see Methods), reaching an immobilization level of ~2000 resonance units (RU), corresponding to approximately 2 ng/mm^2. Unpurified IgG1 monoclonal antibodies were dissolved 1:2 in running buffer (150 mM NaCl, 10 mM Hepes, 3 mM EDTA, pH 7.4) and injected over zGCAP3 at a flow rate of 10 µl/min for 4 minute, by monitoring the dissociation phase for 15 min (Fig. 3.15) The sensor chip surface was regenerated with a pulse of 5 µl of 0.05% (v/v) sodium dodecyl sulfate (SDS) at a flow rate of 10 µl/min, after each antibody injection.

Despite it was not possible to resolve the binding kinetics for each IgG1, IgG1 7E6 was selected because of its lowest percentage of dissociation from zGCAP3, as assessed 15 min after the end of the association phase (Fig. 3.15, Table). However, all IgG1s showed cross-reactivity toward zGCAP4, which was immobilized (~2700 RU) on the chip surface by following the same protocol used for zGCAP3 (Fig. 3.15b). Therefore, the reduction of this non-specific binding and the determination of the antibody concentration were crucial to pursue the project goal. These problems were overcome using antibodies purification protocols as illustrated in further experiments described below.

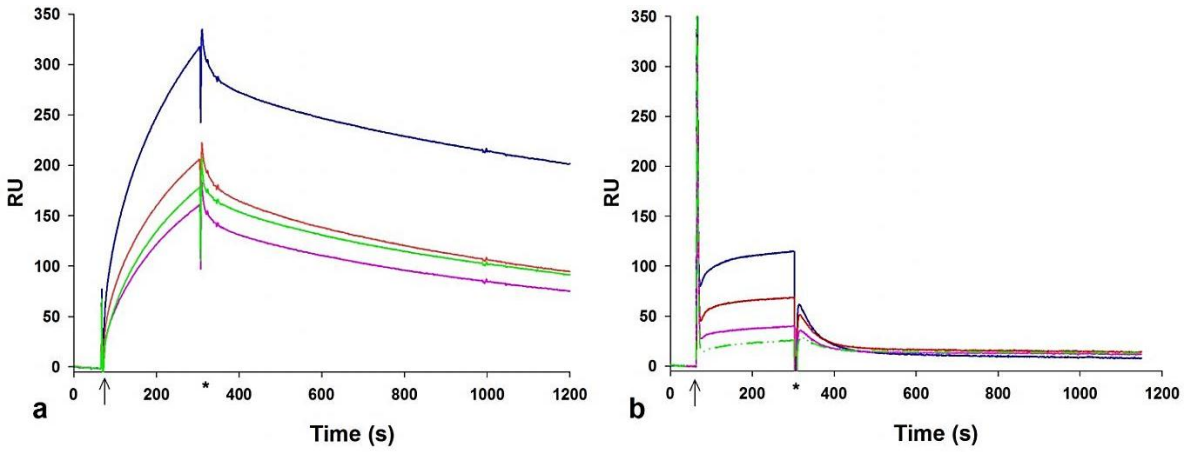

	IgG1 7E6	IgG1 6G9	IgG1 6B9	IgG1 4C12
Percentage of diss. (%)	~36 %	~53%	~ 48%	~53%

Fig. 3.15. Antibody affinities to zGCAP3 and zGCAP4. SPR sensorgrams of IgG1 7E6 (blue line), 6G9 (red line), 6B9 (green line), and 4C12 (magenta line) binding to ~2000 RU of zGCAP3 (***a)*** and ~2700 RU of zGCAP4 ***(b)***, immobilized onto the CM5 sensor chip. All IgGs were diluted in running buffer (150 mM NaCl, 10 mM Hepes, 3 mM EDTA, pH~7) and injected at a flow rate of 10 µl/min for 4 minute. The arrows indicate the start of antibody injection, followed by the association phase; the asterisks indicate the injection end, followed by the dissociation phase. In the table is reported, for each antibodies, the percentage of resonance units (RU) lost (percentage of dissociation) 15 min after the end of the association phase with zGCAP3 immobilized.

3.2.4 Binding properties of purified IgG1 7E6

Since the serum contain, besides the IgG1 7E6, many other proteinaceous components, IgG1 7E6 was purified from rabbit serum to assess whether bindings to zGCAP4 described in Fig. 3.15 was specific or not. Therefore, the non-denaturing protocol of anion-exchange chromatography (AEC) was run and the purity of the collected fractions was checked by SDS-page electrophoresis (Fig. 3.16a, see Methods). The purest samples were collected together, then they were dialyzed against the phosphate buffer (see Methods) in order to remove the high salt buffer used in ion exchange chromatography, and finally lyophilized. In order to measure the binding kinetics of purified IgG17E6, different concentrations of this antibody (0.13 µM; 0.22 µM; 0.33 µM; 0.67 µM; 1.34 µM in HBS buffer) were injected over zGCAP3 protein (immobilized on the CM5 sensor chip) at 10 µl/min for 4 minutes (Fig. 3.16b). The resulting k_{on} and k_{off} were similar to the ones measured when IgG1 7E6 (applied at the same concentrations) was run by replacing the HBS buffer with the zebrafish intracellular cone solution (187 mM KCl, 2 mM $MgCl_2$, 5 mM HEPES, pH 7.6), in order to simulate the same conditions of the electrophysiological experiments (Fig. 3.16c). Notably, no cross activity of purified IgG1 7E6 against zGCAP4 was measured (Fig. 3.16d).

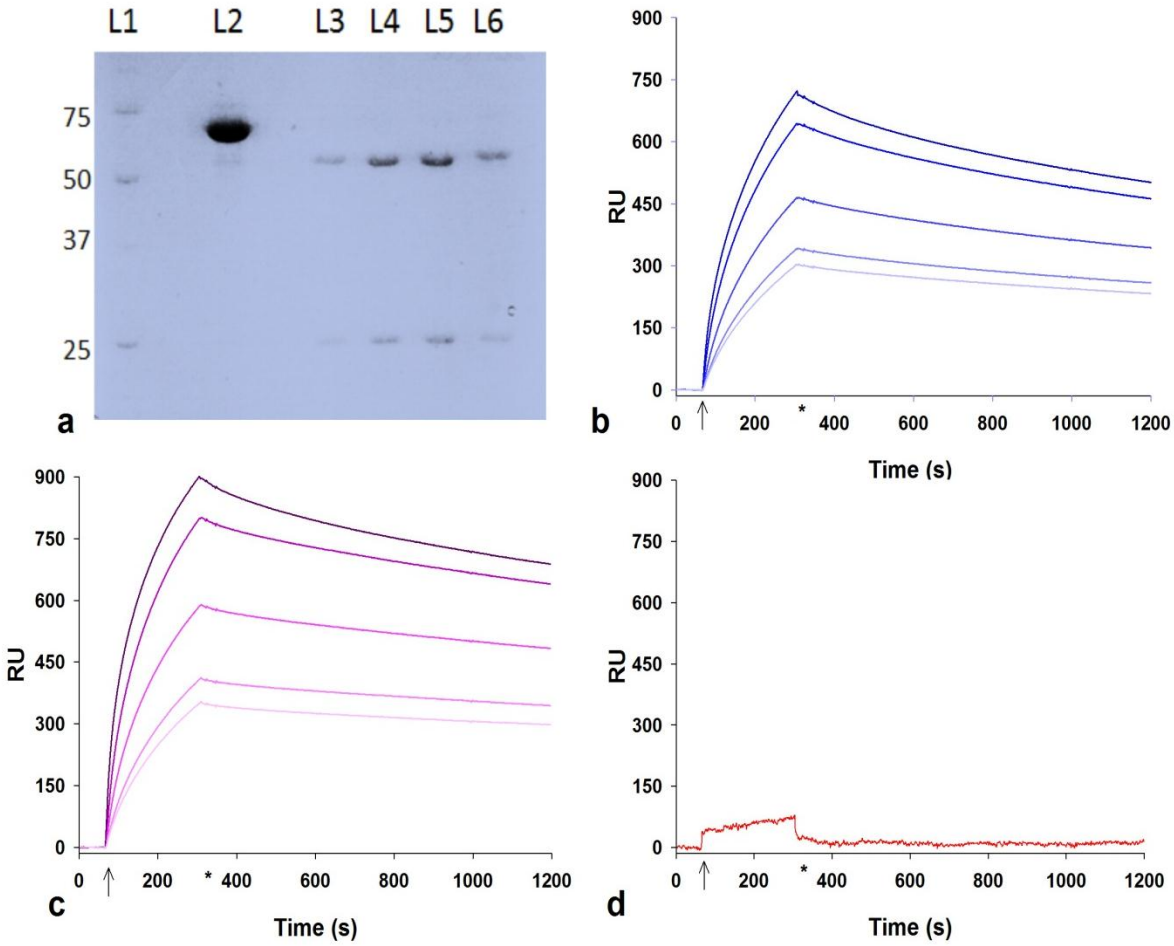

Fig. 3.16. **a** SDS-PAGE (10% polyacrylamide, reducing conditions, Coomassie-stained) of four IgG1 7E6 fractions collected from the peak of the anion exchange chromatogram. The two bands of lanes 3 to 6 show the IgG1 7E6 heavy chains (~50 kDa) and light chains (~25 kDa), while the unbound fraction collected at low salt concentration is showed in line 2; molecular weight markers are shown in lane 1. **b-c** SPR sensorgrams of IgG1 7E6 binding to zGCAP3 immobilized (~2000 RU) on the surface of the sensor chip in the presence of HBS (150 mM NaCl, 10 mM Hepes, 3 mM EDTA, pH 7.4; **b** and zebrafish intracellular cone solution (187 mM KCl, 2 mM $MgCl_2$, 5 mM HEPES pH 7.6; **c**. The arrows indicate the start of antibody injection, while the asterisks indicate the injection end. The binding curves were obtained by injecting five different concentrations of IgG1 7E6 (0.13 µM; 0.22 µM; 0.33 µM; 0.67 µM; 1.34 µM) at a flow rate of 10 µl/min for 4 min, monitoring the dissociation phase for 15 min. **d** Cross-reactivity of IgG1 7E6 (0.27 µM dissolved in HBS buffer) toward zGCAP4 immobilized (~4500 RU) on the chip surface

Analyte	k_{on} **(×10^{4}M^{-1}s^{-1})**	k_{off} **(×10^{-4}M^{-1}s^{-1})**	**K$_d$ (×10^{-8}M)**	**K$_a$ (×10^{-8}M^{-1})**
IgG1 7E6	2.4 ± 0.3	3.3 ± 0.3	1.4 ± 0.3	7.1 ± 0.3

Table 3.3. Association and dissociation rate constants of IgG1 7E6 monoclonal antibody for zGCAP3 measured by SPR. The affinity constant ($K_a = k_{on}/k_{off}$) and the equilibrium constant ($K_d = k_{off}/k_{on}$) were calculated from the average association (k_{on}) and dissociation (k_{off}) rate constants measured from local fits to n=34 sensorgrams, using 1:1 Langmuir binding model.

3.2.5 Comparison between global and local fitting to the sensorgrams

The best fitting values of the IgG1 7E6-zGCAP3 binding constants to the sensorgrams, were determined by both local and global fittings, i.e. by fitting the single curve (obtained at a fixed analyte concentration) and by simultaneously fitting the entire experimental curve set (obtained at several analyte concentrations), using a simple 1:1 Langmuir interaction model (Fig. 3.17). The equilibrium dissociation constant (K_d) was calculated from the ratios of the the association rate constant k_{on} and the dissociation rate constant k_{off} ($K_d = k_{off}/k_{on}$). The average values for 34 experiments are shown in Table in Fig. 3.17.

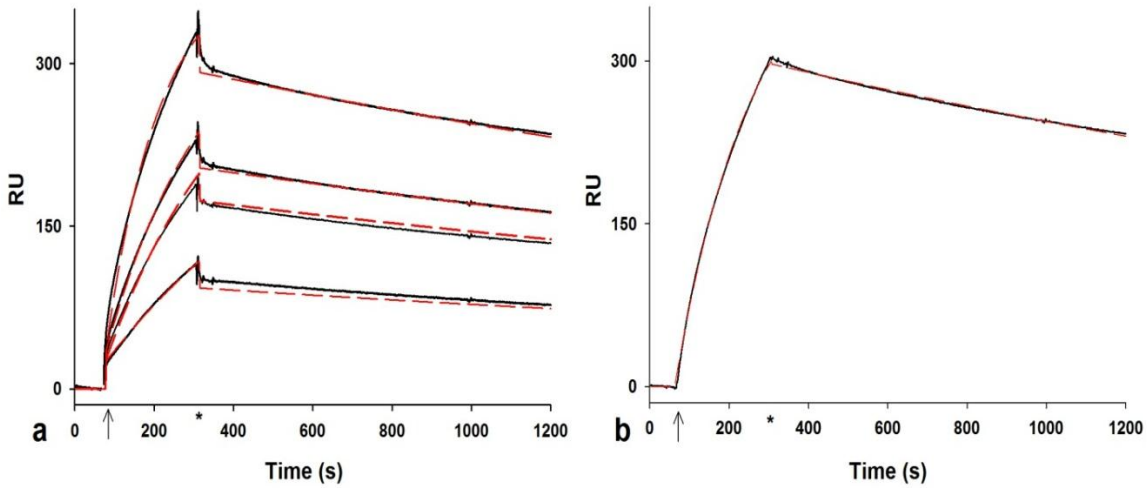

Analyte IgG1 7E6	k_{on} ($\times 10^4 M^{-1}s^{-1}$)	k_{off} ($\times 10^{-4} M^{-1}s^{-1}$)	K_d ($\times 10^{-8} M$)	K_a ($\times 10^{-8} M^{-1}$)
a) Global fitting	2.8± 0.3	3.6± 0.3	1.2± 0.3	7.7± 0.3
b) Local fitting	2.6± 0.3	3.1± 0.3	1.3± 0.3	8.4± 0.3

Fig. 3.17. ***a*** Global fitting of the binding curves obtained with different concentrations of IgG1 7E6-zGCAP3 (0.05 µM; 0.11 µM; 0.14 µM; 0.28 µM dissolved in HBS buffer) injected over a surface with ~2000 RU of immobilized zGCAP3. ***b*** Single fitting of the binding curve of 0.28 µM IgG17E6 (in HBS buffer) to immobilized zGCAP3 (~2000 RU). Antibodies were injected at flow rate of 10 µl/min for 4 minute and the dissociation phase was followed for 15 min. The arrows indicate the start of antibody injection, followed by the association phase; the asterisks indicate the injection end, followed by the dissociation phase. In the table, the affinity constant (K_a) and dissociation constant (K_d) were obtained from the ratio of the association (k_{on}) and dissociation (k_{off}) rate constants, using 1:1 Langmuir binding model; $K_a = k_{on}/k_{off}$; $K_d = k_{off}/k_{on}$. Local ***b*** and global fitting ***a*** of the sensorgrams are shown as red dash lines.

3.2.6 zGCAP3 dimerization test

Some authors suggested that GCAPs may play a key role in the GC activation process through dimerization (Olshevskaya et al., 1999). Dimeric forms of human GCAP3 were

observed in SDS-page and on immunoblotting assays (Imanishi et al., 2004). The monomer-dimer equilibrium of zebrafish GCAPs was investigated by size exclusion chromatography by Scholten and Koch (2011). In this thesis, by using physiological buffers, zGCAP3 dimerization was not observed as proven by the lack of any change in SPR signal upon injecting zGCAP3 over the same protein immobilized on the sensor chip (Fig. 3.18).

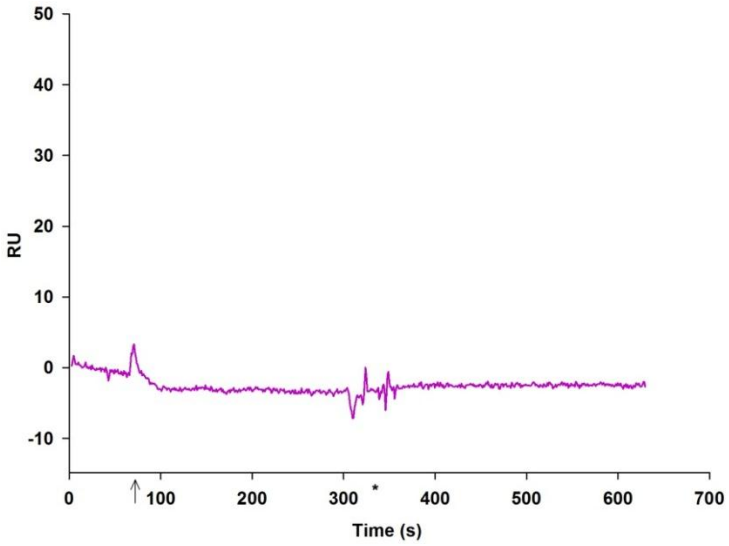

Fig. 3.18. SPR sensorgrams obtained injecting 1 µM zGCAP3 (dissolved in HBS: 150 mM NaCl, 10 mM Hepes, 3 mM EDTA, pH 7.4) over zGCAP3 immobilized (~2700 RU) at a flow rate of 10 µl/min for 4 minute. The arrow indicates the start of antibody injection, followed by the association phase; the asterisk indicates the injection end, followed by the dissociation phase.

3.2.7 Ca^{2+}-independence of the antibody interaction with zGCAP3

The dissociation of Ca^{2+} from zGCAP3 triggers GC activation through the rearrangement of two structural domains, each one containing a pair of EF-hand motifs. Before to test in a living cone the antibody effects, it is necessary to test first that IgG1 7E6 binding to zGCAP3 occurs independently by the zGCAP3 conformational state, which depends by the intracellular Ca^{2+} level during the cone photoresponse. The possible Ca^{2+}-dependence of IgG1 7E6 binding to zGCAP3 was checked by using SPR, upon injecting the same IgG17E6 titration over zGCAP3 in the absence or in the presence of Ca^{2+} in the running buffer (150 mM NaCl, 10 mM Hepes, 3 mM EDTA, pH 7.4). The result was clear cut: no Ca^{2+}-dependent binding was observed, even changing the Ca^{2+} concentration in a range well beyond the physiological one (Fig. 3.19).

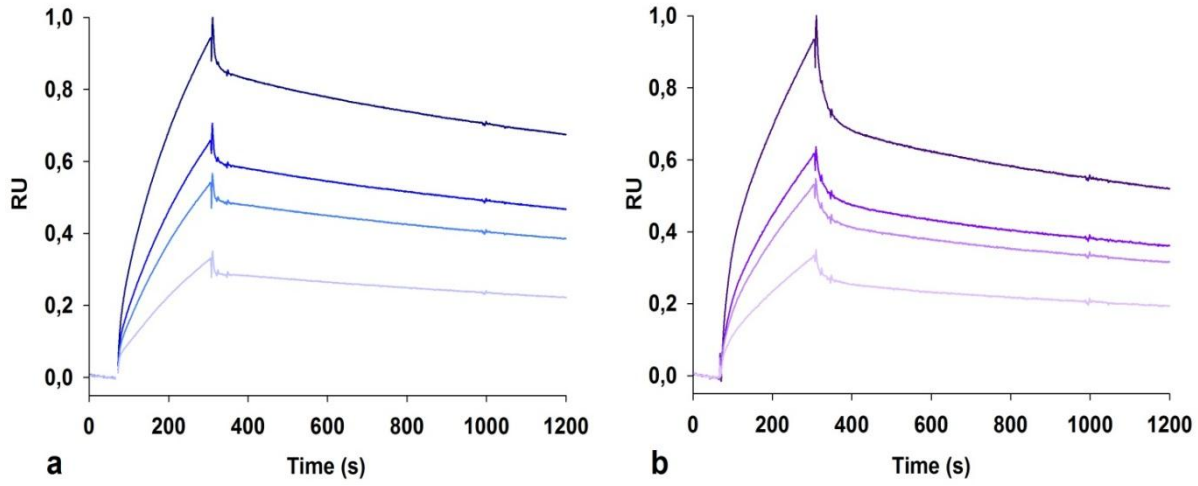

Analyte IgG1 7E6	k_{on} ($\times 10^{4} M^{-1}s^{-1}$)	k_{off} ($\times 10^{-4} M^{-1}s^{-1}$)	K_d ($\times 10^{-8} M$)	K_a ($\times 10^{-8} M^{-1}$)
a) No Ca^{2+}	2.8± 0.3	3.6 ± 0.3	0.8± 0.3	1.3± 0,3
b) 1mM Ca^{2+}	2.6± 0.3	2.6± 0.3	1± 0.3	1± 0.3

Fig. 3.19. Global fittings of the binding curves obtained with different concentrations (0.05 µM; 0.11 µM; 0.14 µM; 0.28 µM) of IgG1 7E6, dissolved in ***a*** HBS buffer without Ca^{2+} (150 mM NaCl, 10 mM Hepes, 3 mM EDTA, pH 7.4) and ***b*** HBS buffer with 1mM Ca^{2+} without EDTA IgG1 7E6 was injected over a surface with ~2000 RU of immobilized zGCAP3. The arrows indicate the start of injection and the association phase while the asterisks indicate the end of injection and the beginning of dissociation phase In the table, the affinity constant (K_a) and dissociation constant (K_d) were obtained from the ratio of the association (k_{on}) and dissociation (k_{off}) rate constants ($K_a = k_{on}/k_{off}$; $K_d = k_{off}/k_{on}$).

3.2.8 Mass transfer limitation in SPR experiments

Binding of analyte to the *ligand* on the sensor chip occurs in two-steps, with their own rate constants: first, the analyte is transferred (the mass transfer) out of the bulk solution on the sensor chip surface; second, the specific, high-affinity interaction between the analyte and the *ligand* takes place. The mass transfer depends on the chip size, the convection and diffusion of the analyte, and the flow rate of the bulk solution. In order to exclude that the measurements of the association and dissociation constants of the analyte to the *ligand* were artifactually affected by mass transfer, the flow of the solution containing IgG1 7E6 (0.13 µM) over zGCAP3 was injected at three different rates (20 µl/min, 30 µl/min, 40 µl/min). The similarity of the binding constants obtained from the three sensorgrams excluded a significant effect of mass transfer.

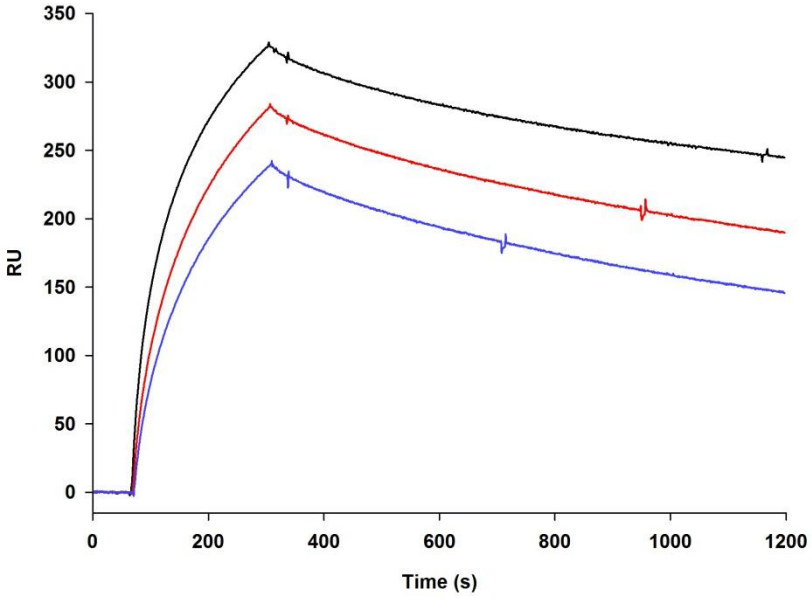

Fig. 3.20. SPR sensorgrams of IgG1 7E6 (0.13 µM) binding to zGCAP3 (1500 RU immobilized) at different flow rates of injection: 20 µl/min (*black line*), 30 µl/min (*red line*), 40 µl/min (*blue line*). The association and dissociation phases were followed for 4 and 15 minutes respectively.

3.2.9 Evaluation of zGCAP3 and its antibody on GC activity

The ultimate goal of the experiment described in the following is to record the response waveform of an isolated zebrafish cone to structured light stimuli, and assess the possible modifications of this waveform following the incorporation in the cytosol, with the intracellular perfusion system, of purified proteins, antibodies, and drugs targeted to the phototransduction cascade. To achieve this goal, it is necessary first to assess that the photoresponse waveform remain stable for several minutes, i.e. the time required to complete a perfusion experiment protocol. This protocol consists of recording of some control photoresponses, measuring the effect on the same photoresponses of a test solution, and finally following the photoresponse waveform recover (or not) the control ones. The stability of the recordings from zebrafish cones is well illustrated in Fig. 3.21, where a typical cone is recorded for more than 22 minutes, showing stable light sensitive current amplitude and flash (and step) response kinetics and sensitivity.

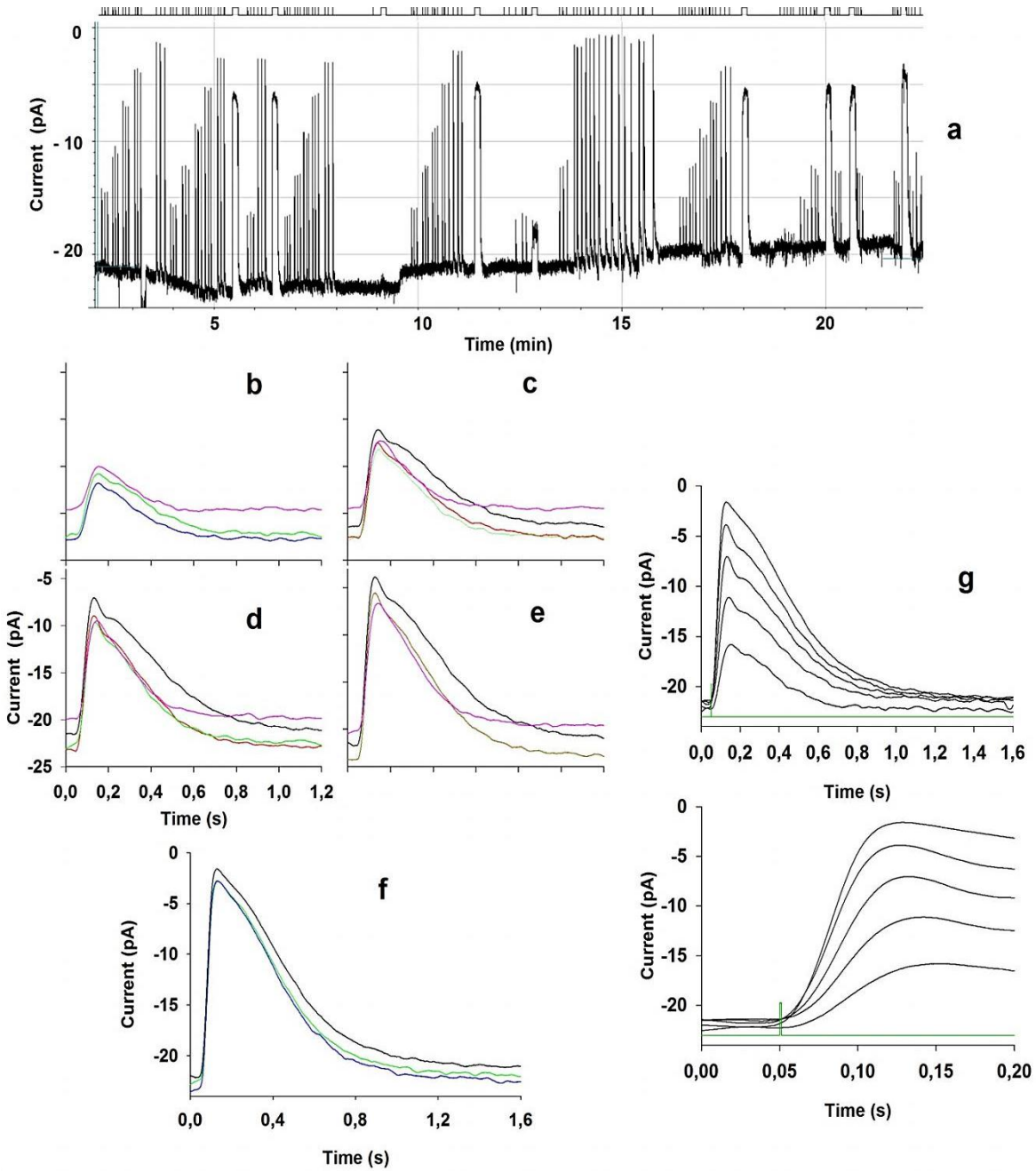

Fig. 3.21. Stability of the whole-cell recordings from zebrafish cones. ***a***, low trace, recording of the light sensitive current in response to light flashes and steps on a slow time scale; upper trace, timing of delivery of light flashes and steps. ***b***, the average and smoothed response of three consecutive flashes of same intensity delivered within ~5 min from the beginning of recording (*green trace*). This group of three flashes is repeated after ~15 min of recording (*blue*) and after ~20 min of recoding (*magenta*), i.e. after having delivered 90 light flashes of various intensities and 5 light steps. ***c***, ***d***, ***e***, and ***f***, light stimulation protocol as in ***b***, but the flash intensity is doubled from one panel to the other one. The color code in ***c*** **-** ***f*** is as in ***a***; two additional colors are used to indicate the average of three photoresponses recorded after ~2 min of recording (*black*), and after ~10 min of recording (*red*). ***g***, the responses reported in each of the 5 panels ***c*** **-** ***f*** are averaged together and the corresponding 5 traces are reported on a two different time scales. Green trace is the flash timing.

The small changes in the baseline (Fig. 3.21) are due to changes of the light-insensitive current flowing through the inner segment conductances, that gave an average current of -3 pA. Indeed, the current suppressed by the bright flashes was always ~18 pA within the 22 min recording (during which were delivered more than 100 light flashes and 8 light steps).

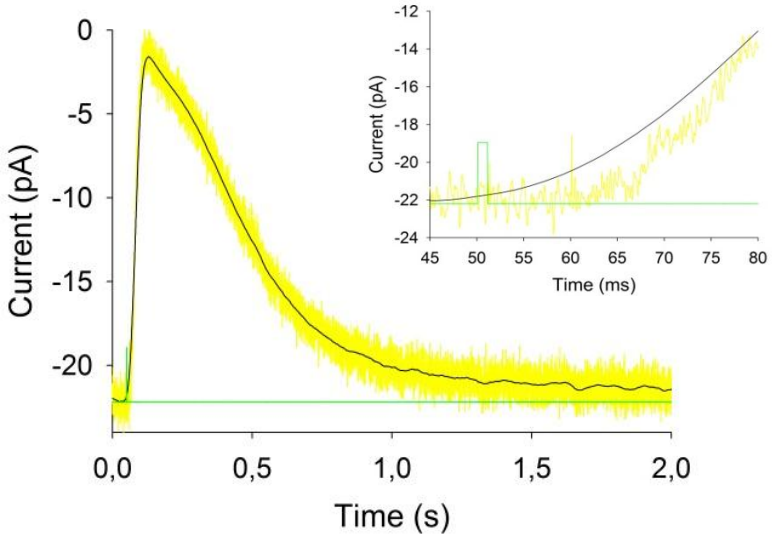

Fig. 3.22. Comparison between a single unsmoothed photoresponse to a saturating flash of a train of three ones, compared with the response resulting from the smoothing of the average of all three responses. Inset, enlargement of 35 ms of the large panel, to show the delay between the flash and the response rising phase. *Green trace* is the flash timing.

Since the photoresponses are very small and the background noise high, to reject the noise each photoresponse shown in Fig. 3.21 is the average of three responses to the same flash, and the resulting average response is further smoothed by using the local smoothing routine of Sigmaplot (Fig. 3.22). This routine uses polynomial regression and weights computed from the Gaussian density function; the smoother function chosen is the negative exponential, with a sampling proportion of 0.02, a polynomial degree 1, and a number of interval that is 1/10 of the total number of samples of each trace. The parameters of the smoothing routine were chosen to reject as much as possible the noise, without distorting the photoresponse waveform. This was tested by comparing the average response to three saturating flashes (that are the fastest responses, i.e. the most prone to be distorted by the smoothing routine; Fig. 3.22, *yellow trace*) with the same photoresponses after smoothing (Fig. 3.22, *black trace*). The smoothing did not change significantly the waveform of the photoresponse, that are therefore ready to be fitted by phototransduction models; however, the delay between the flash delivery time (Fig. 3.22 *insert, green trace*) and the time in which the current start to depart from the dark current level, was somewhat altered (Fig. 3.22, *insert*:

compare *yellow trace* with the *black trace*), but this delay can however be readily measured on the unsmoothed (but averaged) trace on a fast time scale (and it resulted of 13 ± 2 ms, n=20).

Besides the stability of the light response, it is necessary to check that the light adaptation process in isolated cones was not altered by the recording technique. This was evaluated in the experiment of Fig. 3.23, where it is shown the response to steps of light, and the photoresponses to flashes delivered in the dark and on a step.

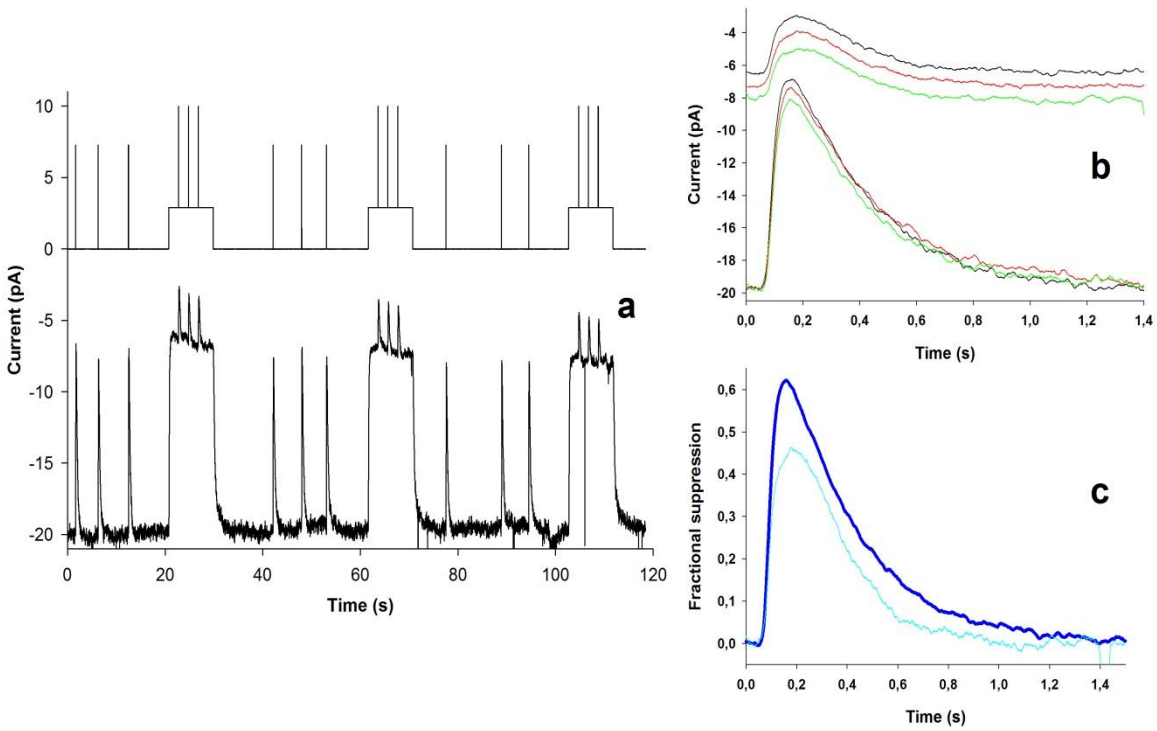

Fig. 3.23. Light adaptation. ***a***, low trace, recording of the light sensitive current in response to light flashes and steps on a slow time scale; upper trace, timing of delivery of light flashes and steps. ***b***, comparison of three average responses to light flashes in the dark (each one is in turn the average of three responses) and the three average responses to light flashes (twice as intense as the ones delivered in the dark) delivered during three steps of light. The *black*, *green*, and *red* traces correspond to a couple of average responses (one in the dark and the other one on the step) to the first, second and third set of three flash responses in the dark and three flash responses on the step, as indicated in upper trace of ***a***. ***c***, comparison between the average of the 9 flash responses in the dark (suppressing about 65% of the dark current, that is ~19.7 pA), and the average of the 9 flash responses during the three light steps (suppressing about 45% of the residual light sensitive current of each step, that is ~7.3 pA; the three steps suppressed ~63% of dark current).

was twice as much the one delivered in the dark. Again, the recordings were quite stable, despite the large amount of light delivered: the waveform of the average response to three flashes delivered in the dark and during the step of light at the beginning of recording (*black traces*; Fig 3.23, panel *b*), in the middle (*green*), and at the end (*red*) were indeed almost identical. The typical features of the light adaptation were also preserved: the response to a step of light showed the normal waveform, i.e. a peak amplitude was rapidly reached just after the

light onset, followed by a slow decay to a steady state level (Fig. 3.23, panel *a*). Moreover, the average of the 9 photoresponses to flashes delivered on the step of light were smaller and faster in respect to the average of the 9 photoresponses in the dark when plotted as the fractional suppression of the light sensitive current (although they were evoked by flashes of same intensity of the flashes delivered in the dark, but lasting 20 ms instead of 10 ms, i.e. they delivered twice the number of photons in respect to the flashes delivered in the dark). It can be therefore concluded that the pipette with the enlarged shank did not significantly wash out any molecule necessary for phototransduction.

At this point, the zGCAP3 and the anti-zGCAP3 proteins (i.e. purified monoclonal antibody 7E6) were delivered in the cytosol by using the intracellular perfusion system. Perfusion with zGCAP3 did not altered significantly the light response (n=4): just in one single case it was observed a slight acceleration and the amplitude reduction of the light response (data not shown), as it would be expected if the target of GCAP3 was the GC. The unexpected lack of an effect of zGCAP3 incorporation in the cone cytosol, suggests that the endogenous number of zGCAP3 is saturating, i.e. their number is equal or above the number of their target molecules (GC), therefore any further increase of zGAP3 in the cytosol is uneffective.

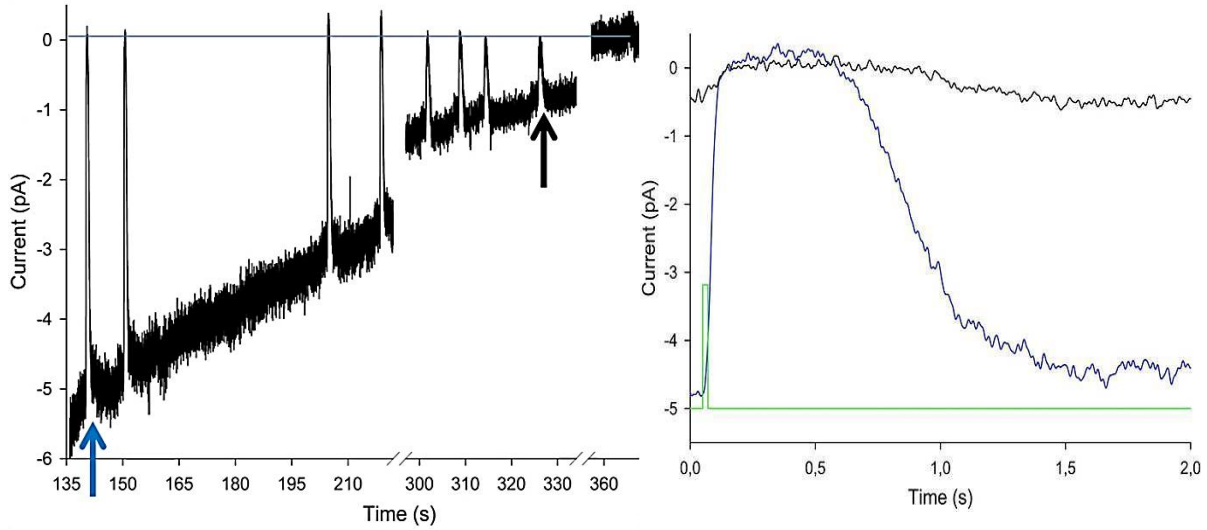

Fig. 3.24. Effect of injection of anti-zGCAP3 in the zebrafish cone cytosol. Left, recording of the light sensitive current on a slow time scale. Right, comparison of the flashes indicated by the arrows on expanded scales; largest response (*blue trace*) is indicated by the *blue arrow*, smaller response (*black trace*) is indicated by the *black arrow*; light stimulus timing is in green.

The anti-zGCAP3 incorporation in the cytosol caused instead the progressive current fall, followed by the progressive fall of saturating flash response amplitude, with no changes in the 0 level of light sensitive current (indicated by the *blue line* in Fig.3.24, *left*; n=4). This shows that the current decay was produced by the progressive GC inhibition: since the dark

current level is due to the balance of a continuous synthesis by GC and a continuous hydrolysis by PDE, as soon as the GC basal activity is reduced (even by a little amount), the PDE hydrolysis (unaffected by the anti-zGCAP3) is expected to cause the cGMP level (i.e. the light sensitive current) to drop to 0, as it was indeed observed. Moreover, the anti-zGCAP3 causes a reduction of Ca^{2+} sensitivity of GC, resulting in the observed slowdown of response recovery (Fig. 3.24, *right*), that was already observed for the response in blue (compare its waveform with the one evoked by the same flash of panel *f* of Fig. 3.21, and of panels *c* of Fig. 3.22 and 3.23). Indeed, the concentration of anti-GCAP used (6 µM) is so large in respect to the GC affinity for the antibody, that even a little leakage of antibody out of the perfusion tube is enough to produce a significant effect on the current level and the response waveform.

4. REFERENCES

Aili D and Stevens MM (2010). Bioresponsive peptide-inorganic hybrid nanomaterials. *Chemical Society reviews* 39: 3358-70.

Ames JB and Ikura M (2002). Structure and membrane-targeting mechanism of retinal Ca2+-binding proteins, recoverin and GCAP-2. *Advances in experimental medicine and biology* 514: 333-48.

Andreu D, Ubach J, Boman A, Wahlin B, Wade D, Merrifield RB and Boman HG (1992). Shortened cecropin A-melittin hybrids. Significant size reduction retains potent antibiotic activity. *FEBS Lett* 296: 190-4.

Baumann G and Mueller P (1974). A molecular model of membrane excitability. *J Supramol Struct* 2: 538-57.

Behnen P, Scholten A, Ratscho N and Koch KW (2009). The cone-specific calcium sensor guanylate cyclase activating protein 4 from the zebrafish retina. *Journal of biological inorganic chemistry : JBIC : a publication of the Society of Biological Inorganic Chemistry* 14: 89-99.

Benedusi M, Aquila M, Milani A and Rispoli G (2011). A pressure-polishing set-up to fabricate patch pipettes that seal on virtually any membrane, yielding low access resistance and efficient intracellular perfusion. *Eur Biophys J* 40: 1215-23.

Bilotta J and Saszik S (2001). The zebrafish as a model visual system. *International journal of developmental neuroscience : the official journal of the International Society for Developmental Neuroscience* 19: 621-9.

Bockmann RA, Hac A, Heimburg T and Grubmuller H (2003). Effect of sodium chloride on a lipid bilayer. *Biophys J* 85: 1647-55.

Boheim G (1974). Statistical analysis of alamethicin channels in black lipid membranes. *J Membr Biol* 19: 277-303.

Brogden KA (2005). Antimicrobial peptides: pore formers or metabolic inhibitors in bacteria? *Nat Rev Microbiol* 3: 238-50.

Canziani GA, Klakamp S and Myszka DG (2004). Kinetic screening of antibodies from crude hybridoma samples using Biacore. *Analytical biochemistry* 325: 301-7.

Carratu L, Franceschelli S, Pardini CL, Kobayashi GS, Horvath I, Vigh L and Maresca B (1996). Membrane lipid perturbation modifies the set point of the temperature of heat shock response in yeast. *Proc Natl Acad Sci U S A* 93: 3870-5.

Chen HM, Clayton AH, Wang W and Sawyer WH (2001). Kinetics of membrane lysis by custom lytic peptides and peptide orientations in membrane. *Eur J Biochem* 268: 1659-69.

Coronado R (1985). Effect of divalent cations on the assembly of neutral and charged phospholipid bilayers in patch-recording pipettes. *Biophys J* 47: 851-7.

Crisma M, Peggion C, Baldini C, Maclean EJ, Vedovato N, Rispoli G and Toniolo C (2007). Crystal structure of a spin-labeled, channel-forming alamethicin analogue. *Angew Chem Int Ed Engl* 46: 2047-50.

Dathe M, Nikolenko H, Meyer J, Beyermann M and Bienert M (2001). Optimization of the antimicrobial activity of magainin peptides by modification of charge. *FEBS Lett* 501: 146-50.

Dell'Orco D, Schmidt H, Mariani S and Fanelli F (2009). Network-level analysis of light adaptation in rod cells under normal and altered conditions. *Molecular bioSystems* 5: 1232-46.

Dizhoor AM, Olshevskaya EV, Henzel WJ, Wong SC, Stults JT, Ankoudinova I and Hurley JB (1995). Cloning, sequencing, and expression of a 24-kDa Ca(2+)-binding protein activating photoreceptor guanylyl cyclase. *J Biol Chem* 270: 25200-6.

Fain GL, Matthews HR, Cornwall MC and Koutalos Y (2001). Adaptation in vertebrate photoreceptors. *Physiological reviews* 81: 117-151.

Fox RO, Jr. and Richards FM (1982). A voltage-gated ion channel model inferred from the crystal structure of alamethicin at 1.5-A resolution. *Nature* 300: 325-30.

Fries R, Scholten A, Saftel W and Koch KW (2011). Operation profile of zebrafish guanylate cyclase-activating protein 3. *Journal of neurochemistry*.

Gadsby DC (2009). Ion channels versus ion pumps: the principal difference, in principle. *Nature reviews. Molecular cell biology* 10: 344-52.

Ganz T (2003). Defensins: antimicrobial peptides of innate immunity. *Nat Rev Immunol* 3: 710-20.

Gorczyca WA, Polans AS, Surgucheva IG, Subbaraya I, Baehr W and Palczewski K (1995). Guanylyl cyclase activating protein. A calcium-sensitive regulator of phototransduction. *J Biol Chem* 270: 22029-36.

Gordon YJ, Romanowski EG and McDermott AM (2005). A review of antimicrobial peptides and their therapeutic potential as anti-infective drugs. *Curr Eye Res* 30: 505-15.

Haeseleer F, Sokal I, Li N, Pettenati M, Rao N, Bronson D, Wechter R, Baehr W and Palczewski K (1999). Molecular characterization of a third member of the guanylyl cyclase-activating protein subfamily. *J Biol Chem* 274: 6526-35.

Hall K and Aguilar MI (2010). Surface plasmon resonance spectroscopy for studying the membrane binding of antimicrobial peptides. *Methods Mol Biol* 627: 213-23.

Hamill OP, Marty A, Neher E, Sakmann B and Sigworth FJ (1981). Improved patch-clamp techniques for high-resolution current recording from cells and cell-free membrane patches. *Pflugers Archiv : European journal of physiology* 391: 85-100.

Hille B (1992). *Ionic channels of excitable membranes,* Sinauer Associates: Sunderland, Mass.

Hoskin DW and Ramamoorthy A (2008). Studies on anticancer activities of antimicrobial peptides. *Biochim Biophys Acta* 1778: 357-75.

Imanishi Y, Yang L, Sokal I, Filipek S, Palczewski K and Baehr W (2004). Diversity of guanylate cyclase-activating proteins (GCAPs) in teleost fish: characterization of three novel GCAPs (GCAP4, GCAP5, GCAP7) from zebrafish (Danio rerio) and prediction of eight GCAPs (GCAP1-8) in pufferfish (Fugu rubripes). *Journal of molecular evolution* 59: 204-17.

Kalfa VC, Jia HP, Kunkle RA, McCray PB, Jr., Tack BF and Brogden KA (2001). Congeners of SMAP29 kill ovine pathogens and induce ultrastructural damage in bacterial cells. *Antimicrob Agents Chemother* 45: 3256-61.

Koch KW and Stryer L (1988). Highly cooperative feedback control of retinal rod guanylate cyclase by calcium ions. *Nature* 334: 64-6.

Lamb TD and Pugh EN, Jr. (2006). Phototransduction, dark adaptation, and rhodopsin regeneration the proctor lecture. *Investigative ophthalmology & visual science* 47: 5137-52.

MacDonald RC, MacDonald RI, Menco BP, Takeshita K, Subbarao NK and Hu LR (1991). Small-volume extrusion apparatus for preparation of large, unilamellar vesicles. *Biochim Biophys Acta* 1061: 297-303.

Malmqvist M (1993). Biospecific interaction analysis using biosensor technology. *Nature* 361: 186-7.

Mendez A and Chen J (2002). Mouse models to study GCAP functions in intact photoreceptors. *Advances in experimental medicine and biology* 514: 361-88.

Molle G, Dugast JY, Spach G and Duclohier H (1996). Ion channel stabilization of synthetic alamethicin analogs by rings of inter-helix H-bonds. *Biophys J* 70: 1669-75.

Nakatani K, Chen C, Yau KW and Koutalos Y (2002). Calcium and phototransduction. *Advances in experimental medicine and biology* 514: 1-20.

Noshiro D, Asami K and Futaki S (2010). Metal-assisted channel stabilization: disposition of a single histidine on the N-terminus of alamethicin yields channels with extraordinarily long lifetimes. *Biophys J* 98: 1801-8.

Olshevskaya EV, Ermilov AN and Dizhoor AM (1999). Dimerization of guanylyl cyclase-activating protein and a mechanism of photoreceptor guanylyl cyclase activation. *J Biol Chem* 274: 25583-7.

Palczewski K, Jager S, Buczylko J, Crouch RK, Bredberg DL, Hofmann KP, Asson-Batres MA and Saari JC (1994). Rod outer segment retinol dehydrogenase: substrate specificity and role in phototransduction. *Biochemistry* 33: 13741-50.

Palczewski K, Polans AS, Baehr W and Ames JB (2000). Ca(2+)-binding proteins in the retina: structure, function, and the etiology of human visual diseases. *BioEssays : news and reviews in molecular, cellular and developmental biology* 22: 337-50.

Palczewski K, Sokal I and Baehr W (2004). Guanylate cyclase-activating proteins: structure, function, and diversity. *Biochemical and biophysical research communications* 322: 1123-30.

Papo N and Shai Y (2005). Host defense peptides as new weapons in cancer treatment. *Cellular and molecular life sciences : CMLS* 62: 784-90.

Peggion C, Coin I and Toniolo C (2004). Total synthesis in solution of alamethicin F50/5 by an easily tunable segment condensation approach. *Biopolymers* 76: 485-93.

Polans A, Baehr W and Palczewski K (1996). Turned on by Ca2+! The physiology and pathology of Ca(2+)-binding proteins in the retina. *Trends in neurosciences* 19: 547-54.

Priel A, Gil Z, Moy VT, Magleby KL and Silberberg SD (2007). Ionic requirements for membrane-glass adhesion and giga seal formation in patch-clamp recording. *Biophys J* 92: 3893-900.

Rispoli G (1998). Calcium regulation of phototransduction in vertebrate rod outer segments. *Journal of photochemistry and photobiology. B, Biology* 44: 1-20.

Rispoli G, Sather WA and Detwiler PB (1993). Visual transduction in dialysed detached rod outer segments from lizard retina. *The Journal of physiology* 465: 513-37.

Safsten P, Klakamp SL, Drake AW, Karlsson R and Myszka DG (2006). Screening antibody-antigen interactions in parallel using Biacore A100. *Analytical biochemistry* 353: 181-90.

Saint N, Cadiou H, Bessin Y and Molle G (2002). Antibacterial peptide pleurocidin forms ion channels in planar lipid bilayers. *Biochim Biophys Acta* 1564: 359-64.

Scholten A and Koch KW (2011). Differential calcium signaling by cone specific guanylate cyclase-activating proteins from the zebrafish retina. *PloS one* 6: e23117.

Vedovato N, Baldini C, Toniolo C and Rispoli G (2007). Pore-forming properties of alamethicin F50/5 inserted in a biological membrane. *Chemistry & biodiversity* 4: 1338-46.

Wallace DP, Tomich JM, Eppler JW, Iwamoto T, Grantham JJ and Sullivan LP (2000). A synthetic channel-forming peptide induces Cl(-) secretion: modulation by Ca(2+)-dependent K(+) channels. *Biochim Biophys Acta* 1464: 69-82.

Wilde AA (2008). Channelopathies in children and adults. *Pacing and clinical electrophysiology : PACE* 31 Suppl 1: S41-5.

Yeaman MR and Yount NY (2003). Mechanisms of antimicrobial peptide action and resistance. *Pharmacol Rev* 55: 27-55.

Yenugu S, Hamil KG, French FS and Hall SH (2004). Antimicrobial actions of the human epididymis 2 (HE2) protein isoforms, HE2alpha, HE2beta1 and HE2beta2. *Reprod Biol Endocrinol* 2: 61.

Zhou Y, Shi J, Cui J and Deng CX (2008). Effects of extracellular calcium on cell membrane resealing in sonoporation. *Journal of controlled release : official journal of the Controlled Release Society* 126: 34-43.